Synchronization and Sensing with Steady State Superradiance and Spin Squeezing

by

Joshua M. Weiner

B.S., California Institute of Technology, 2009

M.S., University of Colorado Boulder, 2012

A thesis submitted to the
Faculty of the Graduate School of the
University of Colorado in partial fulfillment
of the requirements for the degree of
Doctor of Philosophy
Department of Physics
2015

This thesis entitled:
Synchronization and Sensing with Steady State Superradiance and Spin Squeezing
written by Joshua M. Weiner
has been approved for the Department of Physics

James K. Thompson

Murray J. Holland

Date ____________

The final copy of this thesis has been examined by the signatories, and we find that both the content and the form meet acceptable presentation standards of scholarly work in the above mentioned discipline.

Weiner, Joshua M. (Ph.D., Physics)

Synchronization and Sensing with Steady State Superradiance and Spin Squeezing

Thesis directed by Prof. James K. Thompson

Utilizing controllable collective light-atom interactions, I explore the properties of large ensembles of cold ^{87}Rb atoms interacting with an optical cavity. The interactions are used to produce collective light emission and to generate entangled atomic states.

In one set of experiments, I demonstrate a unique atomic magnetometer based on superradiant Raman lasing transitions between hyperfine ground states. This sensor can operate in a continuous broadband mode or a discrete narrowband mode based on the evolution of the atomic coherence in the dark. I also discuss the fundamental sensitivity of this type of detector.

In a second set of experiments, I present studies of the synchronization mechanism between two ensembles undergoing steady state superradiance within the same optical cavity. I explore the behavior of the two oscillators in response to the introduction of controllable phase errors between them in both transient and steady state experiments. This work may stimulate future studies of quantum phase transitions in open quantum systems.

Finally, I discuss progress in another related experimental direction: cavity-aided non-demolition measurements of the collective atomic spin state of an ensemble of atoms. The coherence-preserving collective measurements presented may one day have the capacity to reduce the impact of quantum noise in state-of-the-art precision measurements like clocks and acceleration sensors based on atoms. By upgrading our apparatus, we expect to significantly improve on our previous factor of 10 improvement over the standard quantum limit on quantum phase estimation for unentangled atoms.

Dedication

For Mom and Dad

Acknowledgements

I'm grateful to have collaborated with and been supported by a large number of excellent people during my time in graduate school.

First, I would like to thank my family, especially my parents. They have encouraged me every step along the way.

I'd also like to thank my advisor, James. His talent for coming up with simple and elegant intuitive pictures for the most difficult concepts aided tremendously in communicating and understanding the science. He cares deeply about his students and his enthusiasm and passion for experimental science is contagious and made the lab a great place to work.

Early in my career, Zilong and Justin were patient mentors. Kevin Cox was with me nearly every day in lab for the past four years. His constant enthusiasm and willingness to engage with far-out ideas kept the workplace lively. I am certain that Matt Norcia and Graham Greve will go on to make many more exciting discoveries. Thanks also go to the other graduate students and undergraduates that have spent time in the Thompson Lab: Matthew Winchester, Karl Mayer, Eliza Picozzi, and Katie McAlpine.

Terry Brown and the JILA Electronics Shop deserve credit for so many technical contributions like our fancy loop filters. Hans Green and Todd Asnicar were crucial for moving the optics tables from the B Wing to the X Wing. They and the rest of the JILA staff make the grad students' jobs so much easier!

Lastly, I'm thankful for Dylan. I couldn't have done it without her love, support, and encouragement.

Contents

Chapter

Appendix

Tables

Table

Figures

Figure

Chapter 1

Introduction

1.1 A Quantum Playground

The trend of quantum physics in the past century has been ever-better control of quantum systems. In atomic and molecular systems, techniques of spectroscopy and laser cooling have enabled experimental realizations of the Gedanken experiments conceived by the pioneers of quantum theory [57]. Applications of quantum systems are numerous and varied, including quantum computing [66], precision measurements of fundamental constants [9, 102, 103], a standard definition of the second [59], and atomic clocks in the GPS network [81].

The experimental system consisting of atoms inside an optical cavity used during the course of my doctoral work represents a kind of quantum playground in which many phenomena can be studied. Atoms have been used in conjunction with optical cavities to create clocks enhanced by entanglement [79], generate single on-demand photon pairs [13], and create a single-atom laser [90]. But the quantum frontier is still expanding with fundamentally quantum effects like entanglement finally entering into a useful regime for improving precision measurements [16] and using correlated atoms to improve spectroscopy [87] or optical frequency references [94, 30, 65].

In this dissertation, I describe experiments that explore part of this quantum frontier. In order to do this, I examine the properties of an atomic ensemble of ^{87}Rb atoms interacting with an optical cavity for producing collective light emission and for generating entangled atomic states. Light in the cavity facilitates interactions between the atoms, allowing the formation of collective optical dipoles in the process of steady state superradiance. First, I demonstrate a proof-of-principle sensor of magnetic fields based on superradiant light emission. Next, I characterize the interactions between two distinct ensembles of atoms undergoing steady state superradiance. The interactions can cause synchronization between the phase of the light emitted from each ensemble even when the natural frequencies of the ensembles differ.

I conclude by discussing a next generation of spin squeezing experiments based on coherence-preserving measurements of collective atomic spin states. Through improvements to the apparatus, I show an increased capacity for measurement-induced entanglement to improve atomic phase measurements. The common thread in these experiments is the use of light to generate controllable interactions between atoms and to create useful collective states.

Before describing the experiments in more detail, I begin by discussing the two key features of our playground: atoms and an optical cavity.

1.1.1 Atoms for Precision Measurements

Atomic systems are an attractive platform for creating sensors because of atoms' identical nature, small size, well-characterized spectral properties, and well-understood response to perturbations. Laser cooling and trapping techniques afford control over the external states of atoms and optical pumping techniques can create low-entropy distributions of internal states of atoms. The controlling light fields can propagate long distances in free space, so atoms can be trapped and controlled far from laboratory elements that may introduce perturbing fields. Coherence times of the resulting atomic states can be on the order of seconds even in a room-temperature environment. This is unlike quantum systems in solid state including superconducting qubits [143, 139], or opto-mechanical oscillators [5], which can differ in essential properties depending on the details of their local environments or the precise parameters of their fabrication. Solid state spin systems such as nitrogen-vacancy centers in diamond [124] are subject to highly variable local environmental conditions.

The identical nature of atoms is exploited to create extremely precise sensors. Using many atoms allows a measurement to be effectively massively parallel in nature. The combination of stable atomic states and a quiet, well-characterized laboratory environment results in the most accurate clocks in existence [99, 61, 107] and a standard definition of the second [59, 138]. Clocks based on atomic ions are capable of sensing the Earth's gravitational redshift on the meter scale, corresponding to a fractional change in frequency $\Delta\nu/\nu = 4 \times 10^{-17}$ [36]. Conversely, atomic states that are sensitive to external fields can be used as highly sensitive sensors of those same fields. For instance, atomic magnetometers are capable of sensing magnetic fields a factor of 10^8 smaller than the Earth's magnetic field [69, 113, 131].

1.1.2 Generating Correlations between Atoms

Properly controlled interactions can be used to generate useful correlations between atoms. Collisional interactions [56, 26, 97, 84], coulombic forces [118, 52], and light-mediated interactions [3, 112, 110, 32] can be used to induce quantum correlations between atoms to reduce readout noise or produce highly entangled quantum states with a large number of atoms. However, collisional interactions between atoms can introduce systematic errors in precision measurements [145], a challenge that remains to be solved in these systems. Light-mediated interactions are experimentally desirable for a few reasons. They have the capacity to be turned off, e.g., by extinguishing laser light applied to the atoms. Also, light-mediated interactions can be effectively infinite range (and thus "all-to-all") as long as the atoms are well-localized with respect to the applied coherent field, which is experimentally feasible in both optical cavities and free space [8].

1.1.3 Atom-Optical Cavity Systems

Optical cavities are versatile platforms for creating light-mediated atomic interactions. Essentially infinite-range, all-to-all atomic coupling can be created straightforwardly with a well-defined bus (a single transverse and longitudinal cavity mode). The lifetime of light in the cavity mode can also be made to be shorter than the effective lifetime of the atomic state. This can be expressed in terms of the cavity power decay rate κ being much greater than the atomic decay lifetime γ [94, 93, 30, 65]. Also, the coupling strength can be large even when the atoms are separated by many wavelengths of light. This allows one to avoid density dependent effects like collisional shifts.

A high collective optical depth is important for creating indistinguishability between the atoms and strengthening the interaction between the atoms and the cavity mode. A convenient parametrization of the atom-cavity coupling strength is the unitless single-particle cooperativity, $C = \frac{4g^2}{\kappa\gamma} \approx 10^{-2}$ in our system. For a single atom in an optical excited state, C represents the fraction of all decay events in which the atom emits a photon into the cavity mode compared to all modes of decay. The simple geometric interpretation of C is the fractional solid angle subtended by the cavity mode in the far-field, multiplied by the cavity finesse [123]. Here, $2g$ is the frequency at which a single atom would cyclically absorb and re-emit light into the cavity mode. The spontaneous emission process, loss of photons from the cavity, and coherent coupling of atoms and cavity photons is illustrated in Figure 1.1.

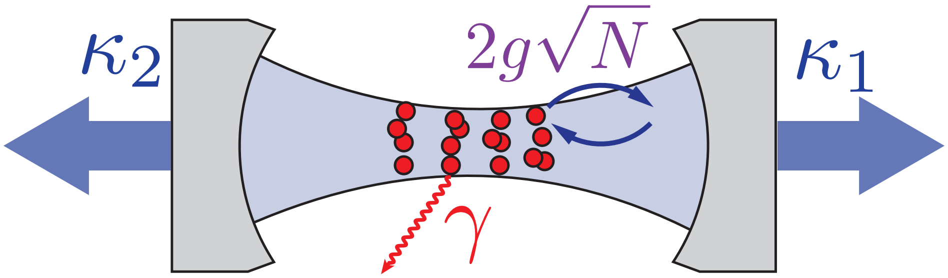

Figure 1.1: Representation of coupled atom-cavity system showing the various decay processes. Coupling to the outside environment is provided by free space scattering at single-particle rate γ and power decay rates from the cavity $\kappa_1 + \kappa_2 = \kappa$. Collective coupling at rate $2g\sqrt{N}$ creates coherent oscillations of the excitations between the atoms and the cavity.

When N atoms are placed inside an optical cavity, the rate of emission into the cavity mode is enhanced by a factor of NC above the spontaneous emission rate γ, resulting in an enhanced single-particle rate $NC\gamma$. The parameter NC represents the cavity-enhanced collective optical depth [123]. Correspondingly, there is a collectively enhanced rate of absorption and re-emission into the cavity at rate $\Omega = 2g\sqrt{N}$, termed the vacuum Rabi splitting. Optical cavities can create a high collective optical depth $NC \gg 1$ with the use of many atoms even when the single-particle cooperativity C is low. Our system is well into the high collective coupling regime with $NC \sim 10^3$. In general, engineering systems with even $C \simeq 1$ may be difficult, yet increasing the number of participating atoms can increase the optical depth enough for collective physics to arise. A classical analogue for this increased emission rate is a set of phased array dipole antennas, which have time phase of radiation of each emitter set to constructively interfere with the phase of radiation of neighboring dipoles. The result is an intensity of light $\propto N^2$ rather than N as occurs in the case of incoherently added electric fields.

1.2 Steady State Superradiance for Magnetometry and Synchronization

Superradiance is a fundamentally interesting process that has promise for improving metrology. Steady state superradiance based on long-lived atomic states in an optical cavity is expected to have spectral properties that exceed state-of-the-art lasers [94, 30, 93]. We demonstrate that the light emitted by an ensemble of atoms can be used to sense phase shifts of the atomic coherence caused by an externally applied magnetic field. External magnetic fields affect the phase of the atomic dipole and therefore the phase of the output light. A unique feature of this magnetometer is that controllable interactions allow operation in a broadband "active" mode or a narrowband "passive" mode, each with complementary trade-offs between bandwidth and sensitivity. I also discuss the fundamental limitations to the sensitivity of the magnetometer.

A second set of experiments explores the behavior of two superradiant ensembles when the perturbing fields are the intracavity electric fields emitted from the other ensemble. We introduce differences in frequencies or phases of the light emitted from each ensemble by applying a combination of magnetic fields and laser light. I discuss the behavior of the two ensembles as they interact in various regimes of their relative frequency detuning and in response to relative phase errors.

1.2.1 Bad Cavity Lasers

Steady state superradiance operates in the "bad cavity" regime of laser physics, where the atomic transverse broadening $\gamma_\perp$ is much smaller than the cavity power decay rate κ. Here, $\gamma_\perp = \gamma/2 + 1/T_2$ is the decay rate of atomic coherence due to spontaneous decay at rate γ and other dephasing mechanisms at rate $1/T_2$. In contrast, the "good cavity" regime where most lasers operate has a narrow optical cavity and a broad atomic gain medium. There is also a crossover regime where far-infrared gas lasers can operate with $\gamma_\perp/\kappa \approx 0.1$ to 10 [71, 72]. In the work discussed here, $\gamma_\perp/\kappa$ ranges from 10^{-4} to 10^{-2}. This is akin to the regime in which microwave masers operate, but with optical frequencies (10^{14} Hz) instead of microwaves (10^9 Hz) [68, 132].

Since the atomic coherence is longer-lived than the photonic coherence, the atoms are the primary reservoir for phase information. This means that the phase of the collective atomic dipole sets the phase of the emitted light. A simple schematic of how a candidate atomic system might be used in conjunction with an optical cavity to create steady state superradiance is shown in Figure 1.2(a). Non-resonant, non-collective repumping light with single-particle repumping rate W is applied to maintain inversion while collective emission into the cavity sustains a collective radiating dipole with enhanced emission rate.

During the process of superradiance, the cavity photons act as a communication bus through which the atoms correlate their optical dipole phases. The optical dipole phases are correlated in such a way that there is constructive interference between the light emitted by individual atoms. This can happen even when the average intracavity photon number $M_c < 1$ [24], emphasizing the role of the atoms in storing the phase coherence.

In the work presented in this thesis, we use a model Raman system to access the bad cavity regime. In our ^{87}Rb system, the decay rates Γ of the excited optical states are comparable to the cavity linewidth κ while the hyperfine ground states are metastable. However, we can create an effective two-photon Raman decay with a much smaller effective decay rate $\gamma \ll \Gamma$ (on the order of 10^0 to 10^3) by applying a dressing laser, as depicted in Figure 1.2(b). This gives experimental control of the decay rate, which can even be changed abruptly or essentially extinguished. The presence of more energy levels also leads to dynamics not present in the model system based on atoms with highly forbidden transitions, as discussed in Chapter 2. In Chapters 2, 4, and 5, I describe how this control can be used to create a magnetometer with variable bandwidth and how it can introduce relative phase errors between superradiant lasers so that the resulting dynamics can be observed.

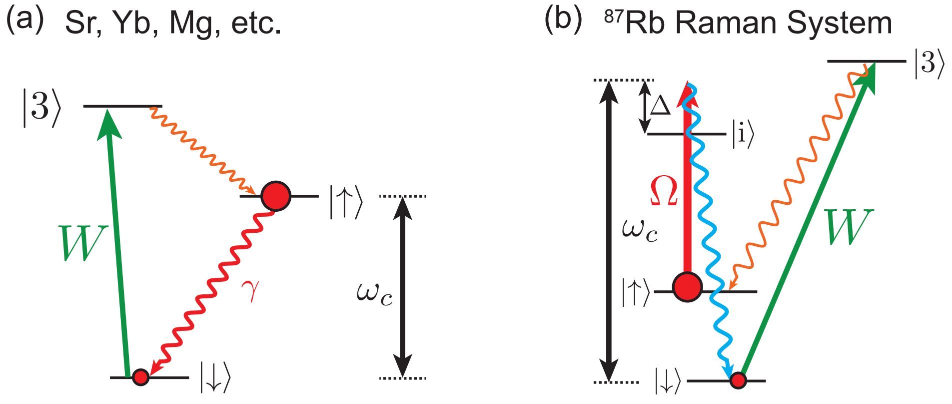

Figure 1.2: Energy level diagrams for (a) an ideal superradiant system based on alkaline-earth-like atoms and (b) for our Raman system in rubidium. Collective emission into the cavity between $|\uparrow\rangle$ and $|\downarrow\rangle$ is sustained by repumping through an intermediate state $|3\rangle$ at rate W. (b) The addition of an intermediate state $|i\rangle$ and application of a dressing laser with strength parametrized by Rabi frequency Ω causes decay from $|\uparrow\rangle$ to $|\downarrow\rangle$.

1.2.2 Synchronization

While steady state superradiance is a quantum mechanical phenomenon, it has deep connections to the field of nonlinear dynamics and synchronization physics. For superradiance to occur, the atoms must synchronize their optical dipole phases with one another. Synchronization of classical oscillators is observed in a wide variety of systems, including biological, chemical, and social systems [120]. Synchronization dynamics are critical for understanding and controlling technologically relevant systems like frequency combs [47, 134], opto-mechanical oscillators [144, 6], and electro-mechanical systems [88]. The "bottom-up" emergent phenomenon of synchronization can generate highly ordered collective states of classical oscillators even with an inhomogeneous distribution of frequencies [121], and similar useful collective states of systems that intrinsically have quantum noise should be possible [141, 73, 75]. Synchronized open quantum systems will be important for understanding synchronization models in open quantum systems [141, 48], creating associative memories [53], and using the dissipation mechanism to engineer states useful for quantum computing [129].

The phase synchronization process studied here could inform future applications of superradiant lasers for exploring fundamental physics or improving technology. Two superradiant lasers operating within the same cavity are a candidate system for exploring synchronization models in open quantum systems [141]. Also, a better understanding the superradiant synchronization process could allow the creation of Ramsey interferometers that use superradiance to maintain coherence [140] or transfer coherence between atomic clock-like ensembles.

1.3 Spin Squeezing with Cavity-Aided Measurements

I also describe a system for cavity-enhanced collective quantum non-demolition (QND) measurements of the population of ^{87}Rb atoms. These collective measurements can generate a high degree of entanglement between atoms, leading to partial cancellation of quantum noise of a quantity of interest. This effect, known as spin squeezing, is a way of exploiting quantum entanglement between the atoms to enhance precision measurements with atoms. Prior QND measurement experiments that generated spin squeezing showed that near-resonant light could still have a high enough degree of non-destructiveness to create entanglement [32, 110], and that eliminating back-action from noise in state-changing Raman transitions could generate an order-of-magnitude improvement (a factor of 10.5) in phase enhancement compared to an unentangled ensemble [16]. By improving the quality of the QND measurement, it may be possible to achieve another order of magnitude in phase enhancement. To this point, we have observed up to 25 times enhancement in variance of the phase, and it may be possible soon to achieve a factor of 50 or greater [42].

1.3.1 Measuring Atomic Spins

Precision measurements with atoms generally rely on measuring the relative quantum phase ϕ between two atomic states $|\uparrow\rangle$ and $|\downarrow\rangle$ in a superposition state $|\psi\rangle = a|\downarrow\rangle + be^{i\phi}|\uparrow\rangle$. The quantum phase ϕ is not directly measurable, but can be mapped onto observable quantities. In steady state superradiance, the atomic phase ϕ is directly related to the phase of emitted light ψ and measuring ψ serves as a continuous non-destructive measurement of the atomic coherence. For collective non-demolition population state measurements, as in spin squeezing, the phase ϕ can be mapped onto the population of atoms in the spin states, $N_\uparrow$ and $N_\downarrow$.

A convenient representation for both kinds of measurements is the Bloch vector. The Bloch vector is a classical three-dimensional vector that represents the quantum state of one or many spin-1/2 systems. For a pure quantum spin state $|\psi\rangle = \cos(\frac{\theta}{2})|\uparrow\rangle + e^{i\phi}\sin(\frac{\theta}{2})|\downarrow\rangle$, it is represented as a vector with length 1/2, polar angle $\theta \in [0, \pi)$, and azimuthal angle $\phi \in [0, 2\pi)$. In Cartesian coordinates, the Bloch vector $\langle\hat{\mathbf{s}}\rangle = \frac{1}{2}(\langle\hat{\sigma}_x\rangle, \langle\hat{\sigma}_y\rangle, \langle\hat{\sigma}_z\rangle) = (s_x, s_y, s_z) = \frac{1}{2}(\sin(\theta)\cos(\phi), \sin(\theta)\sin(\phi), \cos(\theta))$, where $\hat{\sigma}_k$ label the Pauli spin matrices. For N atoms, a collective Bloch vector $\langle\hat{\mathbf{J}}\rangle$ can be defined as the vector sum

$$\langle\hat{\mathbf{J}}\rangle = \sum_{i=1}^{N}\langle\hat{\mathbf{s}}^{(i)}\rangle, \tag{1.1}$$

where i is an index over individual atoms. The relative quantum phase ϕ is the quantity of interest for atomic sensors, as it can change in response to external fields, or in the case of atomic clocks, is set purely by the energy level difference between $|\uparrow\rangle$ and $|\downarrow\rangle$, which can be made very stable. Coherent spin states (CSS) are the idealization of the states used in many quantum measurements. A CSS is composed of N atoms in the same pure quantum state such that $|\psi_{CSS}\rangle = \bigotimes_{j=1}^{N}\cos(\theta/2)|\uparrow\rangle_j + \sin(\theta/2)e^{i\phi}|\downarrow\rangle_j$, as shown in Figure 1.3.

1.3.2 Quantum Noise in Measurements of Atomic Spins

The other key component in this description is quantum noise. A fuzzy blob at the tip of the Bloch vector represents the width of the probability distribution of measurement outcomes resulting from quantum noise, shown in Figure 1.3. The signal-to-noise or angular uncertainty comes from comparing the noise in a given spin component to the length of the Bloch vector. For a CSS on the equator of the Bloch sphere, the root-mean-square (RMS) size of the angular uncertainty distribution is $\Delta\theta = \Delta J_z/|\vec{J}|$. This noise scales in the large N limit as $\Delta\theta = \Delta\phi = 1/\sqrt{N}$. This scaling is known as the Standard Quantum Limit (SQL) and arises from the binomial statistics of "flipping quantum coins" or collapse into $|\uparrow\rangle$ and $|\downarrow\rangle$ due to measurement. Note that the relative size of the uncertainty distribution in Figure 1.3 is not to scale with our experiment, as with $N = 10^6$ atoms the SQL 1 milliradian.

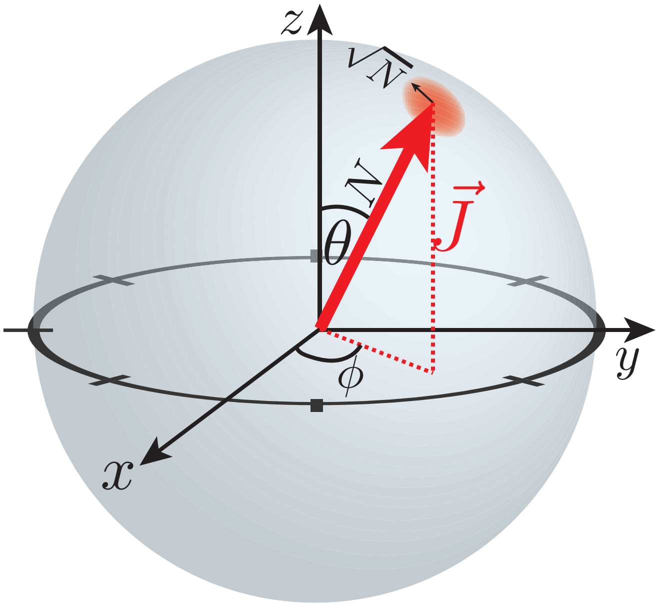

Figure 1.3: Depiction of a coherent spin state (CSS) on the Bloch sphere. The length of the Bloch vector is N and the RMS noise in its pointing angle is $\sqrt{N}$, leading to a fractional quantum noise of $1/\sqrt{N}$. The Bloch vector has polar angle θ from the z-axis and has azimuthal angle ϕ.

The atomic phase ϕ needs to be mapped onto an observable quantity for it to be measured. In our Raman superradiant laser system, ϕ can be inferred from the phase ψ of the light emitted in superradiance. Perturbations to atomic energy levels from fluctuating magnetic fields cause fluctuating precession of ϕ and therefore ψ with respect to a stable frequency reference. Application of coherent microwave transitions and a controllable dark evolution period during which time the dressing lasers are turned off can translate the narrow detection band of the scheme to higher frequencies while minimizing the effect of dephasing on contrast loss.

In the context of interferometers based on atoms, a standard method for mapping the quantum phase ϕ onto spin state population is Ramsey interferometry [104]. Optical pumping removes entropy before a sensing sequence and puts the atoms into a well-defined state (such as $|\downarrow\rangle$). Coherent radiation (e.g., microwaves or a laser) is applied to create a $\pi/2$ pulse to bring the atoms to the equator of the Bloch sphere so that ϕ may precess relative to the local oscillator (LO) that performed the initial $\pi/2$ pulse. Finally, another $\pi/2$ pulse about a rotation axis close to the Bloch vector takes the Bloch vector off of the equator and gives it a non-zero J_z. The z-component of the resultant Bloch vector indicates the phase deviation between the LO and the Bloch vector having precessed. The expectation value $\langle \hat{J}_z \rangle = (N_\uparrow - N_\downarrow)/2$ (using the definition of the Pauli spin matrix $\hat{\sigma}_z$). The result is that in the Ramsey mathod, the problem of measuring a quantum phase is translated into a problem of measuring atomic populations.

Population measurements can be performed with fluorescence measurements, as in ion traps [127, 98], or optical lattice clocks [15, 61]. However, these projective measurements destroy the coherence of the sample, to taking the atoms out of a superposition state by projecting the atoms into either a bright state (e.g., $|\uparrow\rangle$) or a dark state ($|\downarrow\rangle$). Fluorescence measurements also usually require scattering many photons for good signal-to-noise in the detection process, and the resulting photon recoils can cause loss of atoms from a trap due to heating. Repeated measurements then require another round of state preparation. One way to circumvent this is to perform collective measurements that do not provide which-atom information. These kinds of quantum non-demolition measurements are how we generate entanglement between our ^{87}Rb atoms. By only getting information about how many atoms are in $|\uparrow\rangle$, we do not cause single-atom collapse and still have a signal ($|\vec{J}| \gg 1/\sqrt{N}$) that can be used for a precision measurement.

Our QND measurement takes the form of measurements of cavity frequency. Atoms within the cavity mode cause a phase shift of light that effectively changes the optical path length of the cavity. This leads to an atom-number dependent change in the resonance frequency of the cavity compared to the bare cavity containing no atoms. This frequency shift alone contains no which-atom information.

1.3.3 Squeezing Quantum Noise

A key challenge in the context of precision measurements is to improve upon the quantum shot noise level. Squeezing of quantum noise was first demonstrated in light [117], yet there have been few practical demonstrations of measurements enhanced with squeezed light. Laser gravitational wave interferometers (GEO600 and LIGO) have used squeezed light to improve sensitivity to strain induced by gravitational waves at acoustic frequencies by about 3 dB [128, 1]. Enhancement in biological imaging of about 14% in spatial resolution was also recently achieved using squeezed light [125].

In atomic systems, spin squeezing can reduce the quantum noise level in one spin quadrature at the expense of increased noise in an orthogonal quadrature [67]. Techniques for generating inter-atom correlations necessary for spin squeezing include atomic collisions [26, 56, 100, 97], qubit entangling gates [76, 77, 96, 95], and collective measurements in free space [3, 112] or optical cavities [110, 16, 32]. Twisting-type interactions can also be applied in optical cavities through a feedback mechanism between the collective atomic spins and the light shift inside the cavity [78]. A useful metric for expressing the degree of phase enhancement is to compare the improvement relative to the SQL. Figure 1.4 shows a partial summary of the field of quantum phase enhancement, where the results are presented without subtraction of technical background noise. That is, it presents not the inferred degree of entanglement but the degree of entanglement that will actually enhance a precision measurement in the presence of actual experimental imperfections.

Our method for measuring atomic spin populations is effective because it reduces back-action associated with state-changing transitions [33, 16] that limited prior work [32, 110]. We utilize an optical cycling transition to probe the atoms to prevent state-changing transitions. The major source of back-action is then loss of coherence due to free-space Rayleigh scattering, as free space scattered photons reveal the spin state of individual atoms to the environment. The work presented

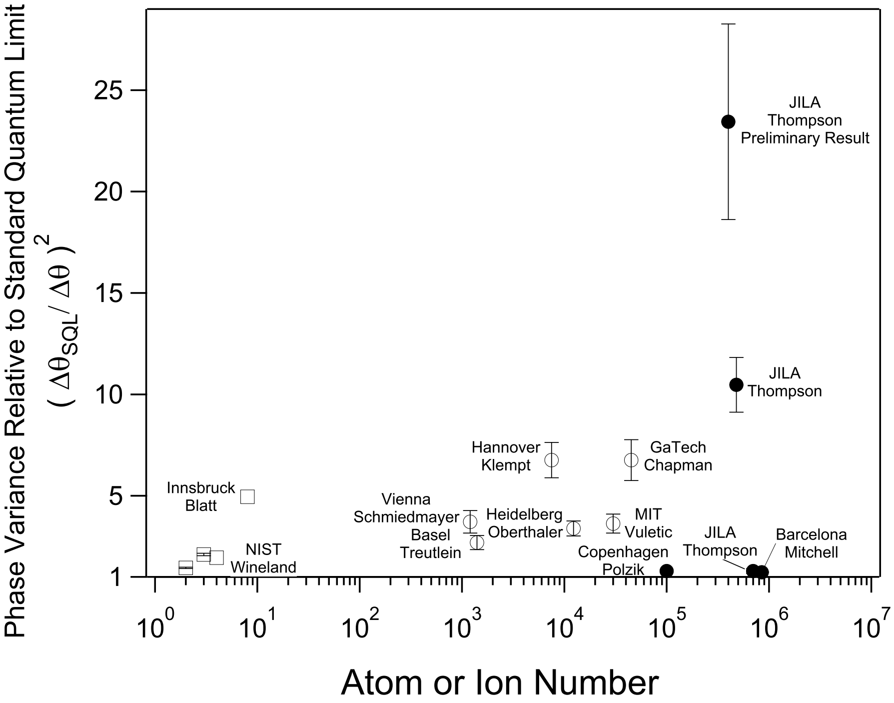

Figure 1.4: A summary of the directly observed entanglement-enhanced estimation of a quantum phase relative to the Standard Quantum Limit versus the number of atoms used. A value of 1 on the y-axis corresponds to no enhancement. This plot presents the results without readout noise subtraction, so the values displayed are lower than some of the reported values for inferred entanglement generation. Solid circles (●) represent experiments that used coherence-preserving measurements in optical cavities [110, 16, 32] or in free space [3, 112]. Open circles (○) used atomic collisions to generate non-linear twisting or parametric interactions [26, 56, 100, 97] or twisting interactions in an optical cavity [78]. Open squares (□) used quantum logic interactions in ion traps to generate Schrödinger Cat states [76, 77, 96] or squeezed states [95].

in this thesis focuses on technical improvements to the probing scheme that eliminates a large degree of relative laser frequency-cavity frequency noise and improves the effective quantum efficiency q of the probing. High q is important for a QND measurement as it means, for fixed incident photon number M_i interacting with the atoms, there is less of a contribution of photon shot noise to the noise in the measurement.

1.4 Organization of Thesis

The structure of this thesis is as follows. First, in Chapter 2, I describe in more detail the physics of steady state superradiance, including linewidth predictions and theoretical models. These concepts were developed in experiments performed during the early years of my doctoral studies. I proceed in Chapter 3 by describing the essential features of our experimental apparatus. The material presented in Chapters 2 and 3 is useful for understanding the details of later chapters.

Next, in Chapter 4, I describe the operation of and characterize the performance of a proof-of-principle sensor of magnetic fields based on a superradiant ensemble of atoms. Since the frequency of emitted light is set by both the energy difference between $|\uparrow\rangle$ and $|\downarrow\rangle$ and the dressing laser frequency, changes in the ground state splitting can be detected as changes in the frequency of the output light. We utilize magnetic-field-sensitive ground states and observe the output light to infer the change in magnetic field at the location of the atoms. A key feature of this sensor is its capability of operating in two regimes: steady state, high bandwidth sensing and a dark, narrowband lock-in mode.

Chapter 5 describes experiments that characterize the manner of synchronization between two spatially separate atomic ensembles undergoing steady state superradiance in the same optical cavity. By breaking the phase or frequency degeneracy of the lasers, we can observe the output light to once again infer the changes in the collective atomic dipoles' phases. This system is also explored in two regimes: in real time as the phase degeneracy between the two ensembles is abruptly broken, and the steady state configuration as the frequency difference between the lasers is changed.

Chapter 6 describes some initial experiments to generate large amounts of entanglement—

the next generation of cavity-aided spin squeezing. Setup for these experiments involved important modifications of the experimental system and breaking vacuum for the first time in several years as part of moving the entire experiment to a new wing of JILA. In the scheme presented here, we expect that an enhancement in phase resolution of 14 dB is possible, with more enhancement of up to 17 dB possible with straightforward technical improvements. I conclude in Chapter 7 with prospects for future squeezing experiments, and briefly describe a scheme for entanglement-enhanced atom interferometry in our optical cavity.

Chapter 2

Steady State Superradiance Overview

To date, there have been several experimental [24, 19, 20, 18, 133] and theoretical [93, 21, 65] investigations of steady state superradiance. This chapter, by reviewing some previous work on superradiance, establishes some shared concepts that are useful for understanding the material in Chapters 4 and 5.

2.1 Technology Promise: Toward MilliHertz Linewidths

One of the most compelling reasons to study steady state superradiance is the superior spectral properties that are predicted. State-of-the-art lasers built for interrogating optical transitions with high coherence times for optical lattice clocks have linewidths of tens of mHz compared to their resonant frequencies of several hundred THz. These lasers then have Q factors in excess of 10^{17} [99]. Impressive progress along these lines continues, but the technical challenges are significant, with the state of the art now requiring cooled mono-crystalline cavities and the ultimate linewidth limitation being thermal fluctuations of the mirror coating [39].

Since the superradiant laser will use natural high-Q oscillators (atoms) as the phase flywheel, rather than the optical cavity, it provides a way of sidestepping the engineering challenges associated with stable optical cavities. The ultimate Schawlow-Townes linewidth of the superradiant laser (in Hz) is $C\gamma/\pi$, with the quantity γ in units of rad/s. This expression has a simple physical interpretation: the cooperativity C is the fraction of solid angle subtended by the cavity mirrors times the cavity finesse [123], so the linewidth is set by the rate $C\gamma$ of spontaneously emitted photons ending up in the cavity mode. The cooperativity C can be less than one, so that the ultimate linewidth of the laser is less than the natural linewidth of the atoms—which for Sr is about 1 mHz and Yb is ~ 10 mHz. The first demonstration of a Raman superradiant laser showed that the linewidth of the light emitted by the atoms was below that of any known source of broadening, but the predicted linewidth was not observed [24].

2.1.1 Insensitivity to Cavity Frequency

Although the ideal superradiant laser linewidth is limited by the atomic decay rate, in any real application there will be a contribution from cavity instabilities. In some sense, the primary purpose of the cavity field is to serve as an infinite-range communication bus between atoms to allow synchronization of the atomic dipoles. But emitted photons still interact with the cavity mirrors so any motion of the cavity mirrors (or a deviation of the cavity resonance frequency) can disrupt the phase stability of the emitted light.

There is a pulling coefficient $P = 2\gamma_\perp/\kappa = W/\kappa$ that sets the sensitivity of the emitted photon frequency ω'_γ to that of the cavity center frequency ω_c and unperturbed emission frequency ω_γ through $\omega'_\gamma = \omega_\gamma + P(\omega_c - \omega_\gamma)$. Here, W is the repumping rate from the ground to excited lasing state. In the bad cavity regime of the experiments presented in this thesis, $P \sim 10^{-4}$ to 10^{-2}. In a good cavity laser, $P = 1$ as the cavity frequency sets the lasing frequency. This means that the technical requirements on engineering a stable cavity are much less stringent than in state-of-the-art lasers.

2.1.2 Atomic Coherence and Emitted Light

A key feature of superradiance is the mapping of atomic coherence onto the coherence of the emitted light. There is a direct relationship between the relative atomic coherence $\phi(t)$ between lasing states $|\uparrow\rangle$ and $|\downarrow\rangle$ and the phase of emitted light $\psi(t)$ such that $\phi(t) = \psi(t)$ up to an overall constant phase offset. The light phase then serves as a non-destructive measure of the non-directly-observable atomic phase ϕ and the equatorial quadrature $J_\perp$, which otherwise would have to be rotated to the z-axis to be observable in our system.

2.1.3 Collective Bloch Sphere

This section introduces explicitly the Bloch vector picture for the collective atomic state and its relationship to the coherently emitted light. The relationship between atomic coherence and the emitted light is crucial for understanding the later Chapters 4 and 5. A convenient picture is the collective Bloch sphere, a classical vector composed of a weighted average of the atomic dipoles

$$\vec{J} = \frac{\sum_{j=1}^{N} g_j^2 \vec{S}_j}{\sum_{j=1}^{N} g_j^2}, \tag{2.1}$$

where $2g_j$ is the single-photon Rabi frequency from the Jaynes-Cummings Hamiltonian for the jth atom and $\vec{S}_j$ is a three-vector representing an atomic spin with components $(\langle\hat{S}_x\rangle, \langle\hat{S}_y\rangle, \langle\hat{S}_z\rangle)$ defined by the expectation values of operators

$$\begin{aligned} \hat{S}_x &= \frac{1}{2}(\left|\uparrow\right\rangle\left\langle\downarrow\right| + \left|\downarrow\right\rangle\left\langle\uparrow\right|) \\ \hat{S}_y &= \frac{i}{2}(\left|\downarrow\right\rangle\left\langle\uparrow\right| - \left|\uparrow\right\rangle\left\langle\downarrow\right|) \\ \hat{S}_z &= \frac{1}{2}\left(\left|\uparrow\right\rangle\left\langle\uparrow\right| - \left|\downarrow\right\rangle\left\langle\downarrow\right|\right). \end{aligned} \tag{2.2}$$

The expression for $\vec{J}$ in Equation 2.1 includes inhomogeneous coupling, allowing for the g_j to vary. A convenient parametrization of the Bloch sphere is to define it by length and polar and azimuthal angles $\vec{J} = |J|\,(\sin(\theta/2)\cos(\phi), \sin(\theta/2)\sin(\phi), \cos(\theta/2))$. In the Raman superradiant laser, the phase of the optical dipoles $\alpha = \phi + \beta$, so that the relative phase ϕ between atomic ground states is mapped onto the light, as shown in Figure 2.1. Another useful picture for superradiance is splitting it up into z-component $J_z = (N_\uparrow - N_\downarrow)/2$ and equatorial plane component $J_\perp = J_x + iJ_y$. Then, J_z indicates the level of inversion and the electric field phasor emitted by the superradiant ensemble $A(t)e^{i\psi(t)}$ is directly proportional to the complex transverse component $J_\perp e^{i\phi(t)}$.

In the Raman system, it is possible to turn off the dressing laser to effectively stop the lasing process from continuing. This allows the atomic coherence to be "frozen" and potentially manipulated with microwaves to create sensors (as in Chapter 4) or explore the effect of repumping modulation on J_z and $J_\perp$ [19].

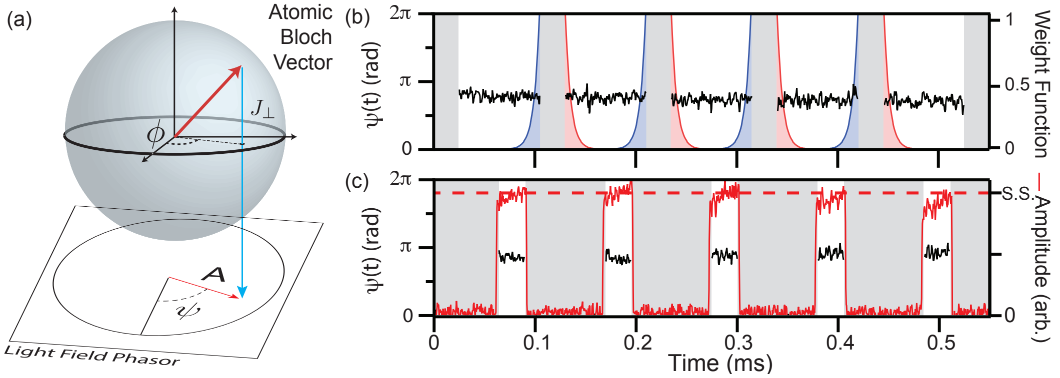

Figure 2.1: Mapping of the Bloch vector equatorial projection onto the emitted light phasor. (a) Atomic Bloch vector with phase ϕ and equatorial projection $J_\perp$ directly setting the light phase ψ and amplitude A. (b) Light phase ψ versus time when the Raman dressing laser and repumping beams are turned on (black line) or off (gray boxes). Exponential weighting of the phase data for optimal phase noise is represented by the blue and red curves. (c) Amplitude $A(t)$ (red trace) versus time with a longer dark time between periods of bright evolution.

As discussed in Ref. [20], the limitations to the capability of light measurements for estimating $J_\perp$ at a given point in time are phase diffusion and photon shot noise. In order to estimate the phase $\phi(t)$, it is necessary to average the time record of the light phase $\psi(t)$ over some time T_m. Increasing the averaging time T_m reduces photon shot noise at the cost of increasing the noise from phase diffusion of $J_\perp(t)$. However, it was shown that an optimal Kalman filter can be constructed to measure $\phi(t)$ to the equivalent standard quantum limit given a certain level of inversion (i.e., the projection of a fractional $\Delta\theta = 1/\sqrt{N}$ noise distribution onto the equatorial plane, given a certain level of inversion J_z that tilts the Bloch vector up out of the plane). This filter is simply an exponential weighting with time constant $\tau_w = 1/\sqrt{q}NC\gamma$, where q is the quantum efficiency of the detection system.

2.2 Models for Superradiance

Depending on the level of detail required, there are a few different useful models for steady state superradiance. A full quantum master equation analysis can provide useful information about the effects of quantum noise. The more computationally tractable optical Bloch equations, where expectation values of operators are considered and higher-order quantum correlations are ignored, can give useful insights into the behavior of the system and capture most of the crucial qualitative detail.

2.2.1 Hamiltonian for Atom-Cavity System

The Jaynes-Cummings Hamiltonian [83] describes the coupling of an ensemble of two-level spins to a single harmonic oscillator, the light field of the cavity mode.

$$\hat{H} = \hbar\omega_c \hat{c}^\dagger \hat{c} + \hbar g(\hat{c}^\dagger \hat{J}_- + \hat{c}\hat{J}_+). \tag{2.3}$$

Here, ω_c is the resonance frequency of the cavity mode. The operators $\hat{c}$ and $\hat{c}^\dagger$ are the annihilation and creation operators, respectively, for photons in the cavity mode. The single photon Rabi frequency is $2g$ and is determined by the atomic dipole matrix element and the cavity mode volume [83]. The collective atomic raising and lowering operators are $\hat{J}_{\pm}$.

We define a density matrix $\hat{\rho} = \sum_{kl} \sum_{m,n=0}^{\infty} |k,n\rangle \langle l,m|$, where k,l label atomic basis states and (m,n) label the photon Fock states. The time evolution of $\hat{\rho}$ is determined by the master equation

$$\dot{\hat{\rho}} = \frac{1}{i\hbar}[\hat{H},\hat{\rho}] + \mathcal{L}[\hat{\rho}]. \tag{2.4}$$

The Lindlbad super-operator $\mathcal{L}[\hat{\rho}]$ [25] includes the effects of dissipation from a few different sources: cavity photons escape through the mirrors at rate κ, incoherent repumping from $|\downarrow\rangle$ to $|\uparrow\rangle$ happens at rate W, and spontaneous emission still occurs at rate γ. The full expressions are contained in Appendix A. Since a laser must have more than just two energy levels, the repumping process actually takes atoms from $|\downarrow\rangle$ to $|\uparrow\rangle$ through at least one other optically excited state $|3\rangle$.

For an operator $\hat{O}$, the expectation value $O \equiv \langle \hat{O} \rangle$ is given by $O = \mathrm{Tr}[\hat{O}\hat{\rho}]$. The time variation of O is given by $\dot{O} = \mathrm{Tr}[\hat{O}\dot{\hat{\rho}}]$, where $\dot{\hat{\rho}}$ comes from the master equation. The frequency of the emitted photon is ω_γ, and the frequency difference between $|\uparrow\rangle$ and $|\downarrow\rangle$ is $\omega_{\uparrow\downarrow}$. Here, $\dot{E} = \mathrm{Tr}[\hat{c}\dot{\hat{\rho}}]$ is the expectation value of the cavity annihilation operator ("E" as a mnemonic for "electric field"). Finally, the symbol $\widetilde{\ }$ indicates that the quantity is in a frame rotating at the frequency of the emitted light ω_γ as, e.g., $E = \widetilde{E}e^{-i\omega_\gamma t}$. The coupled atom-field equations are then

$$\dot{\widetilde{E}} = -(\frac{\kappa}{2} + i(\omega_c - \omega_\gamma))\widetilde{E} - ig\widetilde{J}_- \tag{2.5}$$

$$\dot{\widetilde{J}}_- = -(\gamma_\perp + i(\omega_{\uparrow\downarrow} - \omega_\gamma))\widetilde{J}_- + i2g\widetilde{E}J_z \tag{2.6}$$

$$\dot{J}_z = -(W+\gamma)\frac{J_z}{2} + (2\Gamma_{3e} - W + \gamma)\frac{N_3}{4} + \frac{N}{4}(W-\gamma) + ig(\widetilde{J}_-\widetilde{E}^* + \widetilde{J}_+\widetilde{E}) \tag{2.7}$$

$$\dot{N}_3 = -(\Gamma_{3e} + \frac{W}{2})N_3 + W(\frac{N}{2} - J_z) \tag{2.8}$$

The quantity $\gamma_\perp = \gamma/2 + W/2 + \Gamma_R/2$ represents all the broadening terms from spontaneous decay, repumping, and background decoherence. For our experiments, $\gamma_\perp$ is dominated by the repumping rate W. The corresponding energy levels and frequencies are illustrated in Figure 2.2 and Figure 2.3.

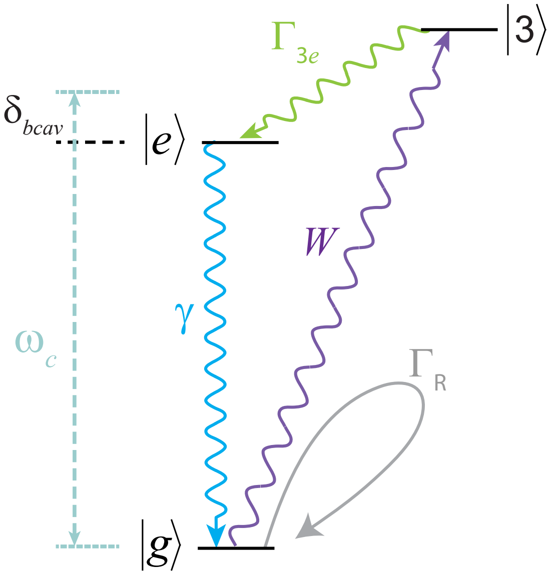

Figure 2.2: Energy level diagram for the three-level system presented in Equations 2.5 to 2.8. Spontaneous decay is at rate γ, decay from $|3\rangle$ to $|e\rangle$ is at Γ_{3e}, and W is the repumping rate out of $|g\rangle$. A decoherence rate Γ_R affects $|g\rangle$.

2.2.2 Raman Laser Equations

The model introduced in the previous section is an adequate description of a 3-level laser, but in our experiments, we use a Raman system. A dressing laser detuned from an excited optical intermediate state $|\mathrm{i}\rangle$ causes decay between the metastable hyperfine ground states of ^{87}Rb. The Hamiltonian for the Raman system depicted in Figure 2.3 is

$$\hat{H} = \hbar\omega_c \hat{c}^\dagger \hat{c} + \hbar\omega_\mathrm{i}\hat{N}_\mathrm{i} + \hbar\omega_\uparrow \hat{N}_\uparrow + \hbar\omega_\downarrow \hat{N}_\downarrow + \hbar\frac{\Omega_d(t)}{2}(\hat{J}_{\uparrow\mathrm{i}} + \hat{J}_{\mathrm{i}\uparrow}) + \hbar g(\hat{c}^\dagger \hat{J}_{\downarrow\mathrm{i}} + \hat{c}\hat{J}_{\mathrm{i}\downarrow}). \tag{2.9}$$

Here, $\Omega_d(t) = \Omega_d(e^{-i\omega_d t} + e^{i\omega_d t})$, where ω_d is the frequency of the dressing laser. The frequencies ω_c and ω_i are the frequencies of the cavity mode and the excited optical state, respectively. The frequencies of $|\uparrow\rangle$ and $|\downarrow\rangle$ are $\omega_\uparrow$ and $\omega_\downarrow$. The operators $\hat{J}_{mn}$ are collective raising and lowering operators, exchanging an excitation in state $|n\rangle$ for one in $|m\rangle$. In this model, the dressing field is unaffected by the atoms. With this Hamiltonian, the master equation (Equation 2.4) can be used to derive the equations of motion for expectation values of operators again. Since the detuning Δ is large, the optically excited state population is eliminated to generate the coupled equations

$$\dot{E} = \left(-\frac{\kappa}{2} - i\left(\frac{g^2}{\Delta}N_\downarrow + \omega_c\right)\right)E - i\frac{g\Omega_d}{2\Delta}J_{\downarrow\uparrow}e^{-i\omega_d t} \tag{2.10}$$

$$\dot{J}_{\downarrow\uparrow} = \left(-\gamma_\perp - i\left(\frac{\Omega_d^2}{4\Delta} - \frac{g^2|E|^2}{\Delta} + \omega_{\uparrow\downarrow}\right)\right)J_{\downarrow\uparrow} + i2\frac{g\Omega_d}{2\Delta}J_z E e^{i\omega_d t} \tag{2.11}$$

$$\dot{J}_z = W(N/2 - J_z) + i\frac{g\Omega_d}{2\Delta}(E^* J_{\downarrow\uparrow}e^{-i\omega_d t} - E J_{\uparrow\downarrow}e^{i\omega_d t}). \tag{2.12}$$

In these equations for the Raman system, the term $\frac{g\Omega_d}{2\Delta}$ appears as the effective two-photon coupling g_2. Correspondingly, the effective decay rate from $|\uparrow\rangle$ to $|\downarrow\rangle$ is approximately

$$\gamma = \frac{\Gamma}{4}\left(\frac{\Omega_d}{\Delta}\right)^2 \tag{2.13}$$

when the detuning Δ is large compared to Γ. Also, the term $\frac{g^2}{\Delta}N_\downarrow + \omega_c$ corresponds to a shifted or dressed cavity mode due to atoms in the ground state $|\downarrow\rangle$. Finally, an AC Stark shift from the dressing laser and intracavity electric field cause a perturbation $\omega_{ac} = \frac{\Omega_d^2}{4\Delta} - \frac{g^2|E|^2}{\Delta}$ to the splitting between the two lasing states $|\uparrow\rangle$ and $|\downarrow\rangle$. The equations can be rewritten more simply by writing them in the frame of the effective atomic frequency $\omega_a = \omega_{\uparrow\downarrow} + \omega_{ac} + \omega_d$ with detuning of the cavity $\delta_c = \omega_c - \omega_a$ as

$$\dot{E} = -\left(\frac{\kappa}{2} + i\delta_c\right) E - ig_2 J_- \tag{2.14}$$

$$\dot{J}_- = -\gamma_\perp J_- + i2g_2 J_z E \tag{2.15}$$

$$\dot{J}_z = -W J_z + \frac{N}{2} W + ig_2 \left(J_- E^* - J_-^* E\right). \tag{2.16}$$

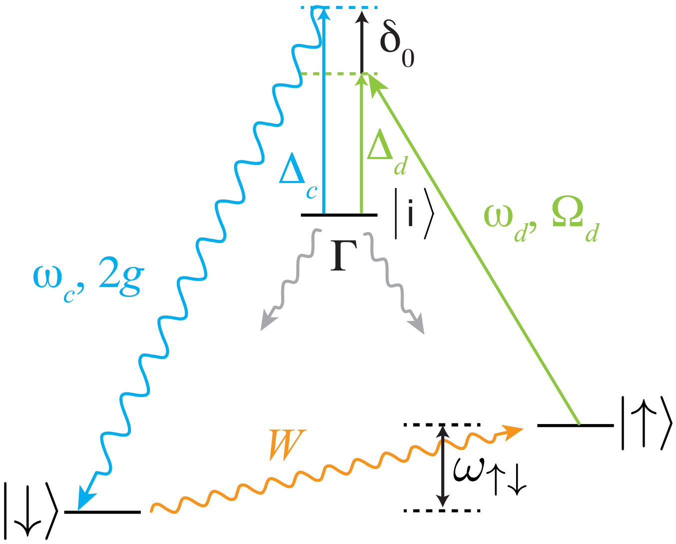

Figure 2.3: Energy level diagram for the Raman laser scheme. A drive laser with Rabi frequency Ω_d and detuning Δ_d from the excited state allows decay from $|\uparrow\rangle$ to $|\downarrow\rangle$. The cavity is detuned Δ_c away from $|\mathrm{i}\rangle$ leading to a detuning $\delta_0 = \Delta_c - \Delta_d$ between the cavity mode and $\omega_d + \omega_{\uparrow\downarrow}$.

A simple dynamical picture, based on the geometric interpretation of the Schrödinger equation [51], for the operation of the superradiant laser at the single-atom level is the following:

(1) In steady state, the collective Bloch vector is pointing somewhere in the northern hemisphere.

(2) Atom k, upon undergoing a repump event, is taken from the global superposition state into $|\uparrow\rangle$. Because N is large, the collective Bloch vector is perturbed very little.

(3) The persistent intracavity field torques the Bloch vector of atom j to be in line with the steady state Bloch vector.

In this picture, the effect of quantum noise is to cause diffusion of the azimuthal phase ϕ in time as fluctuations in the light field cause fluctuations in the time evolution of the atomic Bloch vectors.

2.3 Power Output and Quenching

Since the superradiant laser relies on atomic coherence, and repumping destroys coherence, steady state light emission is a balance between putting energy back into the system from repumping and allowing the synchronization mechanism to happen.

The total transverse broadening $\gamma_\perp = \Gamma_D/2+W/2+\gamma/2$, where $\Gamma_D = 1/T_2$ is the background decoherence rate. This sets the lower threshold for lasing—when W exceeds Γ_D, the atoms are being repumped faster than coherence is re-established through the electric field radiated by all the other atoms. The intracavity field becomes strong enough to build up phase alignment between optical dipoles faster than it can be destroyed.

The Bloch vector picture qualitatively explains the upper quenching behavior of steady state superradiance in response to a changing repump rate W. Unlike in a conventional laser, where a highly broad gain medium has $J_z \approx 0$ in steady state, a superradiant laser's output ceases with too much inversion. This is because the atomic coherence, or equivalently, $J_\perp$, is driven to zero as the Bloch vector aligns to the z-axis. Before a persistent intracavity field can be established, a repump event takes atoms back to $|\uparrow\rangle$. Figure 2.4 shows the output power in units of intracavity photon number as a function of repumping rate W in units of the collective emission rate $NC\gamma$.

2.4 Stability and Relaxation Oscillations

An interesting feature of the Raman system is the interaction between dispersive shifts of the cavity mode and stability. Stability constraints restrict the regime of cavity detunings that are experimentally feasible. Our Raman superradiant laser acts in a regime where the detuning is still small enough for collective dispersive shifts of the cavity mode, given by $\omega_c' = \omega_c + Ng^2/\Delta$, to shift the dressed cavity mode by a large fraction of κ. Since the dressing laser does not necessarily have the same detuning relative to the dressed cavity mode plus the hyperfine splitting, the cavity

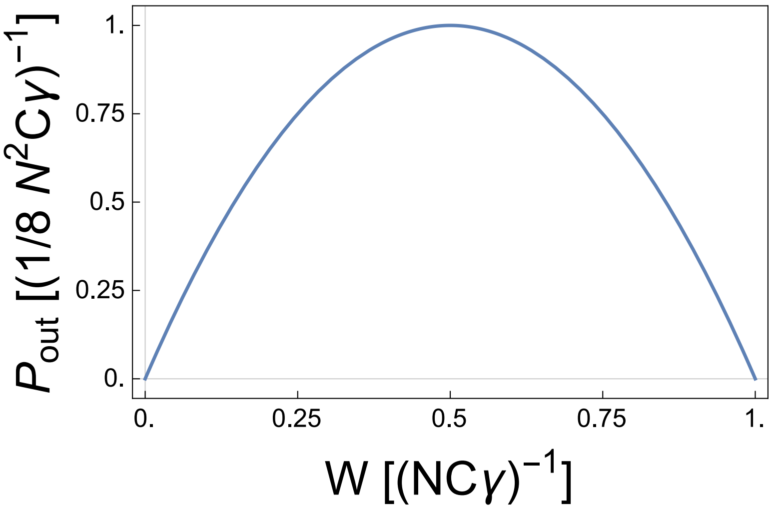

Figure 2.4: Theoretical plot of output power vs. repump rate for a superradiant ensemble. There is a quadratic scaling with W and maximum $\frac{1}{8}N^2C\gamma$ occurs at $W/(NC\gamma) = 1/2$. The upper quench threshold corresponds to the repump rate overtaking the stimulated decay, leaving the system fully inverted and with no projection $J_\perp$.

frequency changes relative to the emitted photon frequency. This changes the effective cooperativity $C' = C/(1+(\delta_c/(\kappa/2))^2)$ such that the collective emission rate $NC'\gamma$ can change, which in turn changes the inversion (or tipping angle θ of the Bloch sphere) and may shift the cavity frequency yet again. It is clear that this feedback mechanism could lead to instability in the emitted light from the laser.

However, the relative sign of the feedback mechanism can change based on which side of cavity resonance the ensemble starts off in. If initially the emitted photon frequency were blue of the cavity, emission would cause the cavity to shift to the blue. This would bring the cavity even more blue (since atoms in $|{\downarrow}\rangle$ create a larger shift) and increase C', increasing the emission rate further: a runaway process that prevents stable operation with the emitted photon blue of the cavity. In the opposite case, when the emitted photon frequency is red of the dressed cavity mode, the sign of the feedback can be negative and stable operation can be reached.

There is also a fundamental time delay in the system, owing to the repumping process. In the real Rb system there are multiple paths for the atoms to take until their internal state reaches the dark state $|{\uparrow}\rangle$. The response of the inversions and the output light phasor to repumping modulation was studied in Refs. [24, 22]. The modulation is expressed in the model of Equation 2.16 by substituting $W \to \bar{W}(1+\epsilon\mathrm{Re}[e^{i\omega t}])$ and introducing another level $|3\rangle$ with population N_3. By analyzing the effect of first-order perturbations, a set of damped, driven harmonic oscillator equations can be derived for $j_{z,\perp}$ which indicate a $\bar{W}$-dependent resonance frequency and damping rate.

Chapter 3

Experimental Apparatus

This Chapter briefly describes the apparatus that was used to perform the experiments described in later chapters. Many details of the apparatus have been described previously in the theses of Chen [31] and Bohnet [17]. As is typical of a modern atomic physics experiment, we rely heavily on ultra-high vacuum (UHV) systems, multiple laser systems, data acquisition and analysis software, and JILA-built control electronics, as well as circuits developed in the lab for very specific purposes.

At the heart of the experiment, however, are our quantum spins (^{87}Rb atoms) confined within an optical cavity. The atoms must be cold enough to have well-defined motional properties on the timescale of our experiments and reside in the cavity with long enough coherence times that we can prepare the atoms, probe them, and perform other experiments with them. A great deal of work collectively by our lab members has gone into opto-electronic systems that can probe features of the light-atom interactions, usually geared towards detecting the phase shift of light applied to or emitted by the atoms, with a noise floor well below that of fundamental quantum noise.

In the summer and fall of 2014 (the fifth year of my Ph.D.), the Rb experiment moved from the second floor of JILA to the basement of the new JILA X Wing. Just prior to and during the move and re-assembly, some crucial pieces of the experiment were modified. The second half of this section details the changes and additions to the apparatus that will be used in a next generation of spin squeezing experiments.

3.1 Vacuum System

The vacuum system has two major pieces, separated by a bellows that extends through the optics table. Above the table surface, there is a spherical cube (Kimball Physics MCF450-SS20400) to which two AR-coated windows, vacuum feedthrough for electronics, and a glass rubidium reservoir are attached. The reservoir, heated to 70–90 °C, creates a thermal vapor inside the science cell. The science cell, a 2" (outer dimension)×2" (o.d.)×10" Borofloat glass rectangular prism attached to a glass-to-metal seal, is also attached to the top of the spherical cube. A bellows extends below the table and connects to a 5-way cross to which the Ti-sub pump, ion pump, ion gauge, and turbo/roughing pump are attached.

A good vacuum system is crucial for long lifetimes of the atoms in the optical trap, so that the limiting atom loss process is not due to collisions with background gas. We performed initial pump-down with a dry scroll pump (Varian IDP-3 Dry Scroll Pump[1] , pumping speed 60 L/min) backing a turbo-molecular pump (Varian Turbo V 81-M, 75 L/s). After the bake, an ion pump (Varian VacIon Starcell 50 L/s, PN 9191340) maintains the pressure at around 2×10^{-10} Torr.

3.2 Science Cavity

A high-finesse optical cavity is crucial for creating a high effective optical depth to create a stronger link between the atoms and the cavity mode than to free space modes. The following description of the science cavity corresponds to the apparatus used prior to August 2014. Chapters 4 and 5 use this cavity mirror configuration. The science cavity with finesse[2] $F \approx 700$ is formed by two mirrors (Advanced Thin Films coating runs v2-1128 through v2-1130) mounted to a low-thermal-expansion Zerodur cavity spacer, residing in the science cell and mounted on a vibration isolation stage. The mirrors are highly reflective at 780 nm (power transmission $T = 2011$ ppm), 795 nm ($T = 2122$ ppm) and 823 nm ($T = 3400$ ppm). The cavity length, and therefore optical

---

[1] This model of vacuum pump seems prone to a failure mode in which its ultimate pressure (and likely, pumping speed) can degrade suddenly.

[2] The finesse decreased over a number of years, from 710 in 2009 to 660 in 2014, due to Rb and sputtered wire coating sticking to the mirror surfaces, causing round-trip losses.

resonance frequency, is controlled by applying voltage to two piezo-electric cylinders (Piezomechanik PZT-5H) to which the mirrors are attached with TorrSeal epoxy. The cavity is shown in Fig. 3.1.

For the spin squeezing experiments of Chapter 6, the cavity mirrors were replaced to create a near "closed" cavity. In this configuration, the top mirror has $T_2 = 131$ ppm at 780 nm while the bottom mirror has $T_1 = 2011$ ppm. A summary of the frequency-dependent cavity parameters is given in Table 3.2. Also, the PZT's were exchanged for flatter cylindrical stack piezos (Piezomechanik HPCh150/12-6/2) with higher bandwidth and more throw per applied volt. A closed cavity configuration allows the cavity phase response to be detected in reflection from only the open side of the cavity, reducing the number of places that technical noise floors can affect the measurement and allowing higher quantum efficiency (because of an anti-reflection coated vacuum window on the bottom side). Instead of having to use multiple detectors with potentially different noise floors and quantum efficiencies and path length stabilization schemes, we can use just one detector. The mirrors were wrapped in thin wire (Kurt J. Lesker PN: FTAK01410, 0.14 mm OD) to heat the mirrors to prevent Rb from sticking to them [116]. In order to mitigate mechanical forces resulting from changing flux through the heater wire coils, 8 counter-winding coils were used on each mirror, secured with epoxy (Epo-Tek H70E thermally conductive). Due to the number of different epoxies used and their curing schedules requiring heat, we originally found during assembly that small flecks of epoxy got onto the mirror surfaces and broadened the linewidth by around 1 MHz. Successive cleaning stages in the plasma cleaner in the Keck Lab seemed to remove almost all of this extra loss, although small defects were still visible on the mirror surface.

Table 3.1: Summary of the new cavity parameters used in experiments after August 2014.

Parameter	Value
Free spectral range ν_{FSR}	8090(1) MHz
Transverse mode spacing	2295(1) MHz
Cavity length L	1.8578(2) cm
Mirror radius of curvature	5.00(1) cm
Rayleigh range z_R	1.9425(2) cm

Table 3.2: Summary of the new cavity transmission coefficients used in experiments after August 2014.

Parameter	780 nm	795 nm	823 nm
Measured Linewidth (with Rb vapor) (MHz)	3.01	–	–
Design linewidth (MHz)	2.76	2.88	4.61
Mode Waist (μm)	69.5	70.2	71.4
Mode Volume (cm^3)	7.02×10^{-5}	7.16×10^{-5}	7.41×10^{-5}
Open mirror transmission T_1 (ppm)	2010.9	2122.3	3400
Closed mirror transmission T_2 (ppm)	131.2	116.7	180
Fractional loss through T_2 (empty cavity)	5.6×10^{-2}	–	–

Figure 3.1: Photographs of the first ("old") optical cavity (left) and the new optical cavity (right). The new cavity has shorter piezos on top of spacers that kept the cavity spacing approximately constant. The top mirror is only 6% as transmissive as the bottom mirror, which has the same transmission coefficient as before (see Table 3.2). Also, thin heater wires are wrapped around each mirror and attached with thermal epoxy.

3.3 Cooling and Trapping the Atoms

The first step in the experiments is the formation of a magneto-optical trap (MOT). Applying red-detuned light from the optical cycling transition in ^{87}Rb in three dimensions cools the atoms through repeated photon absorption and emission. Application of a spherical quadrupole magnetic field that increases in magnitude with distance from the center of the trap causes the atomic energy levels to shift closer to resonance with the cooling beams, resulting in more scattering with distance from the trap center. These two effects lead to a spatially and velocity dependent damping force that traps atoms and cools them approximately to the Doppler temperature T_D of 140 μK, limited by the linewidth of the optically excited $5^2P_{3/2}$ state by

$$T_D = \frac{\hbar\Gamma}{2k_B}, \tag{3.1}$$

where $\Gamma = 2\pi \times 6.06$ MHz is the decay rate of the excited optical state and k_B is Boltzmann's constant [80].

To generate our MOT, we use a tapered amplifier (TA) chip (Eagleyard EYP-TPA-0780-00500-3006-CMT03-0000) to amplify an input beam of 18 mW derived from an external cavity diode laser (ECDL) or distributed Bragg reflector laser (DBR) to about 150 mW of optical power to the atoms. The beam is then split into six free-space paths (three pairs of counter-propagating paths) with approximately equal power of 25 mW to balance radiation pressure in the MOT and optical molasses. The waist of each beam is about 0.8 cm.

The shape of the MOT is very sensitive to beam alignment because of mm-scale fringes of 50% peak-to-peak intensity variation. These fringes cause radiation pressure imbalances that result in spatially inhomogeneous density, especially at the edge of the MOT cloud. In principle, the fringing effects could be mitigated by changing out spherical lenses for large aspheric lenses, but the fractional peak-to-peak trapped atom number fluctuations are still around a couple percent even with the fringes. Likely, the fluctuations are due to fluctuations on the laser wavelength scale of the relative path lengths along each beam path that cause fluctuating interference fringes at the location of the atoms.

Once the atoms have been loaded into the MOT, they are further cooled with polarization gradient cooling (PGC), a kind of “Sisyphus cooling” that allows for sub-Doppler temperatures [45]. In this step, the spherical quadrupole magnetic fields are turned off and Helmholtz bias coils shim out background magnetic fields (including Earth’s magnetic field), creating zero field at the location of the atoms. Applying counter-propagating laser fields in each direction with σ^+ and σ^- polarizations creates a spatially varying polarization. As an atom moves through the polarization gradient, it sees a spatially varying AC Stark shift on its ground state energy levels—essentially, a level repulsion coming from second-order perturbation theory. As the atom reaches a maximum in the spatially varying potential, its probability to scatter increases and it is optically pumped into a different state that has a minimum in energy in its light shift. This optical pumping effect happens many times to the atoms—rolling “up the hill”, getting pumped into a dark state at the bottom of a “hill,” and then rolling “up the hill” again (this is the “Sisyphus” part). In principle, this cooling is at the limit of the recoil energy of the photons at 780 nm of 0.4 μK, but we see temperatures of 20–40 μK.

During the cooling stages, there is a far off-resonant red-detuned optical lattice beam resonant in the cavity. The optical cavity still has a finesse of about 600 at the optical lattice wavelength of 823 nm, so the intra-cavity intensity at the peak of the standing wave is on the order of 1.3×10^4 Watts/cm^2. The light shift from the lattice creates a negative shift in the ground state energy levels of the atoms, leading to potential energy minima at antinodes of the standing wave. The atoms collect in these pancake-shaped trap regions. In the axial direction, the trapping potential from the lattice varies on the wavelength scale, and in the transverse direction it varies on the scale of the waist (70 μm) of the beam. Because the atoms are colder (tens of μK) than the trap depth ($\approx$ 300 μK) of the lattice potential, they are confined within a few tens of nm in the axial direction and 10-20 μm in the transverse or radial directions. The lattice has a similar waist to the lasers at the 780 nm and 795 nm transitions, so the atoms have near-maximal coupling to the probe and dressing beams with respect to the transverse direction. Importantly, there is residual harmonic motion ($\omega_{\text{axial}} \approx 2\pi \times 250$ kHz, $\omega_{\text{radial}} \approx 2\pi \times 800$ Hz for 1 Watt circulating) of the atoms in both the axial and radial directions. These mechanical oscillations are important for understanding opto-mechanical effects and setting an equivalent noise floor for very precise measurements of the resonant frequency of a coupled atom-cavity system, as in spin squeezing.

3.4 Probing Schemes

Measuring the phase shift of light is a task we encounter frequently in the lab. This comes up in, e.g., measuring the properties of light emitted by superradiance or measuring the number of atoms in a given spin state through the phase shift imposed on light shone through the atoms. Since the frequency of our optical signals is a few hundred THz, there isn't a detector fast enough to detect every single oscillation of the electromagnetic field. However, by using a superposition of the light field of interest and a stronger local oscillator (LO) beam offset by 200 MHz or less, we can translate the problem of detecting a phase at optical frequencies to one of detecting an RF electronic signal phase–a technique known as heterodyne measurement. Homodyne measurement, in which the LO frequency is degenerate with the probe frequency, is briefly discussed in the context of a spin squeezing experiment in Chapter 7. Once the light phase signal is encoded in an oscillating RF current at the photodetection step, we can demodulate the full phasor response in both the I and Q quadrature and construct a phasor $\mathcal{E}(t) = I(t) + iQ(t) = A(t)e^{i\psi(t)}$, creating a representation of the electric field phasor $E(t)$.

For the superradiance experiments presented in Chapters 4 and 5, there is a dressing laser field at a frequency lower than the emitted light by about the hyperfine splitting, $\Delta_{hf} = 2\pi \times 6.834$ GHz. To account for the frequency difference, we use electro-optic modulators (EOSPACE PN: PM-0S5-10-PFAPFA-780-UL) to put a LO frequency component near the emitted light's frequency or an applied cavity probe's frequency. Figure 3.2 shows a representative probing scheme corresponding to the experiments of Chapter 4, which is modified for the experiments of Chapters 5 and 6.

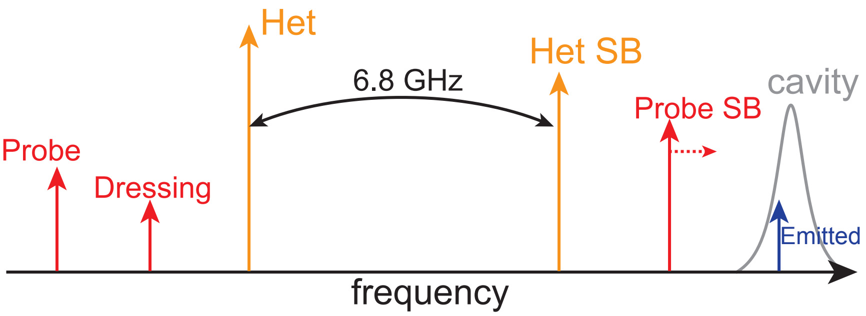

Figure 3.2: General schematic of frequency components relative to the heterodyne LO. The dressing beam is red of the emitted photon by about 6.8 GHz due to the hyperfine frequency between $|\uparrow\rangle$ and $|\downarrow\rangle$. Microwave sidebands slightly above 6.8 GHz provide a sideband within 150 MHz of the emitted photon frequency, so an RF beatnote can be generated. A probe sideband is swept over the cavity for cavity frequency shift measurements.

3.5 Heterodyne Detector

We build the heterodyne detectors with a reverse-biased photodiode (typically, Hamamatsu S5973) and a wideband, low-noise transimpedance amplifier (Analog Devices AD8015). The reverse-biased photodiodes have a smaller capacitance (1.5 pF) and larger response bandwidth (500 MHz) than an unbiased diode. With low input capacitance, the AD8015 has a smaller noise floor (which rises at larger frequencies due to the smaller impedance of the photodiode capacitance). A typical current noise density is 2.5 $\mathrm{pA}/\sqrt{\mathrm{Hz}}$ at 50 MHz with the S5973 photodiode. At this current, the signal would become photon shot noise-limited at a LO beam power of about 40 μW (from the relation $\tilde{I} = \sqrt{2q_eI_0}$ (units of $\mathrm{A}/\sqrt{\mathrm{Hz}}$), where q_e is the electron charge and I_0 is the photocurrent of the LO beam).

3.6 MOT and Repumper DBR Lasers

Crucial to the experiments described in later chapters are the lasers used for cooling the atoms into the lattice. We use two Photodigm PD780DBR080T8-S distributed Bragg reflector (DBR) diode lasers at 780 nm for loading the magneto-optical trap and performing polarization gradient cooling (PGC) when the atoms are loaded into the optical lattice. Although our DBR lasers tend to operate with linewidths of ≈ 1 MHz, higher than the ECDLs, we find their stability and robustness to be more important than their linewidth properties in their capacity as cooling lasers. The DBR lasers tend to be very susceptible to frequency pulling from optical feedback, so we use two opto-isolators for each laser to obtain a high degree (> 60 dB) of isolation. We use aspheric collimating lenses (ThorLabs PN: C230TMD-B) in aluminum mounts that are glued (Loctite 495) directly onto the diode's TO-8 can to eliminate long-term drift that we saw in cage-mounted collimating lenses. The lasers are housed in the manufacturer-supplied test mount setups (Photodigm TO8-1000-A). Standard JILA-built laser controllers (#TJ002-09 for MOT, #TJ002-10 for Repumper) are used for both current and temperature controllers.

The lasers are overlapped with the modulation transfer spectroscopy (MTS) 780 nm reference laser to form beatnotes for offset locks. Since these lasers are used in multiple cooling stages and sometimes in state preparation, agile control of the lasers' frequencies is necessary. With the beatnote locks, we can scan the laser frequencies across the entire excited hyperfine manifold for both the MOT ($F = 2$) and Repumper ($F = 1$) lasers.

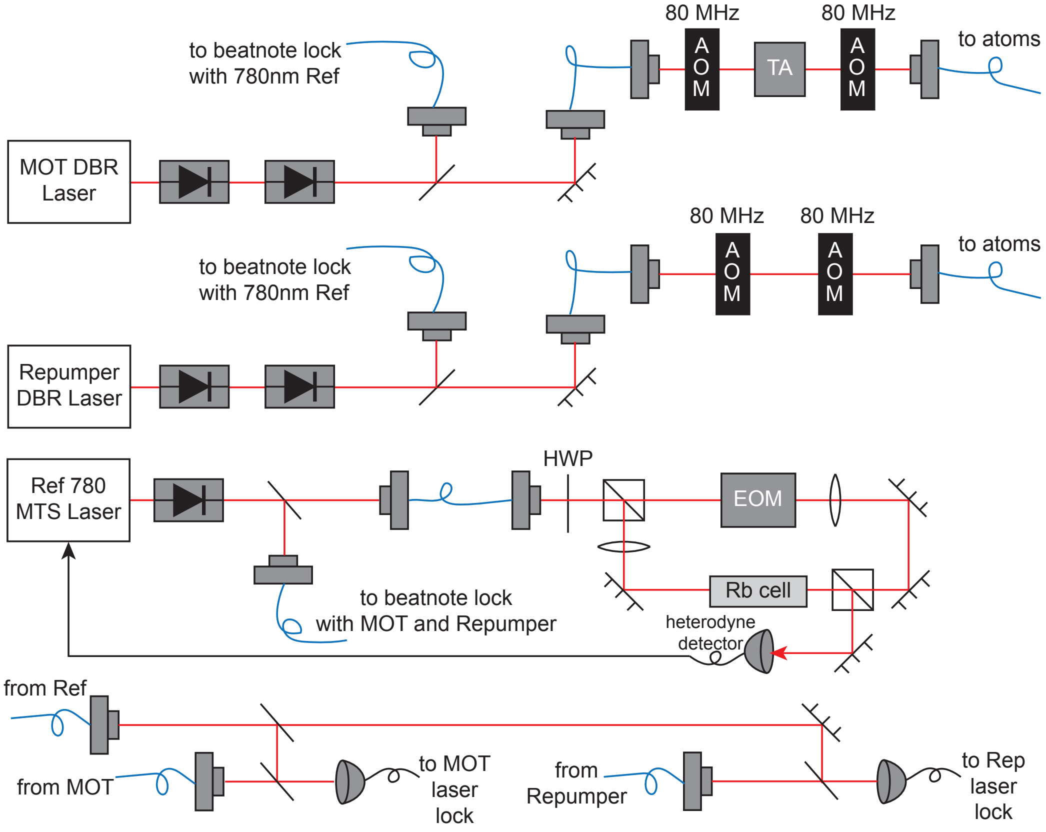

Figure 3.3: Diagram of MOT DBR laser, Repumper DBR laser, and Modulation Spectroscopy Reference and beatnote locks. The MOT laser is sent through two isolators to prevent optical feedback and has a small amount of light picked off and sent to a beatnote lock with the 780nm modulation spectroscopy laser. The MOT light is sent through a tapered amplifier to provide an optical molasses for the MOT. The Repumper laser also has two isolators and a pickoff for frequency stabilization. The modulation transfer spectroscopy reference is stabilized to the cycling transition in ^{85}Rb and overlapped with some MOT light and Repumper light to provide feedback to the MOT and Repumper lasers for stabilization.

3.7 Microwave Source

To perform coherent manipulations of the atoms between the $|\uparrow\rangle$ and $|\downarrow\rangle$ states, we use a stub-tuned dipole antenna (resonant frequency 6.76 GHz, $Q = 24$) placed close to the vacuum cell. In general, we would like the classical phase noise imposed by rotations to be much less than the fundamental quantum noise of $1/\sqrt{N}$ in radians. We therefore drive the dipole antenna with a custom microwave source with low noise (-130 dBc/Hz at 10 kHz offset [35]). The microwaves are generated by phase-locking a low-noise crystal oscillator (Wenzel Sprinter 501-04517) at 100 MHz to a 10 MHz Rb clock (PN: Stanford Research Systems FS725/3).

3.8 Direct Digital Synthesis (DDS)

Part of the convenience of working with RF signals is the mature technologies that allow manipulation and detection of RF fields. We utilize nearly a dozen direct digital synthesis (DDS) boards, which rely on digital chips and digital-to-analog converters to produce amplitude, phase, and frequency-agile RF tones from < 1 MHz to 230 MHz. The Analog Devices AD9959 chip provides 4 phase-synchronous channels with very good phase noise properties for a relatively small cost compared to a full-featured signal generator. These DDS boards can be programmed using LabView to drive serial communication to change their output signals during an experimental sequence and therefore are convenient to provide most of the modulation (AOMs, EOMs, mixing stages, etc.) in the experiment where the phase noise requirements are strict.

The boards can be programmed both through a serial port (SPI) or through a USB port, which actually drives a micro-controller (Cypress CY7C68013A-56PVC) on the evaluation board that translates the USB commands to SPI commands. When the AD9959 evaluation board is plugged into a Windows computer, some firmware is automatically uploaded to the Cypress micro-controller and it is capable of USB communication with the Analog Devices evaluation software. Matt Grau of the Cornell eEDM group was able to package that firmware into a driver for Windows 7 64-bit, which allows communication with the AD9959 evaluation boards over USB through a

LabView interface. This is useful since we were never able to get frequency sweeps working with the boards under serial control. Frequency sweeps are crucial for running the experiment, but with only the Analog Devices evaluation software it is not possible to update the frequency sweep settings synchronously with each iteration of the experiment.

3.9 Data Acquisition System

Most aspects of the experiment are controlled and monitored by a National Instruments (NI) LabView program, “Master.vi,” built for our lab. LabView provides convenient software for performing run-by-run analysis at the 1 Hz repetition rate of the experiment. Analog and digital outputs and inputs are handled with NI acquisition cards, whose properties are summarized in Table 3.3. The fast multi-channel analog input card (PN: NI PCI-6133) is used for sampling in heterodyne photodiode signals for superradiance and squeezing. Since each quadrature I and Q requires a separate channel each, the 8 fast inputs allow for 4 demodulated quadrature heterodyne signals total. The digital output card (PN: NI PCIe-6259) ought to be able to run at 10 MHz update rate but in practice, setting the clock to 4 MHz creates more reliability. The timing resolution of our microwave pulses is set by the 250 ns step size for the 4 MHz update rate of the card.

Table 3.3: Summary of the data acquisition cards used for the experiment.

Card	Type	No. of Inputs/Outputs	Bandwidth
NI PCI-6133	Analog Input (AI)	8	2.5 MSamples/s
NI PCI-6733 (×2)	Analog Output (AO)	8	1 MS/s
NI PCIe-6259	Digital Output/AO/AI	32/4/16	4 MHz/700 kS/s

3.9.1 Imaging Systems

Cameras are very useful for being able to take pictures of our atoms, even though we don’t rely critically on imaging systems for most of our data. We have used fluorescence imaging, for instance, to measure the spatial distribution of the atoms once they have been loaded into the lattice. Having a picture of a transverse Gaussian laser mode, too, is incredibly convenient for laser beam characterization, mode matching, and statements about optical cavity properties. Our lab has two gigabit ethernet (GigE) cameras, one CCD sensor (Basler Scout scA640-70gm) and a CMOS sensor (Basler Scout scA750-60gm). The cameras have similar capabilities and their sensors have similar spectral responses, but the CMOS sensor has more noise. Another LabView program, similar to Master.vi, allows for trial-by-trial fitting and analysis, with typical capture rates of 20 frames per second over the network. While the cameras are smaller and more expensive than commercially available CCDs (i.e., from DSLRs), they have programmable exposure times from 24 μs to several ms and image acquisition can be triggered with TTL pulses, allowing easy synchronization within experimental sequences.

3.10 Frequency Stabilization

Both our superradiance and spin squeezing experiments depend crucially on frequency stabilization of lasers and cavities. Laser stabilization is necessary to control the relative detuning of probe light or dressing light and dressed cavity or atomic resonance, and is useful for reducing acoustic and electrical noise on lasers. This section describes the overall frequency lock chain after the lab was disassembled and moved to X1B21 in the JILA X Wing in Summer and Fall 2014.

Figure 3.4 is a diagram describing the chain of frequency stability, with approximate bandwidths for each lock. The low-frequency stability is derived from locking to an atomic transition ($2-3'$ in ^{87}Rb for the modulation transfer spectroscopy and the $3-4'$ crossover feature in ^{85}Rb for the 795 nm FM Spectroscopy), and translated to other frequencies via offset beatnote locks between lasers or Pound-Drever-Hall locks between lasers and cavities and *vice versa*.

3.10.1 Beatnote Locks

The idea behind a beatnote lock is to generate a heterodyne RF signal through the direct overlap of two lasers onto a photodiode. Because the photodiode current $I \propto P \propto |E|^2$, a cross-term at the difference frequency can be within the detection bandwidth of the photodiode. Stabilizing

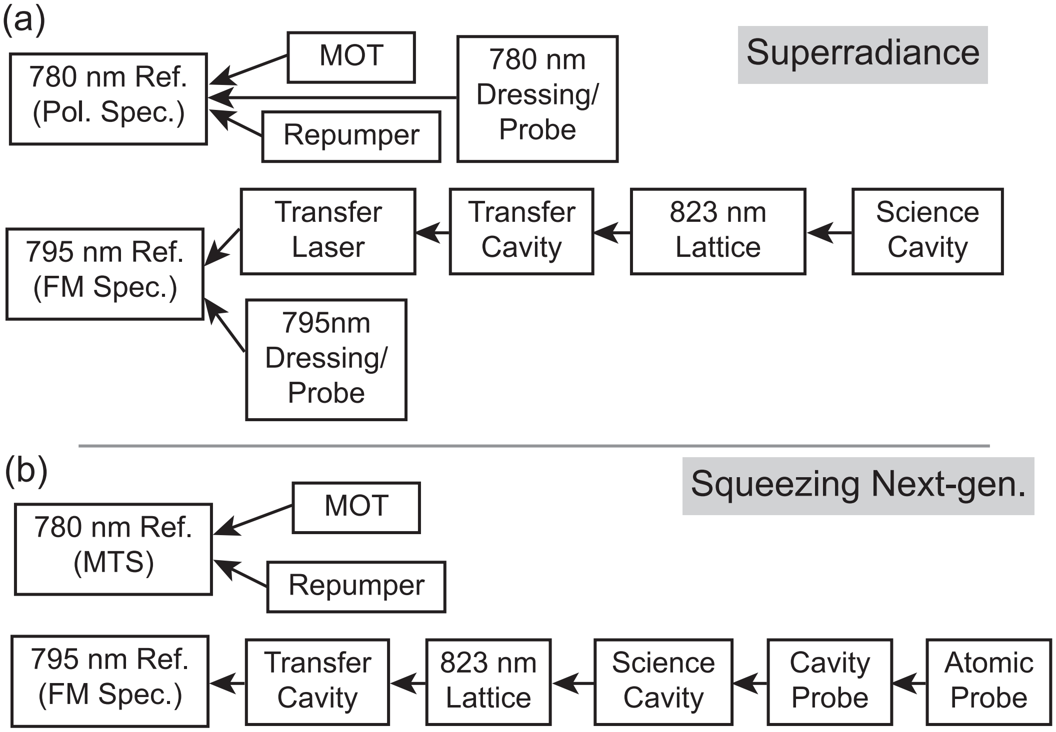

Figure 3.4: A schematic of the frequency stabilization chain for superradiance and future spin squeezing experiments. (Top) The stabilization schemes corresponding to the experiments in Chapters 4 and 5. (Bottom) Stabilization scheme for the next generation of spin squeezing experiments. Note that the chain ultimately locked to the 795 nm FM spectroscopy laser is an artifact of iterating from the first squeezing experiment by Chen *et al.* [31], and could be replaced by a lock to the MTS laser.

the phase of this beatnote frequency to a quiet reference (provided by DDS) stabilizes the phase of a laser to a reference laser to within a bandwidth of $\approx$ 1 MHz. Practically, this is quite a useful technique that allows for high-bandwidth, highly tunable locks over a broad frequency range of $\sim$ 20 MHz to 2.5 GHz offsets.

A representative beatnote lock of two ECDL lasers with free-running linewidth 200 kHz is shown in Figure 3.5. The corner frequencies and gain settings for the corresponding loop filter (JILA TJ011) are given in Table 3.4.

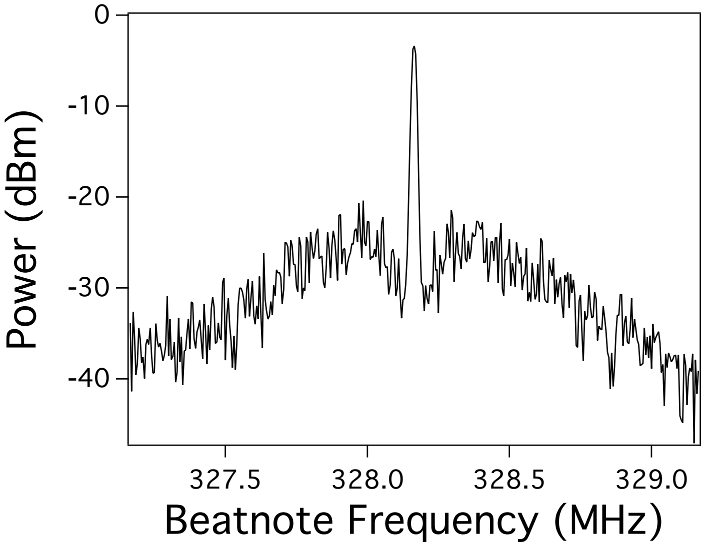

Figure 3.5: Power spectrum of a beatnote lock between two ECDL lasers with span 2 MHz. This power spectrum was generated via a single sweep on a spectrum analyzer with no averaging. Vertical axis is in dBm and horizontal axis is the frequency in MHz. For this trace, the spectrum analyzer video bandwidth (VBW) = resolution bandwidth (RBW) = 10 kHz and the full span is 2 MHz. Lock settings are given in Table 3.4.

3.10.2 Modulation Transfer Spectroscopy

Atomic spectroscopy is a valuable tool for establishing frequency stability of a laser at acoustic frequencies and below. Locking diode lasers to Doppler-free spectroscopy features in vapor cells is how we derive DC stability for our frequency chains. This section describes a robust method for locking one of the spectroscopy setups.

Table 3.4: Lock settings for TJ011 loop filter for the ECDL beatnote lock with spectrum shown in Figure 3.5.

Setting	Value
Gain 1	0 dB
Gain 2	-10 dB
1st PI	70 kHz
2nd PI	50 kHz
D	0.5 MHz

The essential concept of MTS is the transferring of the sidebands that carry information about the optical phase shift imposed on the probe light by the atoms to the pump beam, through a Bragg scattering-like process [89]. This spectroscopy technique is much less sensitive to power level drifts than the previous polarization spectroscopy setup that was used from 2008 - 2014, which was highly sensitive to DC drifts of optical power, alignment, and polarization. MTS ends up being most sensitive to the cycling transitions in both isotopes of Rb: $\left|5^2S_{1/2}, F = 2, m_F = 2\right\rangle \rightarrow \left|5^2P_{3/2}, F' = 3, m_F = 3\right\rangle$ at 780 nm in ^{87}Rb and $\left|5^2S_{1/2}, F = 3, m_F = 3\right\rangle \rightarrow \left|5^2P_{3/2}, F' = 4, m_F = 4\right\rangle$ in ^{85}Rb. The ^{85}Rb transition has higher signal-to-noise than the ^{87}Rb transition because of its higher natural abundance (75% compared to 25%), and is convenient for forming beatnote locks for other lasers that address ^{87}Rb because it is 1126 MHz blue of $\left|5^2S_{1/2}, F = 2, m_F = 2\right\rangle \rightarrow \left|5^2P_{3/2}, F' = 3, m_F = 3\right\rangle$ in ^{87}Rb. This avoids having beatnotes near DC where our PFDs function less reliably and results in a broad tuning range that allows the locked lasers to span the excited hyperfine manifold. Fig. 3.6 is an example error trace when the laser is swept across both cycling transitions.

During the lab move, the biggest change from an initial setup was the addition of more compact telescopes, which allows the probe beam to sample more atomic vapor to increase the signal-to-noise of the error signal. The pump contains about 1 mW and the probe has 1 mW with a $1/e^2$ waist of ≈ 2.35 mm for both beams. The modulation frequency is 5.2 MHz, chosen empirically to maximize the error signal size.

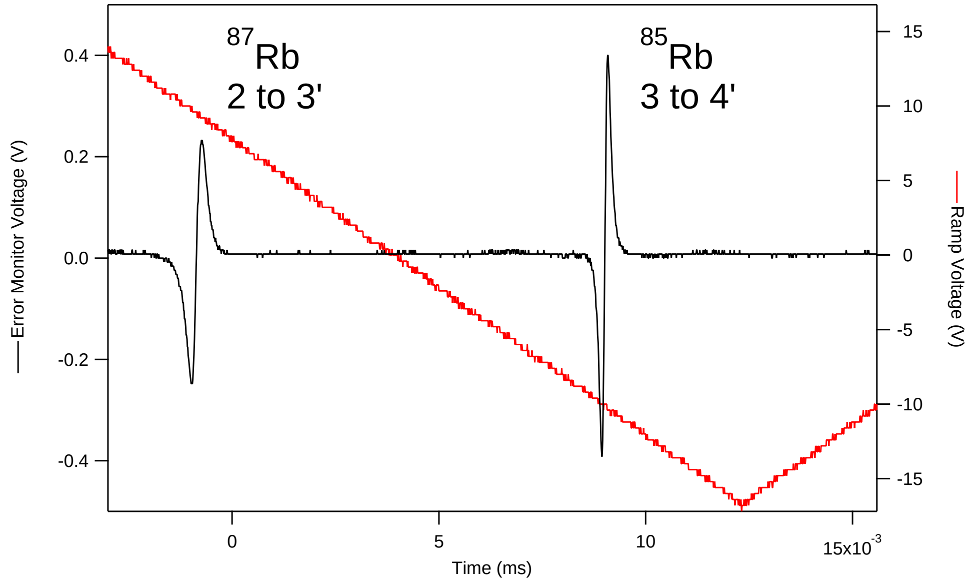

Figure 3.6: An oscilloscope trace showing a representative 780 nm MTS reference error signal and accompanying sweep, with the transitions labeled. Optical frequency increases from left to right. The sweep rate is 114 MHz/ms and the error signal has a lowpass filter with bandwidth 100 kHz.

3.10.3 Transfer Cavity Lock

A high-finesse Transfer Cavity is stabilized using the Pound-Drever-Hall (PDH) technique [14] to feed back on the resonant frequency of the cavity so that it is resonant with the 795 nm FM Spectroscopy reference laser. The same 27 MHz sidebands that are used to create the FM spectroscopy error signal allow PDH locking of the Transfer Cavity to the 795nm reference laser. A high-voltage amplifier provides feedback to a PZT (Pizeomechanik PZT-5H) that controls the length of the cavity to keep the cavity on resonance with the FM Spectroscopy laser. Figure 3.7 shows a representative error signal for the transfer cavity lock.

3.10.4 Lattice to Transfer Cavity Lock

In order to stabilize the frequency of the 823 nm lattice laser, the Pound-Drever-Hall technique is used to lock the Lattice laser to the Transfer Cavity. The supplied current to the 823 nm is modulated at 10 MHz to generate sidebands on the laser for both PDH locking to the Transfer

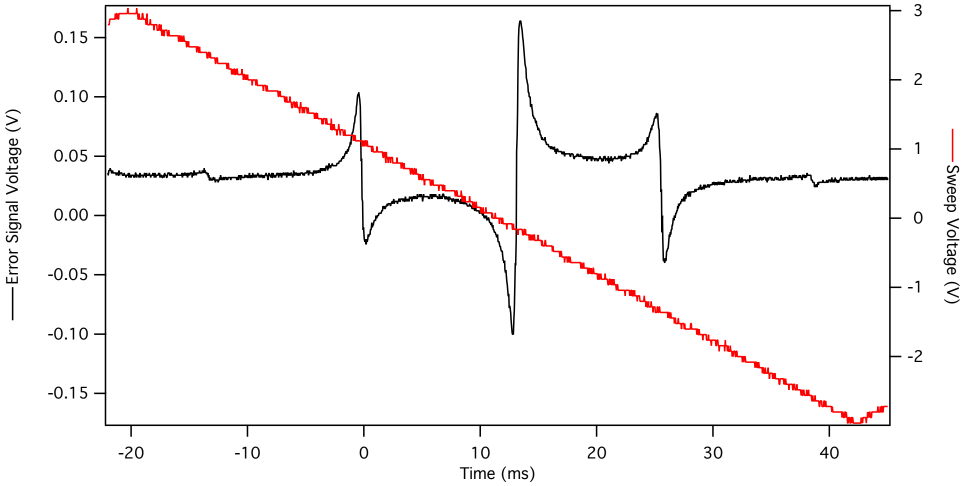

Figure 3.7: Example Pound-Drever-Hall error signal for the transfer cavity-to-FM spectroscopy laser lock. Error signal is black, sweep is red. The optical sweep rate for the transfer cavity is 2.1 MHz/ms and the error signal had a lowpass filter with bandwidth 100 kHz.

Cavity and for the UHV Cavity to lock to the lattice. Before being sent to the Transfer Cavity, the 823nm laser is also sent through an EOSPACE EOM that is modulated at 5.5 - 9.2 GHz by a wideband microwave VCO (described in Section 3.11). Then, either the red or blue sideband of the lattice laser is locked to the Transfer Cavity. As the microwave sideband frequency changes, the absolute optical frequency of the Lattice laser changes. Figure 3.8 shows a diagram of the lattice laser microwave sideband lock.

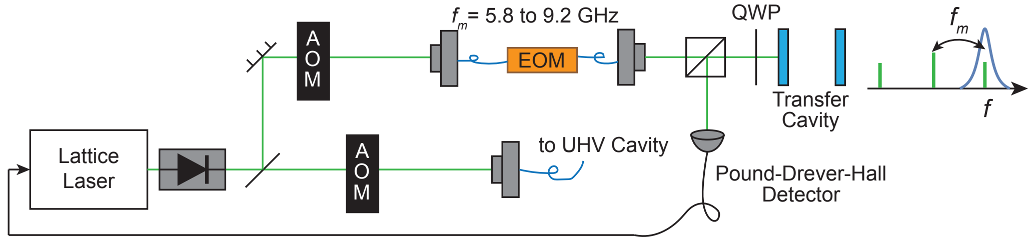

Figure 3.8: Diagram of the lattice laser-to-transfer cavity Pound-Drever-Hall lock. After passing through an isolator (and an AOM for more isolation), a fiber-coupled EOM puts sidebands on the lattice. One of these sidebands, tunable in frequency, is locked to the cavity. A 10 MHz signal puts sidebands on the 823nm lattice laser carrier, which persist on the high-frequency sidebands and are used for locking.

The power into the EOM is set so that the fraction of optical power in the microwave sidebands is near a local maximum (the fractional sideband strength is given by the square of the first Bessel function $J_1^2(\beta)$), and the modulation index is held constant with the use of a variable attenuator (Hittite #HMC346MS8G) because both the response of the EOM and the output power of the VCO vary with frequency. The constant power prevents the magnitude of the error signal slope, and therefore the open-loop gain of the feedback loop, from changing. Figure 3.9 shows a representative Pound-Drever-Hall error signal trace for one of the lattice sidebands.

3.11 Microwave Voltage Controlled Oscillators

Several microwave voltage controlled oscillators (VCOs) are employed in the experiment for many uses, including phase modulating laser beams with EOMs and providing local oscillators for high-frequency mixing stages. Since the ^{87}Rb hyperfine splitting is ≈ 6.8 GHz, wideband VCOs

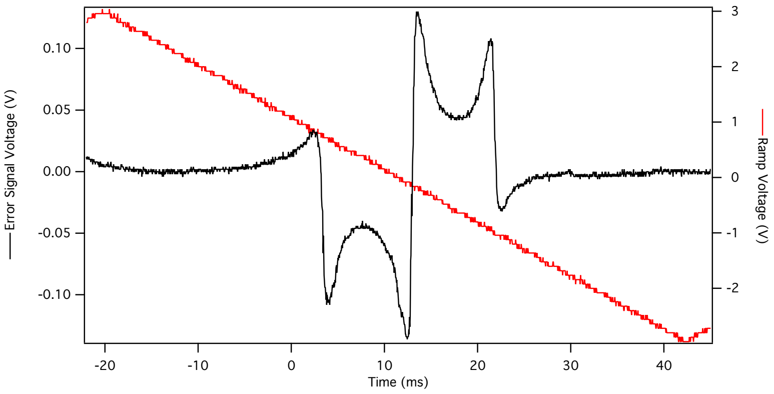

Figure 3.9: Example Pound-Drever-Hall error signal for the lattice sideband-to-transfer cavity lock. The error signal (black) and the ramp (red) are shown. The optical sweep rate for the lattice laser center frequency is 1.1 MHz/ms into a filter of bandwidth 100 kHz.

with frequency ranges centered around 6 GHz tend to be useful for, e.g., compensating for the frequency difference of a dressing laser and emitted photon in superradiance.

Generally, the microwave VCOs utilize frequency scalers and phase-frequency detectors (PFDs) combined with loop filters to lock to RF reference signals provided by DDS. VCOs with a variety of output frequency ranges, loop filters, PFDs, frequency scaling ratios, and mixing stages exist in the lab. Table 3.5 summarizes these parameters and labels the VCOs.

Table 3.5: Summary of the VCOs used in the lab, showing frequency range, prescale, and loop filter type.

Label	VCO Model	Freq. Range (GHz)	PFD	Prescale	Loop Filter
VCO C	HMC732	6 - 12 GHz @ -3 dBm	HMC440	128 = 16 (PFD) × 8 (prescaler)	Custom AD825
VCO D	RFVC1801	5 - 10 GHz @ -3 dBm	HMC440	16 (PFD) + mix freq. (6 GHz, nom.)	Custom AD825
Box VCO	HMC358	5.8 - 7 GHz @ 11 dBm	HMC699	64 (PFD)	Custom AD825

In order to stabilize the frequency and phase of the VCOs, feedback must be supplied to the oscillators. The output of the VCO is divided down either with a combination of a prescaler and the internal PFD prescaler, or just the internal PFD prescaler (depending on the PFD model). The resulting differential outputs drive the inputs to the loop filter, which for the “Custom AD825” is a single op-amp stage with an integrator. The loop filter drives the V_{tune} port on the VCO, which is a single-sided input generally 3 dB modulation bandwidth of at least 10 MHz (based on the . The result is a simple phase-locked loop (PLL) with 1 to 3 MHz of bandwidth, which provides good enough phase noise properties for most purposes.

Chapter 4

Superradiant Magnetometer

The magnetic field is a fundamental physical observable that is produced by essentially all electromagnetic phenomena. Magnetometers, devices that are capable of sensing the magnetic field, are therefore useful in a broad range of applications, including nuclear magnetic resonance (NMR) [54, 38], precision measurements of fundamental constants [58, 7], sensing biological processes [50], and atmospheric physics [108]. Generally, the two most important figures-of-merit for magnetometers are their sensing volume (i.e., characteristic size) and sensitivity. Sensing bandwidth is another important quality that distinguishes magnetic sensing technologies, since phenomena producing magnetic fields can occur at a wide range of frequencies.

Examples of magnetometer technologies are magneto-resistive materials [101], Hall probes [29], superconducting quantum interference devices (SQUIDs) [37], and nitrogen-vacancy centers in diamond [124]. SQUIDs have long been among the most sensitive magnetometers (~ 1 pT/$\sqrt{\text{Hz}}$), but they operate at cryogenic temperatures. Recent progress in nitrogen-vacancy centers–solid-state systems with atom-like electronic structures–has shown the capability to sense single spins [122] and sensitivities of $2 - 20$nT/$\sqrt{\text{Hz}}$ [63, 119].

Atomic sensors are attractive due to their advantages: intrinsically high sensitivity to magnetic fields, well-determined absolute calibration and scale factors, no need for a cryogenic environment, and the capacity for optical probing enabling remote sensing [27, 28, 60]. Atomic magnetometers have been demonstrated in both cold atom systems [70, 100, 97] and thermal vapor cells [69, 114, 82, 111, 60, 131, 62]. Atomic sensors hold the record for magnetic field sensitivity of 0.54 $\mathrm{fT}/\sqrt{\mathrm{Hz}}$ in a sensing volume of 0.3 cm^3 [69]. The capability of quantum entanglement to improve magnetometers is promising–a squeezing-enhanced atomic magnetometer has been demonstrated in Bose-Einstein condensate (BEC) systems [97, 100].

Generally, atomic magnetometers operate by preparing through optical pumping a spin imbalance that leads to single-atom magnetic dipoles. The effect of a magnetic field on the atomic dipoles is to cause Larmor precession of the spin, which in turn changes the complex polarizability (or, absorption and phase-shifting properties) of the atoms in response to an applied light field [27]. Detecting the phase shift of a laser passing through an optically pumped atomic vapor, then, indicates the strength of a magnetic field.

This chapter describes an atomic magnetometer based on a Raman superradiant system. The magnetometer operates by detecting the varying frequency shift between hyperfine ground states of ^{87}Rb atoms in a high-finesse optical cavity. While the effect of a magnetic field still occurs on a single-atom level, the readout of this sensor relies on the mapping of a *collective* atomic phase onto the light emitted from the sensor. The ultimate sensitivity is then set by the amount of atomic phase diffusion noise that results from the lasing process and noise associated with detecting the phase of the emitted light.

4.1 Experimental Details

To create the atomic gain medium needed for superradiant lasing, we begin by cooling the atoms. We create a magneto-optical trap (MOT) through a combination of a spherical quadrupole magnetic field and a MOT DBR laser red-detuned ≈ 15 MHz from the $\left|5^2S_{1/2}, F=2\right\rangle$ to $\left|5^2P_{3/2}, F=3\right\rangle$ optical cycling transition with a Repumper DBR laser detuned slightly red from the $\left|5^2S_{1/2}, F=1\right\rangle$ to $\left|5^2P_{3/2}, F=2\right\rangle$ transition. The MOT coils are then turned off while optical molasses beams are left on to load into the 1D optical lattice at 823 nm. A second polarization gradient cooling (PGC) stage then cools the atoms trapped in the lattice to ≈ 40 μK in a trap depth of ≈ 400 μK. The end result is a cold atom cloud with root-mean-square (rms) extent of ≈ 1.5 mm along the cavity axis and ≈ 15 μK in the transverse direction. The total effective sensing volume is then 2.1×10^{-3} mm^3.

Prior experiments that first demonstrated steady state superradiance in a Raman system operated on the $\left|5S_{1/2}F = 2, m_F = 0\right\rangle$ to $\left|5S_{1/2}F = 1, m_F = 0\right\rangle$ clock transition in ^{87}Rb, which only has second-order sensitivity to magnetic fields [23]. To realize the magnetometer, we used the maximally magnetic-field-sensitive hyperfine ground states of ^{87}Rb, $|\uparrow\rangle \equiv \left|5S_{1/2}F = 2, m_F = 2\right\rangle$ and $|\downarrow\rangle \equiv \left|5S_{1/2}F = 1, m_F = 1\right\rangle$. These states have the added benefit of straightforward state preparation through optical pumping with σ^+ polarizations, as well as a high absolute sensitivity to magnetic fields. This level scheme is shown in Figure 4.1(b).

To induce an effective optical decay from $|\uparrow\rangle$ to $|\downarrow\rangle$ at a controllable single-particle rate γ, we apply a π-polarized Raman dressing laser beam that is injected along the cavity axis and non-resonant with the optical cavity and detuned $\Delta/2\pi = 1.1$ GHz from the $|\uparrow\rangle$ to optically excited state $|i\rangle \equiv \left|5^2P_{1/2}, F' = 2, m_F' = 2\right\rangle$ transition at 795 nm. The cooperativity parameter of cavity QED, or Purcell factor [123], is $C = 7.7 \times 10^{-3}$ for the $|\uparrow\rangle$ to $|\downarrow\rangle$ Raman transition.

A set of Helmholtz coils apply a DC bias magnetic field $B_0 = 2.4 \times 10^{-4}$ T in the $\hat{x}$-direction perpendicular to the cavity axis ($\hat{z}$-direction). This establishes the quantization axis and shifts the transition frequency by $\omega_{\mathrm{dc}}/2\pi = 5.1$ MHz relative to the zero-field ground state hyperfine splitting. The DC field also breaks the degeneracy of the m_F levels so that microwave rotations can be performed exclusively on the $|\uparrow\rangle$ and $|\downarrow\rangle$ states with characteristic Rabi frequency $\Omega/2\pi \approx 35$ kHz for the spin echo studies. This field also sets the $\hat{x}$-direction as the direction in which the fields can be sensed, since small perpendicular components in the $\hat{y}$- or $\hat{z}$-directions would only change the splitting between states at second order. In this sense, the superradiant magnetometer is a vector magnetometer rather than a scalar magnetometer. The experimental configuration of the magnetic fields and light is shown in Figure 4.1(a).

The dressing, probe, and heterodyne local oscillator (LO) laser beams are all split off from a single master ECDL "Probe" laser at 795 nm. This allows for common-mode cancellation of most of the laser frequency noise of the 60 kHz FWHM laser. The heterodyne beam is 84 MHz blue of the dressing beam, and microwaves at 6.800 GHz (from a lab-developed low-noise source [35]) are

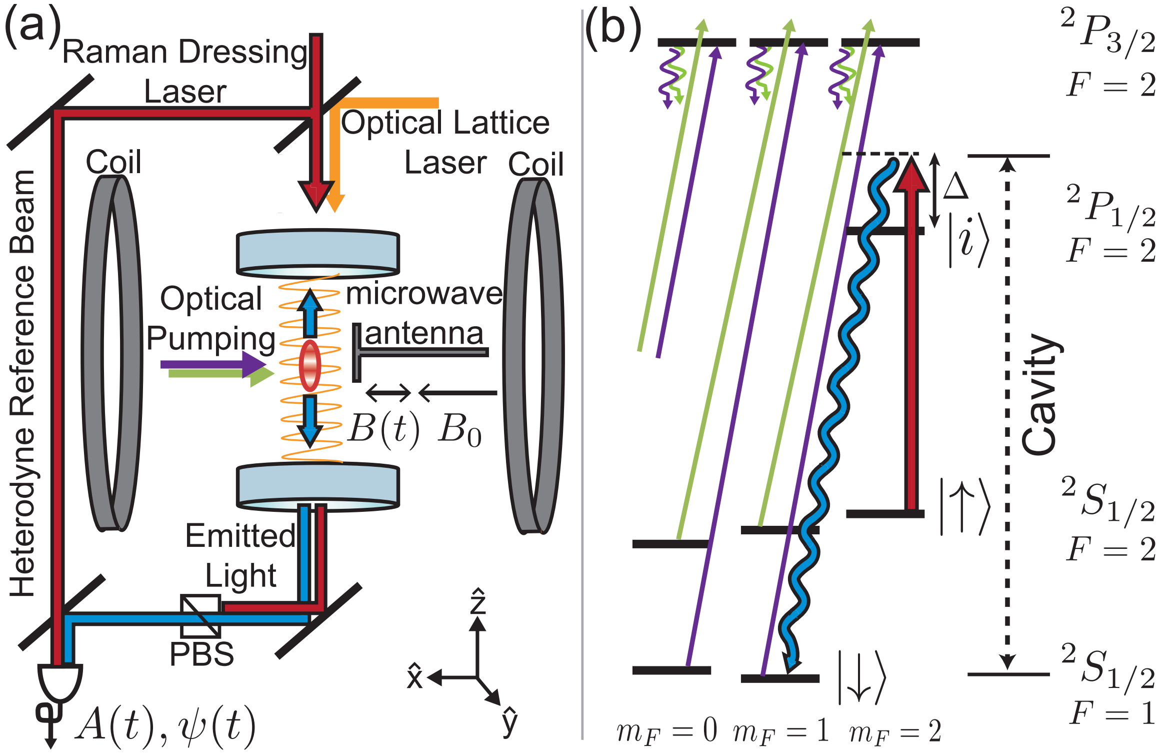

Figure 4.1: Experimental and level diagrams of magnetometer configuration. (a) The dressing laser is applied along the cavity axis and detected in heterodyne with the emitted light, with optical pumping beams applied from the side. Helmholtz coils provide a DC bias magnetic field and applied modulations in the $\hat{x}$-direction. A microwave antenna placed close to the atoms allows rotations between ground states. (b) Atomic levels used for superradiance. A dressing beam (red) induces decay from $|\uparrow\rangle$ to $|\downarrow\rangle$. A TEM$_{00}$ mode of the cavity is tuned to resonance with detuning $\Delta = 1.2$ GHz from an excited intermediate optical state $|i\rangle$. Optical pumping beams at 780 nm prepare the ensemble and maintain inversion.

applied to a fiber-copuled EOM to make up the frequency difference between the applied dressing beam and the emitted photon, which puts the relative LO-dressing frequency 50 MHz blue of the hyperfine frequency difference $\Delta_{hf} = 6.834$ GHz. A probe beam is generated from the master laser, with a 100 MHz red AOM and a second fiber-coupled EOM driven by a signal created by a high-frequency function generator (Stanford Research Systems SG384) mixed with an AD9959 DDS channel. This allows the frequency of the blue probe sideband to be swept across the cavity resonance to measure dispersive cavity shifts for counting the number of atoms in $|\uparrow\rangle$. A summary diagram is given in Figure 4.2.

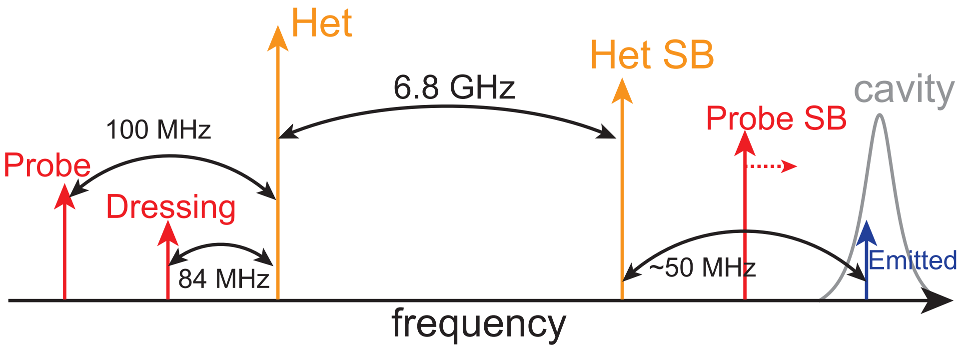

Figure 4.2: Schematic of the laser frequencies for dressing, probing cavity resonance, and detecting the emitted light. AOMs provide frequency shifts for dressing and probe lasers. EOMs put sidebands near the hyperfine frequency for detecting emitted light and probing the cavity.

Heterodyne detection allows reconstruction of the full light phasor $\mathcal{E}(t) = A(t)e^{i\psi(t)}$. Once the heterodyne RF beatnote signal is generated on the photodiode, we filter to select the frequency component of interest and quadrature demodulate using IQ demodulators . Corrections for small offsets and nonlinearities in the detection electronics are applied to the resulting phasor quadratures $I(t)$ and $Q(t)$ in software. The amplitude $A(t)$ and phase $\psi(t)$ are then computed from $I(t) + iQ(t) = A(t)e^{i\psi(t)}$.

A typical experimental sequence involves loading from a MOT into the lattice, optical pumping to initialize the system, then turning on both dressing and repumping lasers. Since the dressing laser is applied along the cavity axis, the direction in which the atoms are trapped in the Lamb-Dicke regime [136], the Doppler decoherence rate can be made very small. The emission rate can then be low enough that light-assisted collisions from repumping beams that cause loss from the trap occur at a rate low enough to allow the superradiant emission to persist for 20 to 100 ms [23]. During the time when superradiance is on, the magnetic field might be modulated or the dressing beam turned on and off to toggle the superradiant emission.

4.1.1 Wideband Sensing

When operating continuously, the sensor can provide a continuous time record of frequency– and therefore, B-field–fluctuations. We investigate the system's response to small magnetic fields by applying small modulations $B(t)$ to the current through the $\hat{x}$-oriented coils (that also provide B_0) and have control over the phase, frequency, and amplitude of the modulation. Upon application of an oscillating magnetic field, the energy $E(t)$ of the transition may be written as

$$E(t)/\hbar = \frac{d\phi(t)}{dt} = \Delta_{hf} + 2\pi\alpha\left(B_0 + B(t)\right), \tag{4.1}$$

where $\hbar$ is the reduced Planck constant and the sensitivity factor $\alpha = 2.1 \times 10^{10}$ Hz/T or $\alpha =$ 2.1 MHz/G between $|F = 1, m_F = 1\rangle$ and $|F = 2, m_F = 2\rangle$. It is worth noting that the sensitivity of this magnetometer is absolute and not set by fractional sensitivity to the change in the ground-state frequency Δ_{hf}—that is, an atomic magnetometer of this kind with a higher-Q atom (such as strontium) utilizing an optical transition would not gain sensitivity in terms of the raw Hz/G conversion factor α. In the low-field limit, the energy shift for Rb due to the Zeeman effect for a state with F, m_F is given by [40]

$$\Delta E(t)/\hbar = \alpha B_{\text{tot}} = \mu_B g_F m_F (B_0 + B(t)), \tag{4.2}$$

where the Bohr magneton $\mu_B = 9.274 \times 10^{-24}$ J/T, $g_F \approx \pm 2$, and $m_F = 1$ or 2 for the ground states used here. Consequently, the fundamental sensitivity is set by the Bohr magneton μ_B and numerical factors of order unity.

It is convenient to ignore the DC frequency shift to the transition frequency Δ_{21} from the hyperfine splitting and the static magnetic field B_0, so the following analysis is in the rotating frame at frequency $\Delta_{hf} + 2\pi\alpha B_0$. With the superradiance on, we apply a small sinusoidal modulation of the field $B(t) = B_m \cos(2\pi f_m t + \theta_m)$ to create a modulation of the atomic phase as $\phi(t) = \beta \sin(2\pi f_m t + \theta_m)$, where the modulation index is $\beta = \alpha B_m / f_m$. This relationship comes from simply integrating the frequency shift over time to back out the total phase shift.

The data were obtained by detecting $\mathcal{E}(t)$ and converting to $I(t), Q(t)$ during a time window of 3 ms. The atoms are reloaded and the experiment is repeated at a 1 Hz rate. Atom loss causes chirping of the carrier frequency from the combined effect of cavity frequency pulling (suppressed as γ/κ) and an atom-dependent shift of the dressed cavity mode frequency into which the atoms emit their light. This kind of cavity-related chirping effect appears as a quadratic ramp of $\psi(t)$ in time, and can fluctuate in magnitude from shot to shot. On a single-shot basis, we mitigate the effect of the cavity chirping by applying a third-order digital Bessel high-pass filter to $\psi(t)$ with cutoff frequency of 300 Hz to produce a filtered phase $\psi'(t)$. Spectral leakage of the carrier due to a rectangular sampling time window is mitigated by applying a Blackman-Harris time window weight factor $w(t) = 0.423 - 0.498 \cos(t/T_m) + 0.0792 \cos(2t/T_m)$, where T_m is the total measurement time, such that $\mathcal{E}''(t) = w(t)\mathcal{E}'(t)$.

We remove any possible amplitude modulation (AM) sideband noise by setting the amplitude of $\mathcal{E}(t)$ to $A(t) = 1$ in the data analysis. Because the intensity of the output light depends crucially on the level of inversion and the Bloch vector polar angle θ, such AM could arise from, e.g., the applied frequency modulation changing the effective cooperativity C' for the atomic emission mode and therefore modifying the collective emission rate $NC'\gamma$. This stripping off of amplitude noise is justified, since the same effect could be accomplished in real time by phase locking a low amplitude noise oscillator to the emitted light phase.

Figure 4.3(a) demonstrates the simultaneous detection during continuous superradiance of two applied discrete modulations at frequencies 6.9 and 10.2 kHz. These frequencies were chosen so that, if there were harmonics at, e.g., 2×6.9 kHz, they wouldn't interfere with the 10.2 kHz tone. We do not observe any modulation at the difference or sum frequency of the two modulation frequencies, confirming the linearity of the detection scheme to our achievable level of sensitivity. Near DC, residual bleed-through of the carrier limits the sensitivity, causing the steep rise around 1 kHz.

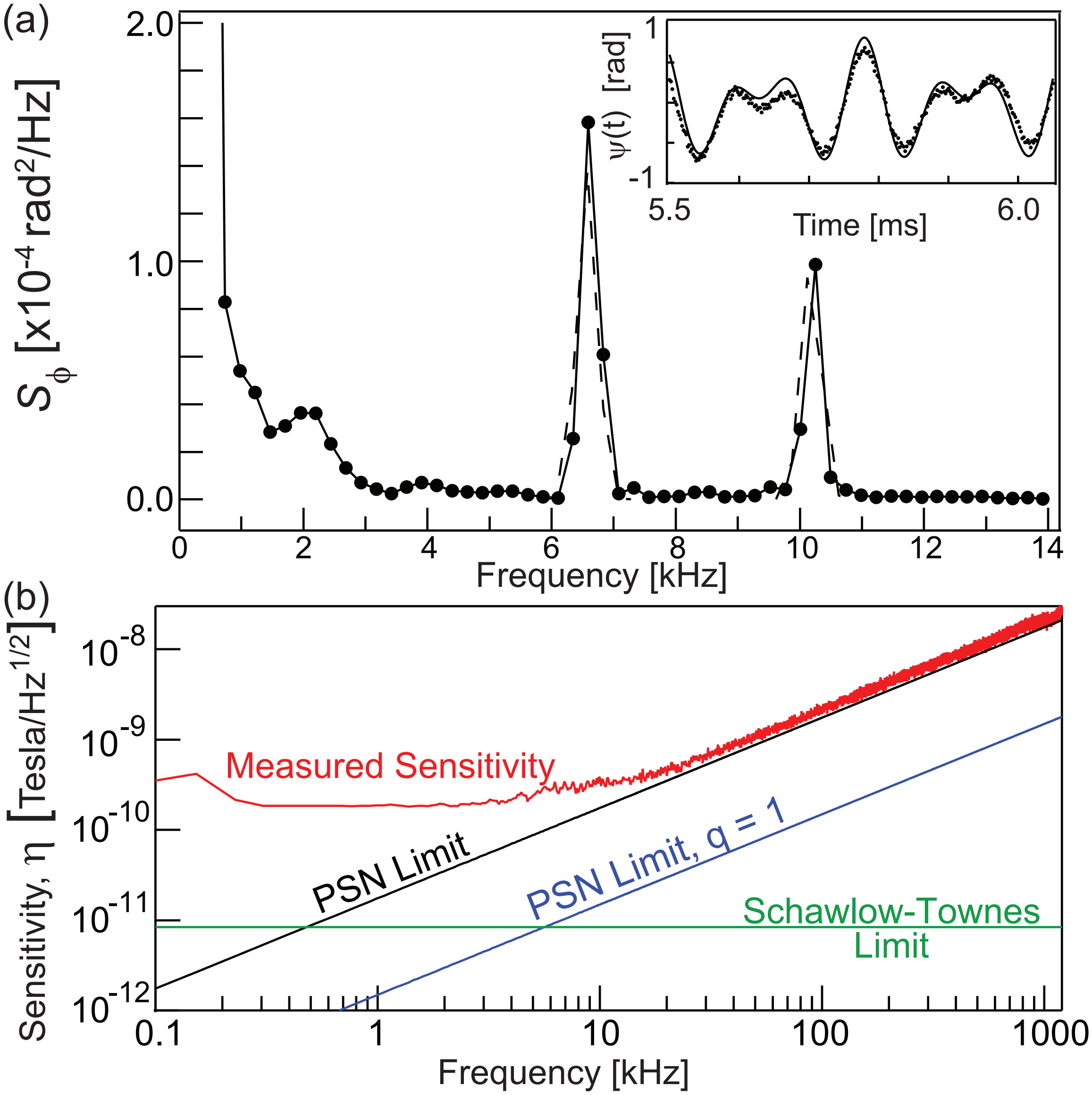

Figure 4.3: (a) Power spectral density of instantaneous phase fluctuations, S_ϕ, showing two discrete modulation peaks. (inset) Portion of the time trace of the light phasor $\psi(t)$ used to generate the power spectral density. (b) Sensitivity $\eta(f)$ in $\mathrm{T}/\sqrt{\mathrm{Hz}}$ without any applied modulation. The predicted limit from Schawlow-Townes quantum phase diffusion (green) and the predicted photon shot noise limit for $N = 1.1 \times 10^6$, and $W = 4.5 \times 10^4\ \mathrm{s}^{-1}$ and finite quantum efficiency $q = 7 \times 10^{-2}$ (black) and for ideal quantum efficiency $q = 1$ (blue) are shown.

4.2 Sensitivity in Continuous Operation

A convenient measure of the performance of the magnetometer is the frequency-dependent sensitivity, $\eta(f)$ (units of Tesla/$\sqrt{\text{Hz}}$). The sensitivity describes, in a 1 Hz bandwidth, the rms strength of the field that would be equal to the noise floor of the detector. A power spectrum of the instantaneous phase fluctuations of the superradiant laser, with the applied $B(t) = 0$, is used to generate the power spectral density of phase fluctuations $S_\phi(f)$ and in turn, the sensitivity η. This section describes how we calculate the sensitivity η.

We define the frequency-dependent sensitivity $\eta(f)$ (in spectral density units T/$\sqrt{\text{Hz}}$) to be related to the total variance in B-field by the sum

$$\begin{aligned} (\Delta B)^2 &= \int_0^\infty \eta^2(f)df && (4.3)\\ = \frac{(\Delta\nu)^2}{\alpha^2} &= \frac{1}{\alpha^2}\int_0^\infty S_\nu(f)df && (4.4)\\ &= \frac{1}{\alpha^2}\int_0^\infty f^2 S_\phi(f)df. && (4.5)\end{aligned}$$

For a single-tone noise source, we substitute the general expression for $S_\phi(f)$ to obtain

$$\begin{aligned} (\Delta B)^2 &= \frac{1}{\alpha^2}\int_0^\infty f^2\frac{\langle\beta^2\rangle}{2}\delta(f-f_m)df && (4.6)\\ &= \frac{f_m^2}{\alpha^2}\frac{\langle\beta^2\rangle}{2} && (4.7)\\ \Rightarrow \eta(f_m) &= \frac{f}{\alpha}\sqrt{S_\phi(f_m)} && (4.8)\end{aligned}$$

Equation 4.8 is the key relationship for obtaining the sensitivity from the measured power spectrum. The double-sideband power spectral density (PSD) of phase fluctuations $S_\phi(f)$ is calculated from the Fourier transform of $\mathcal{E}''(t)$ and averaged over many trials [106].

Figure 4.3(b) shows the calculated ideal detection sensitivity and the measured field sensitivity for $\gamma = 37$ s^{-1}, quantum efficiency $q = 7.2\times10^{-3}$, $N = 1.1\times10^6$, and $W = 4.5\times10^4$ s^{-1}. Since $NC\gamma/2 = 1.6\times10^5$, this represents operation somewhat below the optimum repumping rate. Our apparatus does not have any magnetic shielding, so that ambient magnetic field noise, noise in the coil driver electronics, and remaining emission frequency chirping contribute noise far above the fundamental Schawlow-Townes diffusion limit at frequencies < 11 kHz. At high frequencies, we see good agreement between the expected PSN limit and our measured η. The ultimate limit is ~ 140 pT/$\sqrt{\text{Hz}}$ at an offset of 1 kHz.

Ideally, the noise floor in the light emitted by the superradiant laser comes from two sources: (1) Diffusion of the atomic Bloch vector coming from quantum mechanical randomness that enters through spontaneous emission into the cavity and is mapped onto the output light, and (2) the photon statistics of the emitted light (photon shot noise). The Schawlow-Townes term (1) dominates at low offset frequencies from the carrier. In S_ϕ, it looks like a $1/f$ rise near DC. However, at higher frequencies the flat noise floor in S_ϕ contributed by photon shot noise dominates. When converting to S_ν and then η, the Schawlow-Townes becomes a flat noise floor in sensitivity and the PSN limit grows with frequency. The frequency dependence of the PSN noise floor, Schawlow-Townes phase diffusion noise floor, and their sum are represented in Figure 4.4(a) and (b) for S_ϕ and S_ν, respectively.

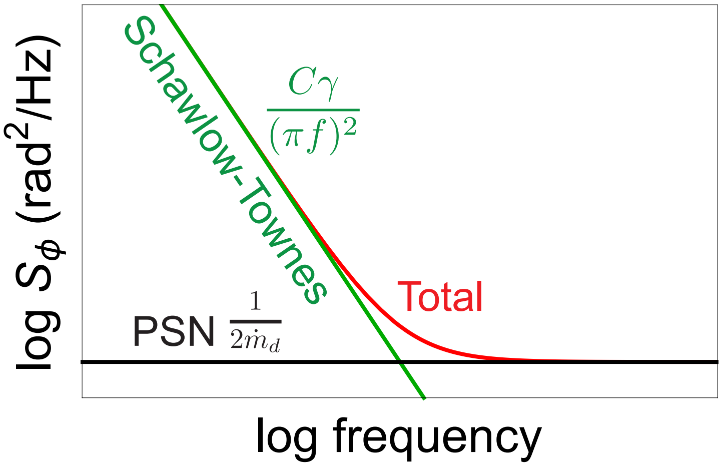

Figure 4.4: Sketch of the ideal contributions to the spectral densities S_ϕ versus frequency. Log-log plot of S_ϕ in units of rad^2/$\sqrt{\text{Hz}}$ versus frequency. The black line is the photon shot noise limit with scaling $1/(2\dot{m}_d$, green is the ideal phase diffusion limit, scaling as γ/f^2, and red is the sum. The corner frequency where the PSN and S-T contributions cross is $f_0 = \sqrt{qRNC\gamma}/(2\pi)$.

Summarizing from above, in the absence of technical noise, the ideal phase noise density

$$S_\phi^i(f) = S_\phi^{\mathrm{ST}} + S_\phi^{\mathrm{PSN}} = \frac{S_\nu^{\mathrm{ST}}}{f^2} + \frac{1}{2\dot{m}_d} \tag{4.9}$$

$$= \frac{C\gamma}{(\pi f)^2} + \frac{1}{2\dot{m}_d} \tag{4.10}$$

represents the Schawlow-Townes limit (first term) and the PSN limit (second term). Here, I have used the diffusion coefficient $D^2 = 2C\gamma$ for a FWHM linewidth of $C\gamma/\pi$ [20]. To find $\dot{m}_d$, we use the expression for the output power from the superradiant laser $P = \frac{W}{2C\gamma}(NC\gamma - W)$. For photon quantum detection efficiency q and optimum repumping rate $W_{\mathrm{pk}} = NC\gamma/2$, the rate of detected photons emitted from the laser is then $\dot{m}_d = qRN^2C\gamma/8$. Here, R is a reduction factor for our multi-level ^{87}Rb scheme with value $R \leq 3/5$, coming from time delays in the repumping process [19, 22]. The ideal field sensitivity is then expressed as

$$\left(\eta^i(f)\right)^2 = \frac{f^2}{\alpha^2} 2S_\phi = \frac{2f^2}{\alpha^2}\left(\frac{C\gamma}{\pi^2 f^2} + \frac{4}{qRN^2C\gamma}\right) \tag{4.11}$$

$$= \frac{2C\gamma}{\pi^2\alpha^2}\left(1 + \frac{f^2}{qR(NC\gamma/(2\pi))^2}\right) = \frac{2C\gamma}{\pi^2\alpha^2}\left(1 + \frac{f^2}{f_0^2}\right), \tag{4.12}$$

where the corner frequency $f_0 = \sqrt{qR}NC\gamma/(2\pi)$. We see that the equivalent field noise density scales with the single-particle decay rate into the cavity $C\gamma$, while the corner frequency scales with the collectively enhanced scattering rate $NC\gamma$. In principle, the tunable decay rate γ can be reduced until the single-particle transition broadening described by a transverse coherence decay rate $\gamma_\perp$ is no longer negligible compared to $W/2$, setting a minimum $C\gamma \sim \gamma_\perp/N$ for which $\left(\eta^i(f)\right)^2 \sim (\gamma_\perp/N)(1 + f^2/f_0^2)$ with corner frequency $f_0 \sim \gamma_\perp$. These ideal scalings are equivalent to the scaling of the standard quantum limit for unentangled atoms in the presence of transition broadening.

4.3 Narrowband Detection

The sensitivity of the continuous readout can be surpassed if the system operates in a narrowband detection mode based on passive evolution, analogous to Ramsey spectroscopy. As first demonstrated by Bohnet *et al.* [20], an equivalent passive Ramsey measurement technique can be realized using steady state superradiance. The superradiant emission is interrupted for some period of dark time T_d by setting the decay rate γ and repumping rate W to zero before turning both back on. The atomic phase precesses during this dark period with no Schawlow-Townes phase diffusion and possibly lower systematic errors before γ and W are restored to their previous non-zero values. Measurement of the light phase just before and after the shut-off allows the accumulated quantum phase to be estimated as $\phi(T_d) - \phi(0) \approx \psi(T_d) - \psi(0) \equiv \Delta\psi$ The measurement record needed to estimate the final phase $\psi(T_d)$ also serves to estimate the phase for the next iteration of the experiment, potentially allowing high repetition rate, non-destructive Ramsey-like measurements.

Ramsey spectroscopy operates with a detection band centered at zero frequency. The favorable sensitivity of DC detection can be translated to an in-principle arbitrary frequency using spin echo sequences to essentially serve the role of a mixer in a lock-in amplifier [70]. This Carr-Purcell-Meiboom-Gill sequence [92] is an essential concept in solid-state magnetometry, such as in NV centers, and NMR, where a very high degree of transition broadening necessitates the use of spin echo to extend the coherence time [124]. If the π pulses are aligned to the applied modulation such that the π pulse is centered in time on the zero crossing of the sinusoidal *phase* modulation, the net accumulated phase will not be zero–instead, after each π-pulse, the phase difference $\Delta\phi_B$ between applying the B-field and absence of the B-field always increases. This idea for a single cycle of the B-field and two π-pulses is illustrated in Fig. 4.5.

To maintain steady state superradiance, we need to maintain the atomic inversion to keep the laser above threshold. This means that, since the collective Bloch vector is in the upper hemisphere of the Bloch sphere with positive J_z, only an even number n_π of π pulses during the dark evolution time will re-establish inversion so that superradiance can begin once the pumps and dressing beams are turned on again.

Figure 4.6 shows a sequence in which the phase accumulation is coherently enhanced through a spin echo pulse sequence with the π-pulses aligned in time to the nodes of the applied modulation $B(t)$. The phase difference $\Delta\psi$ is approximately $2\beta n_\pi$, where $\beta = 0.71$ rad and $n_\pi = 2$, with only small corrections due to the finite π-pulse times of 15 μs.

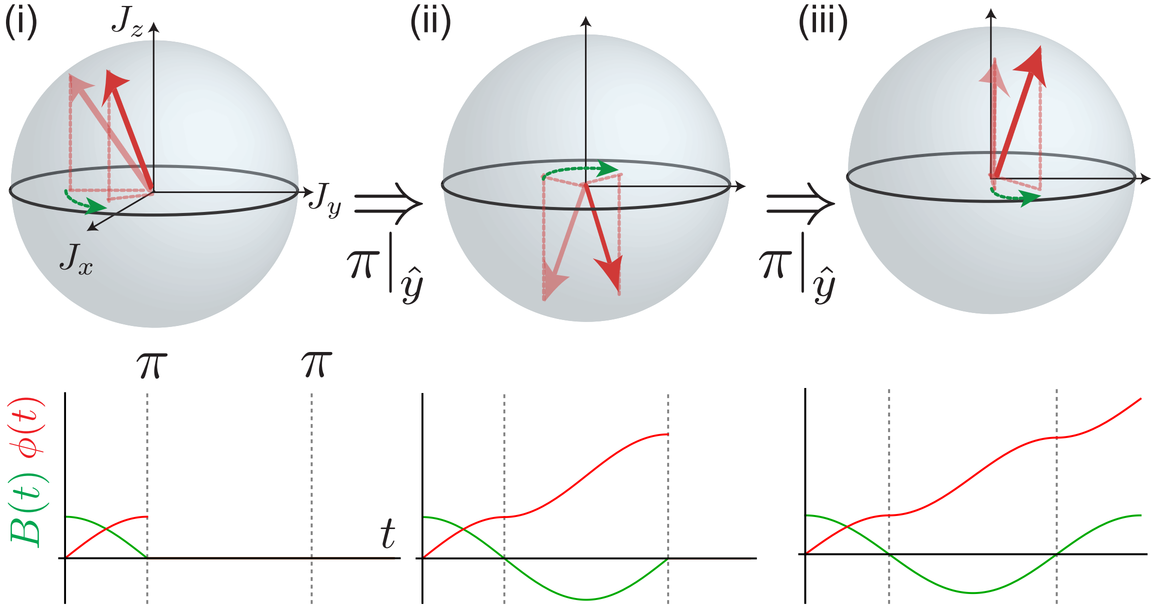

Figure 4.5: Cartoon picture of Bloch vector of superradiant ensemble accumulating phase in the presence of B-field modulation as a function of time. (above) Red arrows show the Bloch vector at the end of each time step, with ghosted red arrows showing the orientation of the Bloch vector at the beginning of the time step. Green arrows show phase accumulation due to B-field in each time step. (below) Plot of the applied modulation $B(t)$ (green) and the accumulated relative phase (red) vs. time. (i) Atoms begin accumulating phase and a π-pulse is applied before the phase accumulation reverses. (ii) After the π-pulse, atoms continue evolving phase, in the opposite direction (clockwise from above) from the first evolution period. Since the coherence is flipped by the π-pulse, the total phase deviation will add in the end. (iii) After the final π-pulse, the phase evolution continues while the sample has once again achieved inversion. Even though $B(t)$ goes positive and negative, there is a net atomic phase shift.

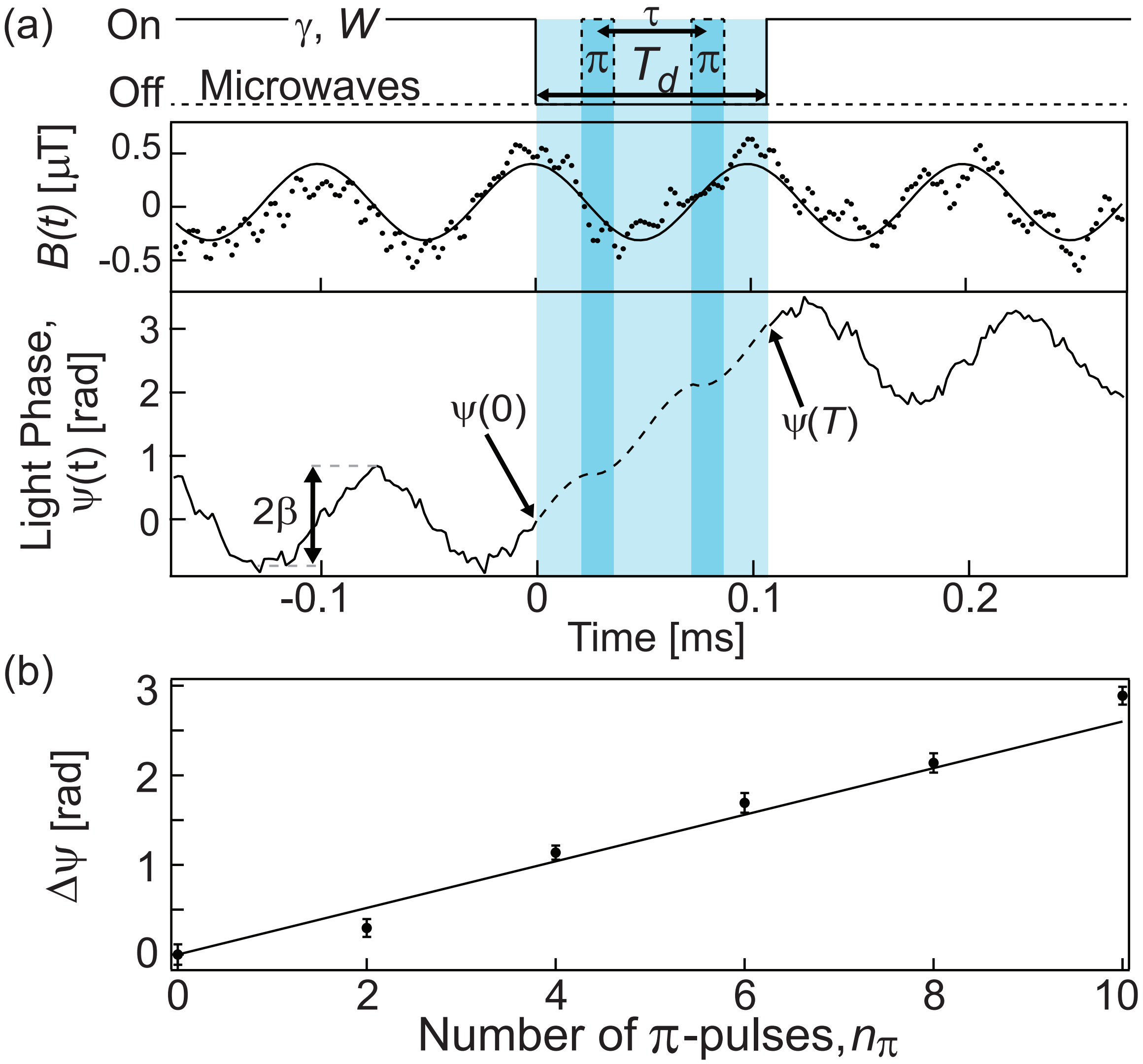

Figure 4.6: Experimental sequence showing narrowband sensitivity of magnetometer. (a) (Top) Timing diagram for the Ramsey sequence, showing on and off states for lasers (solid) and microwaves (dashed), (middle) time traces of the measured (points) and fitted (solid line) $B(t)$, and (bottom) the measured (solid line) light phase $\psi(t)$ and expected atomic phase $\phi(t)$ (dashed black line) in the presence of magnetic field modulation. During the dark period in which all optical pumping and dressing lasers are shut off (light blue region), spin echo π-pulses cause the unobserved atomic phase $\phi(t)$ to coherently increase in response to the applied magnetic field modulation. This manifests as a discontinuous advance in the phase of the light when the optical pumping and dressing lasers are turned back on. (c) The magnitude of the phase advance $\Delta\psi = \psi(T_d) - \psi(0)$ (points) increases witht he number of π-pulses n_π. The total dark time is $T_d = n_\pi \tau$. Also shown is the expected slope of 2β (line).

4.4 Sensitivity in Narrowband Configuration

In this section, I derive an expression for the fundamental sensitivity of the magnetometer. For a single dark time, the total phase advance (or signal size) for the aligned phase modulation that constructively adds is

$$\begin{aligned} \Delta\psi = 2\beta n_\pi &= 4\beta n_c & (4.13) \\ = 4\left(\frac{\alpha B_0}{f_m}\right) T_d f_m &= 4\alpha B_0 T_d, & (4.14) \end{aligned}$$

where $n_c = 2n_\pi$ because there needs to be an even number of π-pulses per complete cycle to maintain inversion. The sensitivity is set by the fractional noise in the B-field measurement $\Delta B/B_0 = \sigma_\psi/\Delta\psi$. Rearranging gives $\Delta B = \sigma_\psi/(4\alpha T_d)$. In principle, the experiment can be repeated to average down the noise (as in standard Ramsey spectroscopy) so that the number of measurements in a fixed time T_{meas} is $n_{\text{meas}} = T_{\text{meas}}/T_d$, giving $1/\sqrt{n_{\text{meas}}} = \sqrt{T_d/T_{\text{meas}}}$. Then, assuming that the noise between trials is uncorrelated, the noise for n_{meas} trials will be $\Delta B_{n_{\text{meas}}} = \sigma_\psi/(4\alpha\sqrt{T_d T_{\text{meas}}})$. To get the equivalent sensitivity in Tesla/$\sqrt{\text{Hz}}$, we can set $T_{\text{meas}} = 1$ sec, so that

$$\eta = \frac{\sigma_\psi}{4\alpha\sqrt{T_d}}, \tag{4.15}$$

where σ_ψ is the rms measurement noise of the light phase difference $\Delta\psi$. Figure 4.6 shows the phase advance $\Delta\psi$ versus the number of π-pulses applied with a 10 kHz modulation with $\beta = 0.13$ rad and modulation phase for which nodes of $B(t)$ are aligned to the pulse times. The fitted slope is 0.28 rad/π-pulse, close to the expected slope of magnitude $2\beta = 0.26$ rad/pulse, showing that we have a good understanding of the phase shift imposed by the B-field and spin echo sequence.

Figure 4.7 illustrates both that the sensitivity can be translated in frequency, and that the sensitivity increases with the number of π-pulses, while the bandwidth is decreased. We construct the phase-insensitive transfer function

$$G(f_m) \equiv \beta^{-1}\sqrt{\left\langle(\Delta\psi)^2\right\rangle_{\theta_m}}, \tag{4.16}$$

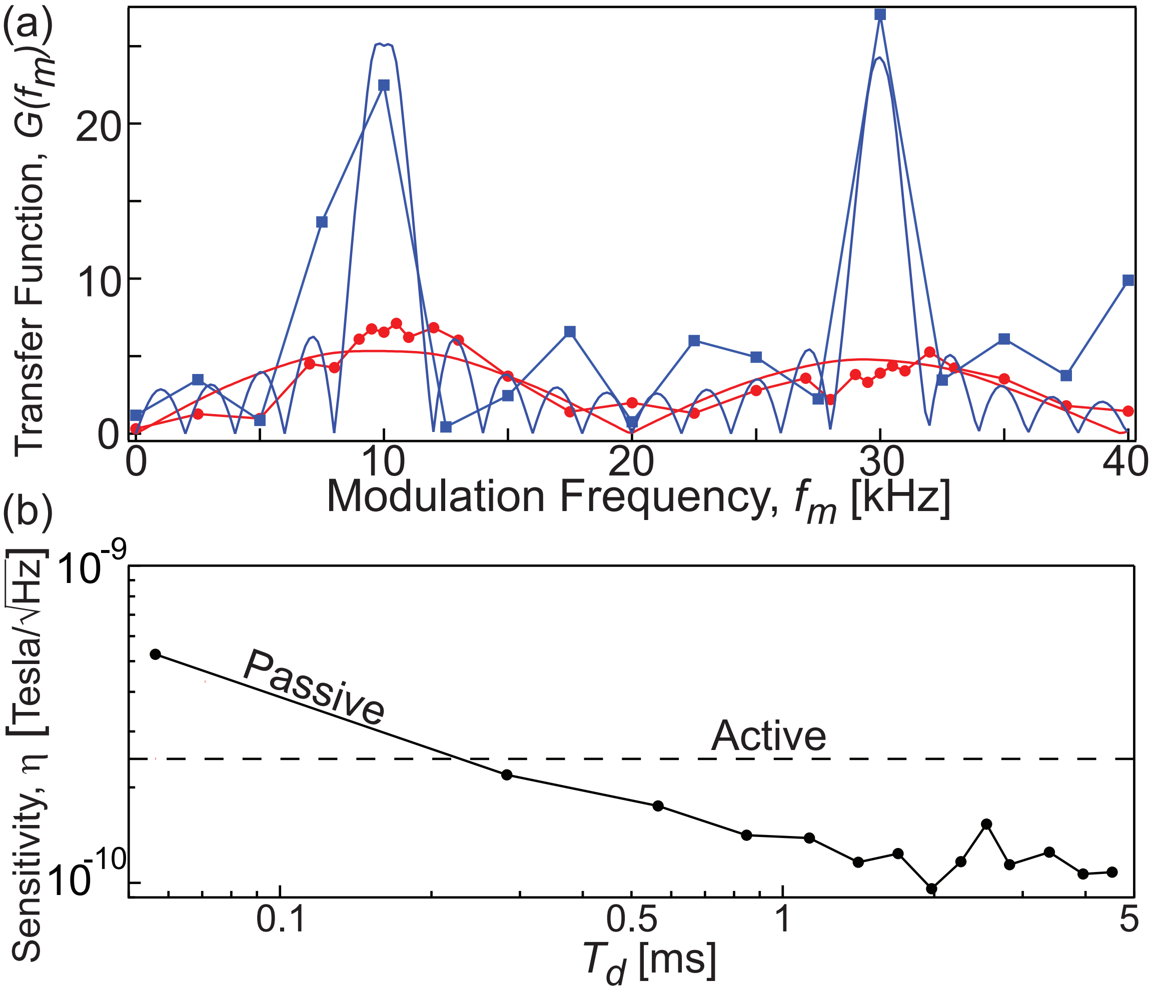

Figure 4.7: Narrowband sensitivity of magnetometer. (a) Quadrature-averaged transfer function $G(f_m)$ versus modulation frequency f_m. Transfer functions (solid lines) are shown for $n_\pi = 2$ (red) and $n_\pi = 8$ (blue). The peaks correspond to 1/(spacing) (b) Sensitivity η vs. dark time. Wideband sensitivity at $f_m = 36$ kHz is the dashed horizontal line.

by measuring $\Delta\psi$ and averaging over the modulation phase θ_m at each modulation frequency f_m. For this data, the spacing between the π-pulses was fixed to $\tau = T_d/n_\pi = 50\ \mu$s, setting the maximum sensitivity to modulations near 10 kHz. Two different numbers of pulses are used: $n_\pi = 2$ and 10 for the red and blue curves, respectively.

4.5 Numerical Simulation of Phase Accumulation

For comparison, we numerically integrate the time-dependent Schrödinger equation for a two-level system in the presence of a modulated classical driving field with finite Rabi frequency $\Omega/2\pi =$ 33 kHz. This numerical simulation is necessary because the frequency scales of the modulation frequency and microwave Rabi frequency are the same order of magnitude (due to technical constraints on the B-field modulation frequency and the microwave power), so that in the frame of the atoms, the effective rotation axis $\vec{\Omega}$ has a modulating azimuthal phase ϕ_Ω.

Figure 4.7 shows that this technique allows sensitivity below the limit imposed by PSN in the active mode. We compare the field sensitivity at frequency $f = 36$ kHz using an increasing number of spin echo pulses to the PSN-limited active sensing mode at the same frequency. The phase measurement noise σ_ψ is roughly constant as T_d increases since the continuous spin echo sequence prevents a great deal of dephasing, allowing the collective dipole to persist even for long dark times. The win in sensitivity then comes from the $1/\sqrt{T_d}$ scaling with the dark time. Eventually, the sensitivity drops below that of the active mode and reaches 10 pT/$\sqrt{\text{Hz}}$.

4.6 Additional Details

4.6.1 Phase Noise Definitions

Here I describe in detail the phase noise conventions that are used to calculate the sensitivity of Section 4.2. I use the phase noise conventions of Ref. [34] for the following discussion. For a phase modulation of the form $\phi(t) = \phi_0 + \beta\cos(2\pi f_m t + \theta_m)$, where the modulation index $\beta = f_0/f_m$, we can define the single sideband (SSB) phase noise as

$$\mathcal{L}_\phi(f) = \frac{\langle \beta^2 \rangle}{4} \delta(f - f_m), \tag{4.17}$$

where $\delta(f)$ is the Dirac delta functional. To relate the RMS phase variance $(\Delta\phi)^2$ (in units of radian^2) to the SSB phase noise spectral density $\mathcal{L}_\phi(f)$ (units of rad^2/Hz), we use the convention

$$\begin{aligned}
(\Delta\phi)^2 &= \int_{-\infty}^{\infty} T(f)\mathcal{L}_\phi(f)df & (4.18)\\
&= 2\int_{0}^{\infty} T(f)\mathcal{L}_\phi(f)df & (4.19)\\
&= \int_{0}^{\infty} T(f)S_\phi(f)df. & (4.20)
\end{aligned}$$

From the definition above, we see that the PSD $S_\phi(f)$ and SSB spectral density $\mathcal{L}_\phi$ only differ by a factor of two: $S_\phi(f_m) = \frac{\langle \beta^2 \rangle}{2}\delta(f - f_m)$. The PSD $S_\phi(f)$ is also formally defined from a two-time correlation of phase as

$$S_\phi(f) = 2\int_{-\infty}^{\infty} \langle \phi(t)\phi(t+\tau) \rangle_t \, e^{-i2\pi f\tau} d\tau. \tag{4.21}$$

Since the instantaneous frequency is $f(t) = \frac{1}{2\pi}\frac{d\phi(t)}{dt}$, the PSD of frequency fluctuations is $S_\nu(f) = f^2 S_\phi(f)$.

4.6.2 Conversion from Measured Power Spectrum to Power Spectral Density

Since the FFT of the light phasor $\mathcal{E}(t) = A(t)e^{i\psi(t)}$ is taken with $A(t) = 1$, and the phase modulation $\phi(t) \ll 1$, we expand the corrected light phasor as $\mathcal{E}''(t) \simeq 1 + i\phi(t)$. We obtain a two-sided power spectrum $P(f_i) \propto \mathcal{L}(f_i)$ at discrete frequencies f_i separated by bandwidth Δf. To convert to the PSD of phase fluctuations,

$$S_\phi(f_i) = \frac{2P(f_i)}{\Delta f \left(\sum_j P(f_j)\right)}, \tag{4.22}$$

where the normalization factor accounts for the lack of power conservation of the Blackman-Harris window.

4.6.3 Atom Counting

Measuring the number of atoms participating in superradiance is important for initial tuning of the system, reproducibility in power output from day-to-day, and understanding the quality of our optical pumping sequence. To measure the number of participating atoms, we measured the cavity resonance frequency using a probe laser. In contrast to the spin squeezing measurements discussed later in Chapter 6, projection-noise-limited sensitivity is not required here. By sweeping the probe laser over the cavity resonance frequency, we were able to measure the frequency shift of the dressed cavity compared to the bare cavity. The RMS atom number N_{rms} was then determined from an exact diagonalization of the atom-cavity Hamiltonian including the basis states (written as $|\text{atom}; m_c\rangle$) $|1,1;1\rangle$, $|2',1;0\rangle$, and $|1',1;0\rangle$ written in the rotating frame of the frequency corresponding to the $|F=2\rangle$ to $|F=2'\rangle$ atomic transition energy, yielded an expression for the number of atoms in $|1,1\rangle$ as a function of the cavity frequency shift $\Delta\omega$.

The exact calculation actually agrees within 5% of a simple calculation that does not include any interference terms between excited states

$$\Delta\omega \approx N_{rms}^{approx} \frac{1}{4} \left(\frac{c_1 g_{rms}^2}{\delta_p} + \frac{c_2 g_{rms}^2}{\delta_p + 2\pi \times 814.5 \text{ MHz}} \right), \tag{4.23}$$

where $c_1 = 1/4$ and $c_2 = 3/4$ account for differences in Clebsch-Gordan coefficients between excited states.

4.7 Conclusion

In this chapter, I described a superradiant laser that acts as a vector magnetometer through detection of the emitted light. The fundamental sensitivity scalings for the active mode and passive mode were described. In the wideband mode, a sensitivity of 140 $\text{pT}/\sqrt{\text{Hz}}$ at offset frequencies of 1–2 kHz was observed. Narrowband operation was also demonstrated, with ideal sensitivity about a factor of 3 better at 36 kHz.

There are already plenty of sensitive magnetometers. Why is this one special? One unique quality is its ability to run both in steady state and in a pulsed mode with higher sensitivity.

In principle, wideband operation could give a lot of information about the B-field spectrum, and narrowband operation could zoom in on a particular frequency component with potentially lower noise. If the laser gain medium were long-lived (e.g., a solid state system) then optical addressability would be the major requirement for operating such a device.

Chapter 5

Phase Synchronization Between Superradiant Lasers

5.1 Introduction

Coupled oscillators appear in a very wide array of contexts. Under certain conditions, coupled oscillators can be seen to undergo a transition to synchronized behavior, where the oscillators' relative phase difference can be constant in time even when their uncoupled natural frequencies differ. Huygens first described the phase synchronization of coupled pendulum clocks in 1665 [11], and since then phase synchronization of oscillators has been descibed in physical, chemical, biological, and social systems [120]. The behavior of coupled oscillators continues to be a field of active study.

Recent experimental progress includes the development of nano-scale mechanical [115], optomechanical [144, 6], optical frequency comb[88], spintronic [64, 109], and electro-mechanical [88] systems. Synchronization in large arrays of nonlinear oscillators could provide suppression of phase noise for improving local frequency references [44].

Extensive theoretical studies of large ensembles of coupled oscillators exist in the literature, most notably the nonlinear Kuramoto model [121, 2, 137]. Until recently, theoretical explorations focused on classical oscillators that were not subject to quantum fluctuations. Examples in which few coupled oscillators could exhibit effects of quantum noise have been proposed in optomechanical [130, 86, 85, 142], optical [74], and cold atom [141, 73, 75] systems. In the context of continuous quantum phase transitions, synchronized quantum oscillators would represent a dynamical quantum phase transition [48, 126] in the two-time correlation function of the oscillator phases [141]. Relatedly, a quantum phase transition in an open system to a spontaneously ordered state has been demonstrated in a BEC coupled to light fields [10].

5.2 Two Superradiant Lasers

This section describes experiments in which two superradiant lasers are operated within the same longitudinal and transverse cavity mode, the experimental implementation of the system theoretically studied by Xu *et al.* [141]. As in Chapters 2 and 4, we create superradiant ensembles by applying dressing light to generate spontaneous two-photon Raman transitions between metastable ground hyperfine states. Both lasers operate in the bad cavity regime where the atomic broadening is much smaller than the cavity decay rate, $\gamma_\perp \ll \kappa$.

The two superradiant ensembles are spatially separate, with experimentally controllable natural frequencies. To distinguish between the two ensembles, I use a and b as labels. The lasing excited states $|\uparrow_a\rangle$ and $|\uparrow_b\rangle$ are separated by frequency $\delta \leq \pm 2$ MHz $< \kappa/2$. The average of the two natural frequencies is at detuning $\delta_c \in (-\kappa, 0)$ from the cavity line center. Both lasing transitions are within κ of the cavity resonance frequency, ω_c. The unperturbed emission frequencies are ω_a^0 and ω_b^0, and the emission frequencies in the presence of interactions ω_a and ω_b.

Two experimental schemes are presented in this chapter: the first in which the frequency degeneracy is broken by changing the frequency degeneracy of the lasing states by changing a magnetic field (I), and a second in which the phase difference between the two lasers is set by the relative phase of Raman dressing lasers (II). This latter scheme has the advantage of greater phase agility, at the cost of having to increase the decay rate and repumping rates so the atomic sample is destroyed more quickly.

Figure 5.2 shows the dressing laser and repumper polarizations, as well as atomic energy level diagrams, for the two schemes. In the magnetic field scheme (I), separate repumping beams applied with σ^+ and σ^- polarizations split the atoms into ensembles a and b with ground states $|\downarrow_a\rangle = \left|5^2S_{1/2}, F=2, m_F=2\right\rangle$ and $|\downarrow_b\rangle = \left|5^2S_{1/2}, F=2, m_F=-2\right\rangle$. The 795 nm dressing laser is applied with π-polarized light detuned blue of the $\left|5^2S_{1/2}, F=2\right\rangle$ to $\left|5^2P_{1/2}, F=2\right\rangle$ transition. The scheme

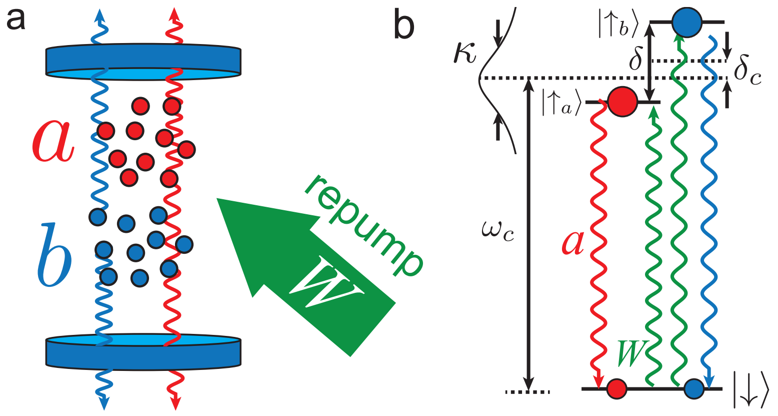

Figure 5.1: Diagram showing two ensembles within the cavity and simplified energy level diagram for the lasing process. (a) Two spatially separate ensembles a and b emit light within the same optical cavity. Incoherent repumping laser beams are applied from the side. The spatial selectivity of the ensembles results from applying different sets of dressing or repumping lasers to the atoms. (b) Simplified energy level diagram. The lasing excited states $|\uparrow_a\rangle$ and $|\uparrow_b\rangle$ are separated by frequency δ. The average of the two frequencies is at detuning δ_c from the cavity line center. Both lasing transitions are within κ of the cavity resonance frequency, ω_c.

with separated dressing lasers (II) uses π-polarized repumping to create a dark state $\left|5^2S_{1/2}, F=2, m_F=0\right\rangle$. Dressing light with linear polarization is applied from the side. Two spatially separate dressing lasers a and b with independent intensities and optical phases define the atomic ensembles a and b.

5.3 Modeling Two Ensemble Superradiance

This section extends the model of Eqns. 2.16 from Chapter 2 to the two-ensemble model. Although the full quantum nature of the scheme was analyzed in Ref. [141], here we extend the optical Bloch equations to two superradiant lasers with potentially different repump rates $W^{a,b}$, emission rates $\gamma^{a,b}$ and dressing laser couplings $\Omega^{a,b}$, Bloch vectors $\mathbf{J}^{a,b}$, and total populations $N^{a,b}$.

The models of Ref. [141] described a dynamical phase transition in the relative detuning between the light emitted by the two ensembles, with scaling behavior versus δ reminiscent of a second-order phase transition, with square root scaling of an order parameter $(\delta^2+W^2)^{1/2}$ near the critical point $\delta \to W$ showing a critical exponent of 1/2. The linewidth was predicted to diverge as δ approached the transition point. In contrast, we use the equations of Chapter 2 to model the qualitative behavior of the systems in the presence of asymmetry, and ignore the noise properties of the system. As this section explains, asymmetries are crucial for understanding the behavior of the coupled system. The asymmetries in our system take the form of atom number imbalances, differential emission rates, and differential detuning relative to the cavity mode (which causes a change in coupling to the cavity mode between the ensembles). The models show that differences in these parameters between the two ensembles can produce qualitatively very different behavior (e.g., one emission peak versus two) than for completely identical ensembles.

The model is essentially the same as the single ensemble model of Eqns. (2.16) except with

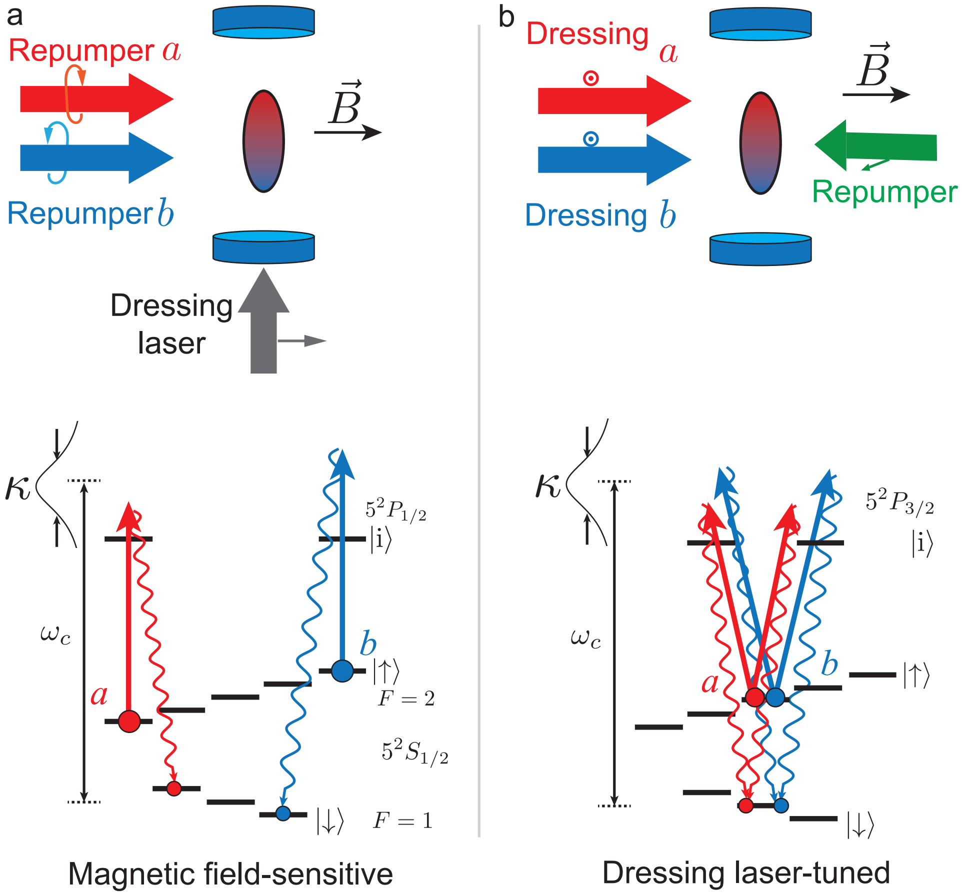

Figure 5.2: Lasing transitions for the two experimental configurations. (a) Magnetic-field control scheme (I). A single dressing beam at 795 nm is applied along the cavity axis with π-polarization. An applied magnetic field shifts the transition frequencies of the $5^2S_{1/2}$ ground states for ensembles a and b, which are separated by σ^+ and σ^- polarizations of two repumper beams to create two different dark states. The lasing transitions are between the stretched states $\left|5^2S_{1/2}, F=2, m_F=\pm 2\right\rangle$ and $\left|5^2S_{1/2}, F=1, m_F=\pm 1\right\rangle$. (b) Dressing laser control (II) scheme. Two dressing beams at 780 nm with linear-polarization are applied transverse to the cavity, and an incoherent repumping beam is applied transverse to the cavity with π-polarization. The lasing transition is between the clock states $\left|5^2S_{1/2}, F=2, m_F=0\right\rangle$ and $\left|5^2S_{1/2}, F=1, m_F=0\right\rangle$.

two independent ensembles a and b coupled to the same cavity mode with electric field $E(t)$

$$\dot{E} = \left(-\frac{\kappa}{2} + i\delta_c\right) E - i(g_2^a J_-^a + g_2^b J_-^b) \tag{5.1}$$

$$\dot{J}_-^a = i2g_2^a E J_z^a - \left(\frac{W^a}{2} + i\frac{\delta}{2}\right) J_-^a \tag{5.2}$$

$$\dot{J}_-^b = i2g_2^b E J_z^b - \left(\frac{W^b}{2} - i\frac{\delta}{2}\right) J_-^b \tag{5.3}$$

$$\dot{J}_z^\nu = -W^\nu J_z^\nu + \frac{N^\nu}{2} W^\nu + ig_2^\nu (J_-^\nu E^* - J_+^\nu E). \tag{5.4}$$

These equations are written in the frame of the average of the unperturbed emission frequencies, $(\omega_a^0 + \omega_b^0)/2$. Here, the superscripts a, b and $\nu \in a, b$ refer to the parameters corresponding to the ensembles a and b, respectively. The collective Bloch vectors are similar to those defined previously, $\langle \hat{\mathbf{J}}^{a,b} \rangle = (\langle \hat{J}_x^{a,b} \rangle, \langle \hat{J}_x^{a,b} \rangle, \langle \hat{J}_x^{a,b} \rangle)$, with the substitution of separate operators for the projection operators $|\uparrow\rangle\langle\uparrow| \to |\uparrow_{a,b}\rangle\langle\uparrow_{a,b}|$ (and similarly for $|\downarrow\rangle$). For instance, $J_z^{a,b} = (N_\uparrow^{a,b} - N_\downarrow^{a,b})/2$.

The two-photon Rabi frequency $g_2^{a,b} = g\Omega^{a,b}/(2\Delta)$ can differ between ensembles a and b because of unequal intensity in the a and b dressing beams in scheme (II). The repump rates $W^{a,b}$ may differ experimentally due to a mismatch between the center of the Gaussian profile of the beam and the atom cloud, but in our simulations we set $W^a = W^b$. Also, the cavity detuning δ_c can be set to be constant or the effect of cavity dispersive tuning can be included with the substitution $\delta_c \to \delta_c + 2\beta(J_z^a + J_z^b)$, where β is the differential cavity shift per atom for the states $|\uparrow\rangle$ and $|\downarrow\rangle$ that are differentially detuned from the cavity mode.

5.3.1 Expected Behavior

This section describes the expected behavior of the system given the model above, in two regimes: continuous phase error introduction and abrupt phase error introduction. Coupled phase oscillators with non-degenerate frequencies can exhibit a wide variety of behaviors. In the thermodynamic limit, where the number of classical oscillators $N \to \infty$, an array of phase oscillators with disordered frequencies (given by a Gaussian distribution, for instance) can undergo a phase transition to a frequency or phase-locked state. The Kuramoto model, a paradigmatic and extensively studied model in non-linear dynamics, exhibits this behavior [121, 2].

For the purposes of this calculation, we consider the mesoscopic collective dipoles formed by the ensembles of atoms within each ensemble a and b. This simulates the mean-field behavior of the ensembles.

In a similar configuration, the effect of an external driving field on a single superradiant laser was studied [43]. The model for this system was essentially the same as the one presented above in Equation 5.4, and was shown to be equivalent to a damped, driven van der Pol oscillator in the limit of small drive detuning and small drive strength. Importantly, the three-dimensional nature of the dynamical variables shows an AC Stark shift can cause frequency repulsion instead of attraction, which is not observed in a conventional two-dimensional phasor (i.e., the difference between a Bloch sphere and a phasor in a plane).

In the two-ensemble case, the coupling between population inversion and coupling strength to the cavity mode adds another feedback path into the system. The modified cooperativity $C' = C/\left(1 + \left(\frac{\delta_c \pm \delta/2}{\kappa/2}\right)\right)$ for ensembles a and b, respectively, so that the collective emission rates $(NC'\gamma)^{a,b}$ are not necessarily equal. Because of nonlinear scaling of the population inversion J_z with W compared to $NC\gamma$, the tuning of the dressed cavity mode in response to a change in $NC\gamma$ for one of the ensembles can depend crucially on the degree of asymmetry in the ensembles' parameters.

Synchronization in this system manifests as a locking of the two frequencies, $\omega_a = \omega_b$ even when the unperturbed frequencies are not equal, $\omega_a^0 \neq \omega_b^0$ or $\delta \neq 0$. In steady state, the time rate of change of the relative phases $\frac{d}{dt}(\omega_b - \omega_a) = 0$. There can be a constant phase offset ϕ_0 between the emitted fields that decreases to 0 when $\delta = 0$. In a power spectrum of the emitted light, the synchronization region of δ can be identified by the presence of a single frequency component.

For the symmetric case, $N^a = N^b$, $\Omega^a = \Omega^b$, and $W^a = W^b$. As the two ensembles' relative detuning δ is varied, synchronization occurs for $|\delta| \leq W$. Within the synchronization region, we expect a finite (but constant) opening angle ϕ_0 between the ensembles that decreases to 0 when $\delta = 0$. This should cause an increase in the collectively emitted power in the synchronization region, with the power highest at $\delta = 0$, since the atomic coherences $J_\perp^{a,b}$ are maximally aligned to each other ($\phi_0 = 0$). A finite phase offset that varies with δ within the locking range where oscillator frequencies are equal is commonly seen in injection-locked systems [105].

The same qualitative behavior is predicted by the full quantum mechanical model of Ref. [140]. However, the phase noise properties of the system (i.e., quantum-limited linewidth scaling) is not captured in our mean-field model. As δ decreases, the emitted photon frequencies ω_a and ω_b are attracted towards each other in a hyperbolic-like fashion and then meet to synchronize at the average frequency. In the case of the full model, the phase correlation or linewidth blows up at the transition point, marking the second-order phase transition to a synchronized state.

Qualitatively, this is easy to understand by considering the difference in rates in the system: the rate of relative phase precession of the two ensembles, with no coupling, is exactly the detuning δ. If the rate of relative phase precession (or, effectively, the rate of relative phase error) δ becomes less than the phase resetting rate, newly repumped atoms will align to the average faster than their phases can be pushed away from the average. The phase resetting rate (or rate of transfer to re-initialization in $|\uparrow\rangle$) is exactly the repumping rate W.

When asymmetries are introduced, the output spectrum of light changes significantly. There are a few different types of asymmetry that are crucial: differences in coupling to the cavity mode (from $C'_a \neq C'_b$ when $\delta_c \neq 0$), differences in emission rate from asymmetric dressing laser intensity ($g_2^a \neq g_2^b$), and differences in population ($N_a \neq N_b$).

First is the differential coupling to the cavity mode coming from the detunings $\delta_c \pm \delta/2$. Because a detuning δ_c from the dressed cavity resonance is necessary for stable operation (due to the feedback effect discussed in Chapter 2), as δ_c varies the two ensembles acquire different effective cooperativities C' leading to differential $NC'\gamma$. We see empirically that $\delta_c \approx \kappa/2$ for stable operation, which is close to side-of-fringe for the Lorentzian response $C' = C/(1 + \left(\frac{\delta}{\kappa/2}\right)^2)$ This effect could in principle be mitigated by detuning the dressing beam further from atomic resonance to reduce β, the dispersive shift per atom.

Next, in the configuration where the dressing beam is applied transverse to the cavity mode, there can be differences in the intensity of the dressing beam hitting the two ensembles so $\Omega_a \neq \Omega_b$, which causes a difference in $\gamma^{a,b} = \frac{\Gamma}{4}\left(\Omega^{a,b}/\Delta\right)^2$. This does not exist in the magnetic field-sensitive configuration of Section 5.5 where the RMS $\Omega^a_{\text{rms}} = \Omega^b_{\text{rms}}$ when the dressing laser is applied along the cavity axis. This arises both from the Gaussian beam profile and the diffraction pattern that results from the split waveplate used to create two beams. The waist of the dressing laser intensity in the axial direction of the cavity is comparable to the RMS atom distribution of about 1.5 mm. In order to change the relative populations N_a/N_b, we changed the fraction of the dressing laser that spatially addresses ensembles a and b. The populations in each ensemble are therefore coupled to the intensity of the dressing beams. We can partially compensate for the difference in $\Omega^{a,b}$ by scaling the relative intensities with AOMs, but could only control the relative scattering rates $\gamma^{a,b}$ at the 10% level.

Finally, an important asymmetry is the atom number imbalance between the two ensembles. Our method of measuring the relative atom numbers is uncertain on about the few percent level as the atom number measurement must be performed separately on each ensemble on successive runs of the experiment, and atom number fluctuations are at the few percent level. The ultimate limit to the relative atom numbers is the capability of driving the ensemble above the lower threshold. This comes from the atom number being coupled to the intensity of dressing beam, since the dressing beam size is somewhat comparable to the atom distribution. As the number of atoms decreases, so does the relative scattering rate, since it tends to be on the wing of the Gaussian beam profile in the z-direction. In principle, this could be mitigated by increasing the intensity in the dressing beam that addresses fewer atoms–however, there is a finite amount of power in our system. So when the scattering rate for ensemble a is less, it is not always possible to turn it up to the same level as ensemble b. Also, the thresholds for optimum power output change as a function of $N_{a,b}$, i.e., if $N_a C\gamma_a/2 \ll N_b C\gamma_b/2$ then the two ensembles cannot both simultaneously operate at optimum repumping, where stability is highest.

Figure 5.4 shows a particular simulation where the population $N_a = N_b$. A single emission peak is clearly visible in the spectrogram. Notably, as the detuning δ changes sign, the ensemble that actually lases changes. Also visible is a deviation from an X-cross with constant slope, meaning there is some synchronization happening near $\delta = 0$. For comparison, a completely balanced prediction is in Figure 5.4.

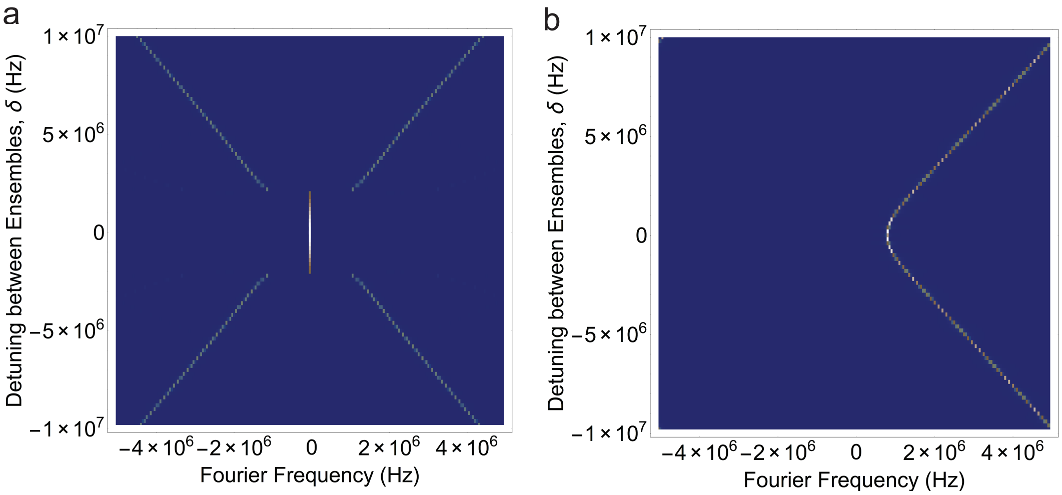

Figure 5.3: Comparison of theoretical lockup curves with population asymmetry with and without cavity tuning. Each horizontal trace in the spectrograms is a single power spectrum generated from an FFT after steady state is reached. (a) Balanced populations, $N_a = N_b$ with the cavity mode centered at zero frequency. Within the lock-in range, at $\pm W$, there is a single frequency component that increases in power close to $\delta = 0$. (b) The populations are balanced with $N_a = N_b$. Both ensembles are present, yet only one frequency component is visible for all δ.

5.3.1.1 Phase Response

In a separate set of experiments (with two dressing lasers, scheme (II)) $\delta = 0$ and the relative optical dipole phase of ensemble b is abruptly changed on a timescale faster than W. This experiment is only possible in the configuration where two dressing beams are applied transverse to the cavity, since the phase degeneracy needs to be broken on a timescale faster than W^{-1} and our control of the magnetic fields is not fast enough to introduce a phase difference. Also, in the magnetic field-sensitive configuration, the frequencies must be non-degenerate for the optical pumping to work correctly.

We simulate this experiment with the following sequence. First, both ensembles are initialized with nearly full inversion (but a small component J_- to allow superradiant emission to start). The system is allowed to evolve to steady state, where the magnitude of the combined optical dipole $|J_-^a + J_-^b|$ is constant in time. After steady state has been reached, we introduce a phase

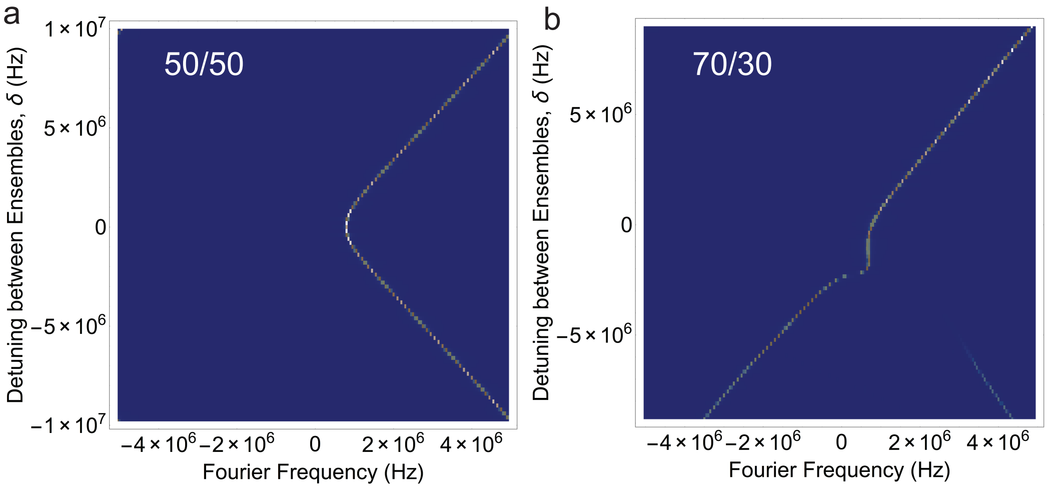

Figure 5.4: Comparison of theoretical lockup curves with population asymmetry in the presence of cavity tuning. Each row is a power spectrum of the light phasor after steady state is reached. The vertical axis is the detuning δ between the natural frequencies of the ensembles. Lighter color corresponds to higher power. The finite resolution is an aliasing artifact due to the finite amount of time sampled. For this simulation $N = 1.4 \times 10^6$, $\gamma = 10^4$ sec^{-1} and $W = 10^5$ sec^{-1}. (a) The populations are balanced with $N_a = N_b$. Both ensembles are present, yet only one frequency component is visible. (b) The populations are imbalanced, with 70% in a and 30% in b. The frequency scaling near $\delta = 0$ is much different than the balanced case, and at large negative δ there is still power emitted from b visible. Here, as opposed to in (a), a single same ensemble lases at all sδ.

deviation of $\Delta\alpha$ to ensemble b and calculate the response of the phase $\psi_+(t)$ of the cavity field $E(t)$. To eliminate the effect of cavity tuning, we also calculate the response $\psi_-(t)$ when the phase deviation is $-\Delta\alpha$ and construct the quantity $(\psi_+ - \psi_-)/2$.

5.4 Description of the Synchronization Process

Synchronization necessarily implies moving from a state of higher entropy to one of lower entropy, requiring dissipation into a bath of states that absorb the entropy. In the case of pendula coupled through a beam (as in the Huygens example), the beam that connects the pendula also provides coupling to the ambient environment, thereby providing dissipation. In our atom-cavity system, the dominant dissipation mechanism is the spontaneously scattered light involved in re-exciting atoms from $|\downarrow\rangle$ to $|\uparrow\rangle$ at rate W. Because our atomic ensemble is optically thin in the direction transverse to the laser cavity, the scattering process for the jth atom is not collective and causes single-atom collapse, erasing the relative quantum phase η_j in the single-atom superposition state: $\cos(\theta_j/2)\,|\uparrow\rangle_j + e^{\imath\eta_j}\sin(\theta_j/2)\,|\downarrow\rangle_j \rightarrow |\uparrow\rangle_j$. It is this relative phase ϕ_j that encodes the phase of the single-atom dipole and thus the phase of the light $\psi_j = \phi_j + const.$ that is radiated by the single oscillator. It is helpful to visualize ϕ_j as the azimuthal phase of the single-dipole Bloch sphere and the angle θ_j as a polar angle. Most importantly, the quantum collapse serves to erase any relative phase error $\Delta\phi_j = \phi_j - \phi_{\text{avg}}$ that had accumulated between the individual atom's optical dipole and an appropriately defined average of the phases of all of the optical dipoles of participating atoms, ϕ_{avg}.

The total cavity field is the sum of the optical fields radiated by each atom, with a resulting phase $\psi_{\text{avg}} = \phi_{\text{avg}}$. This cavity field aligns the optical dipole phase of a newly repumped atom to ϕ_{avg}. The combination of realignment to the average, accrual of phase errors, and erasure of phase errors is the physical origin of the quantum synchronization process.

Another dissipation channel in the atom-cavity system is the emission of photons from the cavity mode through the mirrors. However, this channel only provides *collective* information to the environment and should not erase single-atom phase errors. Detection of a photon exiting the cavity indicates that one atom has made a transition from $|\uparrow\rangle$ to $|\downarrow\rangle$, but does not indicate *which* atom made the transition. Still, the fast dissipation relative to the decoherence rate (the system is deep in the bad cavity regime with $\kappa \gg \gamma_\perp$) ensures that the cavity field adiabatically follows the total optical dipole of the atoms such that the phase of the optical dipoles ϕ_{avg} can be determined directly from the phase of the emitted light ψ_{avg}.

5.5 First Experimental Configuration: Magnetic-field-sensitive

In this configuration, the lasing is between the ground states $|\uparrow_a\rangle \equiv \left|5^2S_{1/2}F = 2, m_F = 2\right\rangle$ to $|\downarrow_a\rangle \equiv \left|5^2S_{1/2}F = 1, m_F = 1\right\rangle$ and $|\uparrow_b\rangle \equiv \left|5^2S_{1/2}F = 2, m_F = -2\right\rangle$ to lower state $|\downarrow_b\rangle \equiv \left|5^2S_{1/2}F = 1, m_F = -1\right\rangle$. The frequencies of these two transitions have opposite sensitivity to magnetic fields, so their relative frequencies could be changed by changing the magnitude of the magnetic field B_y applied along the $\hat{y}$ direction transverse to the cavity. The dressing laser had π-polarization and was injected along the cavity axis.

To prepare two distinct populations a and b, optical pumping beams with opposite σ^+ and σ^- polarizations were applied transverse to the cavity with the wave-vector of light $\vec{k}||\vec{B}$. This allows repumping to the stretch states $|\uparrow_a\rangle$ and $|\uparrow_b\rangle$. This configuration is shown in Figure 5.2(a). The polarization of the beam was set spatially through the use of a split quarter-wave plate (QWP) with fast and slow axes offset by 90°. The vertical position of the boundary between waveplates with respect to the waist of the beam set the fraction of the atomic population in a or b. Since the distribution of atoms in the $\hat{z}$ direction (direction of the cavity axis) is approximately Gaussian with width ~ 2 mm, a translation stage could easily position the waveplate boundary with enough precision for repeated trials.

To observe the steady state behavior of the lasers, the full light phasor from the emitted fields was detected in heterodyne and an FFT was constructed from the time record of amplitude and phase. On each successive trial of the experiment, the magnitude of the magnetic field is changed to change the relative detuning δ.

Figure 5.5(a) shows a spectrogram for which all the atoms are put into one magnetic sublevel.

The frequency essentially follows the predicted straight line except for a small deviation in the center, where there is no longer a dark state for repumping so that atoms spread out among all the $|F=2, m_F\rangle$ levels. However, this effect appears not to be large in the case of a single ensemble.

Figure 5.5(b) shows a spectrogram of the light emitted from the atomic ensemble as the B-field is changed. In the absence of any coupling between the two groups of atoms, there would be a simple X-cross, where the two ensembles emit at frequencies following straight lines. In the presence of coupling, we expect the emission peaks will be attracted to a common frequency.

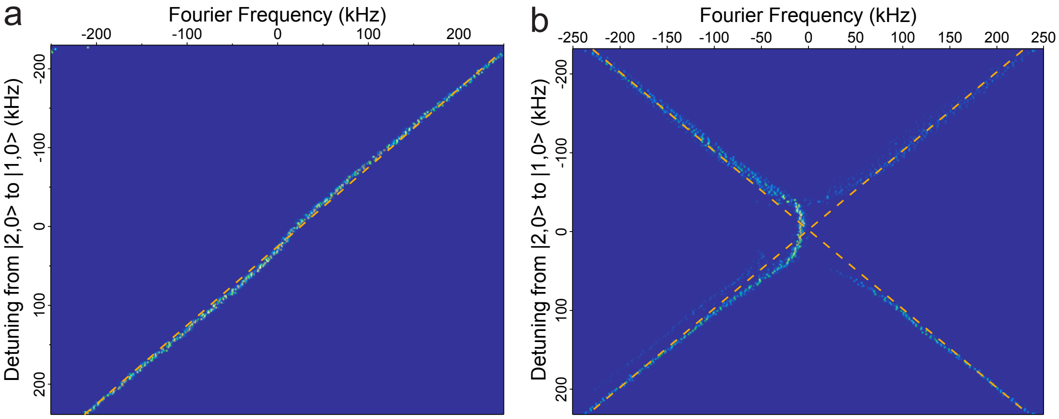

Figure 5.5: Response of one ensemble and synchronization of two ensembles in the magnetic field-sensitive configuration. The x-axis is the Fourier frequency for each power spectrum and the y-axis is the detuning of the atomic energy level given by changing the B-field. Color represents intensity in arbitrary units (lighter color is a higher intensity). (a) Spectrogram of the response of a single ensemble to changing detuning. For reference, a line with slope 1 (expected for no interaction) is plotted as an orange dashed line. From the maximal deviation of 6 kHz, the residual magnetic field is approximately 3 mG. (b) Spectrogram of the response of two ensembles to changing detuning. Two lines are plotted showing the expectation for non-interacting ensembles (orange dashed lines). When δ is below a critical value, the ensembles begin lasing at the same frequency and with a higher overall intensity.

This approach to the experiment has a couple of advantages. First, applying the dressing laser along the cavity axis allows operation in the Doppler-free regime because of the tight confinement from the optical lattice along the $\hat{z}$ direction. Having a low background decoherence rate Γ_D by operating in this parameter space means that the repump rate W need not be large to overcome the decoherence at rate Γ_D, so that the cavity pulling coefficient $P = W/\kappa \lesssim 10^{-4}$. This allowed for an investigation of cavity pulling and demonstrations of very low linewidth [24].

However, since the dressing laser is applied off-resonantly to the cavity and we have finite laser power, the scattering rate γ cannot be made higher than a few 100 s^{-1}. This in turn limits the absolute scale of the upper quench threshold for $W \propto NC\gamma$, which means that the range of synchronized δ is also limited since the synchronization range is set by W.

A key competing mechanism in this scheme is the breakdown of the atomic polarization as B_y approaches zero. Residual fields B_x or B_z can couple the near-degenerate $|F = 2, m_F\rangle$ levels, which causes a competition between optical pumping and the Rabi frequency between adjacent m_F levels. The second configuration of the following Section 5.6 eliminates this issue while introducing other features.

5.6 Second Configuration: Phase Controlled by Dressing Lasers

The second experimental configuration relies on changing dressing laser frequencies or phases to control the effective atomic transition frequency. To create two spatially separate ensembles with independently controlled optical dipoles, we apply two Raman dressing lasers that address either the upper or lower portions of the total trapped atomic ensemble (see Figure 5.13). This provides independent control of the dressing laser phases $\alpha_{a,b}$, angular frequencies $\omega_{a,b}$, and intensities are parametrized by a resonant-Rabi flopping angular frequency $\Omega_{a,b}$ for the $|\uparrow\rangle$ to $|\mathrm{i}\rangle$ transition. We can independently set the single-atom Raman decay rates $\gamma_{a,b}$ ($\approx 2\pi \times 250$ Hz) by controlling each laser's intensity. The relative number of atoms $N_{a,b}$ in each ensembles can be controlled by translating the spatial boundary between the dressing lasers along the cavity axis.

Because we utilize Raman transitions for the lasing process, the relevant total optical dipole phases that synchronize are given by $\phi_{a,b} = \eta_{a,b} + \alpha_{a,b}$. Here, $\eta_{a,b}$ is the phase associated with the coherence that develops between ground states $|\uparrow\rangle$ and $|\downarrow\rangle$ in each ensemble. Since the dressing phases are externally controlled parameters, the cavity-mediated interactions drive changes in the ground state coherences $\eta_{a,b}$ to synchronize the optical dipole phases $\phi_{a,b}$.

5.7 Time Dynamics

We study the dynamics of phase synchronization in the time domain for two ensembles with degenerate frequencies $\delta \equiv \omega_b - \omega_a = 0$. The dressing and repumping lasers are all turned on for 0.1 ms, during which time the two ensembles reach a steady state in which they emit at the same frequency and act as a single synchronized superradiant ensemble with $\phi_a = \phi_b$. An EOM (ThorLabs EO-PM-NR-C1) is used to quickly jump the phase α_b of the b dressing laser by an amount $\Delta\alpha_b$ in 30 ns. The timescale of the jump is much faster than the time dynamics of the resynchronization process and effectively creates an instantaneous error in the alignment of the optical phases $\phi_b = \phi_a + \Delta\alpha_b$.

To observe how this phase error heals in time, we allow the system to dynamically evolve for a variable amount of time $T_{\text{evol}} = 0$ to 1.5 μs before we rapidly extinguish the other dressing laser, setting $\Omega_a \to 0$. Subsequently, only ensemble b radiates into the cavity mode. We infer the change in ϕ_b from the difference in the phases $\Delta\psi$ of the emitted light just before the phase jump and just after T_{evol}.

5.7.1 Technical Details of Phase Measurement

In order to verify the amount of phase deviation $\Delta\alpha_b$ that is applied, we calibrated the applied phase difference with and without atoms. Without atoms, we overlapped the dressing beam b with a heterodyne LO beam onto a heterodyne photodetector and looked at the light phase of the dressing beam after $\Delta\alpha_b$ was applied versus the applied voltage. The same kind of measurement was performed with a single ensemble of atoms undergoing steady state superradiance, which produced a very linear relationship between the applied voltage and the observed phase shift, as shown in Figure 5.6.

The way we actually measure the phase is by performing linear fits to the time record of phase and interpolating to the point in time where the phase is changed. In the case where the time T_{evol} is scanned, the differential quantity $\psi(0) - \psi(T_{\text{evol}})$ is computed. Generally, averaging

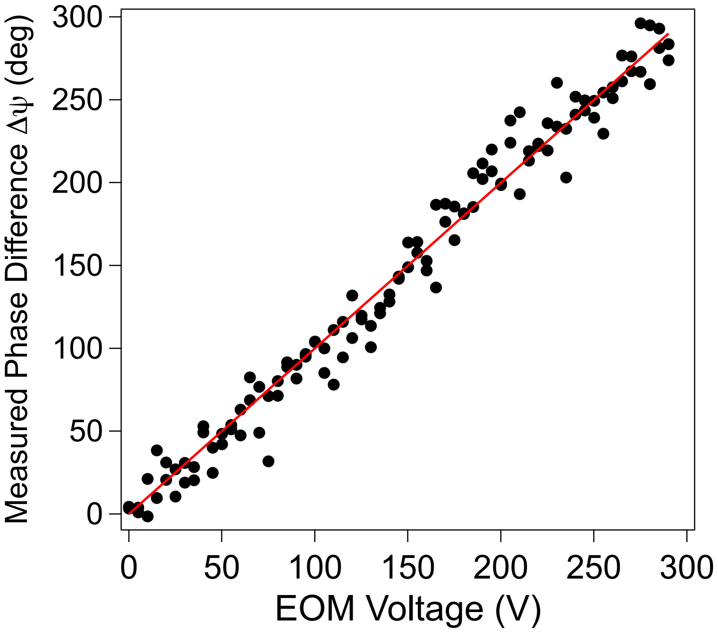

Figure 5.6: Measured phase shift of light $\Delta\psi$ with one ensemble versus EOM b voltage. Black points represent measured $\Delta\psi$ from interpolating to the time at which the phase deviation was applied. Red line is a linear fit to the data with slope $m = 1.00(1)$.

a DC measurement for longer reduces the phase variance due to photon shot noise. However, in the case of a linear fit in the presence of frequency chirping (which happens in the superradiant laser) and white noise, increasing the amount of data to which a line is fit can increase the noise in the value of an extrapolated point outside of the fit range. We empirically looked for an optimum amount of time to fit to, which occurred at around 15 data points (or around 6 μs). These linear fits can also be thought of in the frequency domain as a kind of band-pass filter centered on the instantaneous emission frequency of the laser. Figure 5.7 shows the noise in the phase difference $\Delta\bar{\psi}$ as a function of duration of the second fit window, which indicates a minimum standard deviation of about 19° at 7 μs.

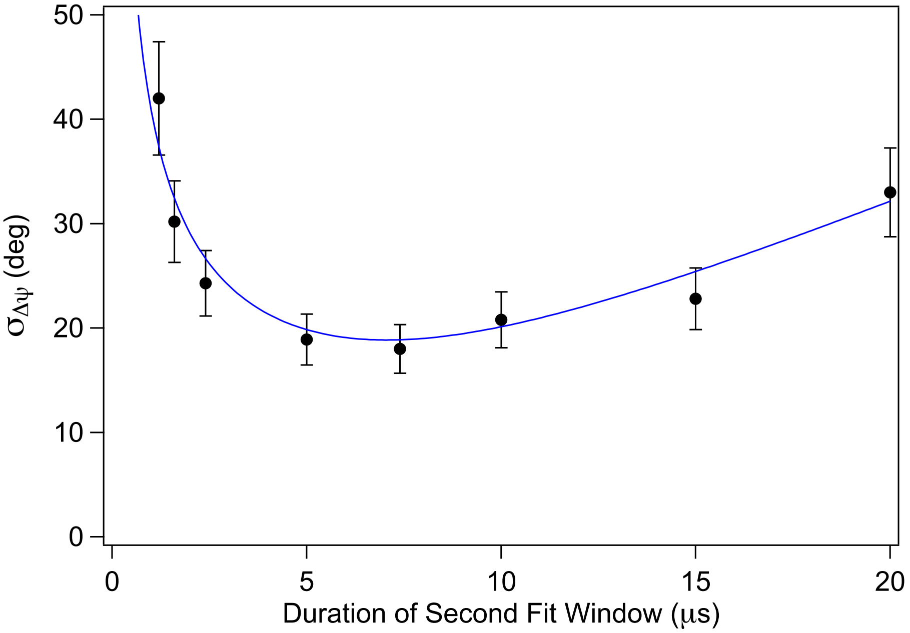

Figure 5.7: Noise in the phase measurement $\Delta\bar{\psi}$ versus duration of the second fit window. Blue line is a fit to a model $\hat{\sigma}_{\Delta\bar{\psi}}(t) = (a^2 + (b^2/t) + c^2t^2)^{1/2}$. This corresponds to a constant technical noise background set by a and photon shot noise term b and diffusion term c. The error bars reflect the statistical uncertainty of ≈ 30 measurements for each point.

There are a couple of major sources of systematic error in this phase measurement. First, when the dressing light for a is extinguished, the repumping will tend to increase the a ensemble inversion and will cause the dressed cavity frequency to move. However, this cavity chirping effect is in the same direction no matter what the direction of the phase deviation of the laser. And, the physics is expected to be the same whether the dressing laser b phase is jumped $+90°$ or $-90°$—only the opening angle between the two dipoles should matter, not the sign. So, by averaging the result of two successive trials in which $\Delta\alpha_b = \pm 90°$, we cancel out the cavity chirping effect.

Another systematic error is slow drift of the relative path length which would cause fluctuations in the optical phase of the dressing lasers at the atoms, $\alpha_b - \alpha_a$. To account for a slowly varying relative optical phase, we measure $\Delta\psi$ at positive and negative $\pm\Delta\alpha_b$ while scanning the phase of the AOM b from $0°$ to $360°$, stepping by $180°$ between points. For example, two experimental trials for $\Delta\alpha_b = +90°, -90°$ are performed at $\phi_{AOM} = 0°$, then at $\phi_{AOM} = 180°$, followed by $12°$, $192°$, etc., until all ϕ_{AOM} have been sampled. Then, averages are constructed for ψ_+ and ψ_- and they are combined into $\Delta\bar{\psi} = \frac{1}{2}(\psi_+ - \psi_-)$.

The measured quantity $\Delta\bar{\psi}$ as a function of the evolution time T_{evol} is shown in Figure 5.8(b). Here the phase jump is $\Delta\alpha_b = 90°$, and we see that $\Delta\bar{\psi}$ is also $90°$ near $T_{\text{evol}} = 0$. The phase $\Delta\bar{\psi}$ then relaxes back toward $0°$, settling at an intermediate value such that $\phi_a = \phi_b$. The timescale for relaxation is close to the repumping rate W^{-1}, i.e., the characteristic rate at which phase errors are erased.

The equilibrium phase at large T_{evol} is mostly determined by the ratio of the relative magnitudes of the optical dipoles of the two ensembles just before the evolution period. The magnitude of each collective dipole is proportional to the number of participating synchronized atoms ($N_{a,b}$) and the emitted electric field per atom ($\propto \sqrt{\gamma_{a,b}}$). The *relative* dipole magnitude can be roughly characterized by $R_d \equiv (N_b\sqrt{\gamma_b})/(N_a\sqrt{\gamma_a}) = 1.5$ and 4.0 for the solid and open data sets in Figure 5.8.

A simple model for the phase prediction is vector addition of the optical dipoles whose size is proportional to $J_\perp^{a,b}$. The long-time behavior with $T_{evol} \gg W^{-1}$ and $\Delta\alpha_b = 90°$ is that $\Delta\bar{\psi}$ will relax to $\Delta\bar{\psi}_e = \tan^{-1}(R_d)$. For comparison, we label the steady state phase given by the full numerical simulation as $\Delta\bar{\psi}_n$. For the data with more balanced populations (solid), the ensembles equally pull each other's optical phases $\phi_{a,b}$ and the light phase relaxes to $\Delta\bar{\psi} = 51(3)°$, close to

$(\Delta\bar{\psi}_e, \Delta\bar{\psi}_n) = (56°, 55°)$. In contrast, in the more imbalanced (open) data, the unobserved ϕ_a is pulled more rapidly toward the phase of ϕ_b, and the phase relaxes toward $\Delta\bar{\psi} = 71(2)°$, while $(\Delta\bar{\psi}_e, \Delta\bar{\psi}_n) = (79°, 73°)$, i.e., closer to the phase of ensemble b at $T_{\text{evol}} = 0$.

The experimental steady state value of $\Delta\bar{\psi}$ versus dipole ratio R_d is plotted in Figure 5.9. The experimental measurement comes from taking the average of the last several data points. For reference, the simple two-level theory of Equation 5.4 is shown as the solid black line. The range over which R_d can be scaled is limited by the decreasing upper lasing threshold for W as R_d is decreased. That is, as one of the ensembles is made smaller, it eventually requires a very low W to emit light at all. The data is basically in agreement with the simple prediction line and obtains reasonable agreement with the two-level model theory.

5.8 Frequency Response

We next consider the case in which a continuous source of phase error is introduced between the two ensembles by detuning the dressing laser frequencies. As δ deviates from zero, the total power emitted by the two ensembles decreases as shown in Figure 5.10. For $|\delta| > W$ the total output power is roughly constant. At the transition point, the two ensembles largely behave independently, emitting at their respective natural lasing frequencies. The characteristic frequency scale is set by W since any relative phase accumulated between the ensembles is reset through repumping, as discussed in Section 5.4. The observed maximum synchronized power output is a factor of 2.2(1) greater than the unsynchronized power output, while we predict a factor of 1.8(2). This estimate is based on the quenching behavior of the output power with repumping rate that accounts for changes in population inversion of each ensemble [22, 93]. The asymmetry of the total power for positive and negative δ is also reflected in the asymmetric behavior in the spectra of Figure 5.11 as discussed below.

We can observe the transition from synchronized to unsynchronized behavior in the frequency domain by looking at the spectral properties of the light emitted from the cavity. In the spectrograms of Figure 5.11, each row is a frequency spectrum of emitted light from the cavity, with

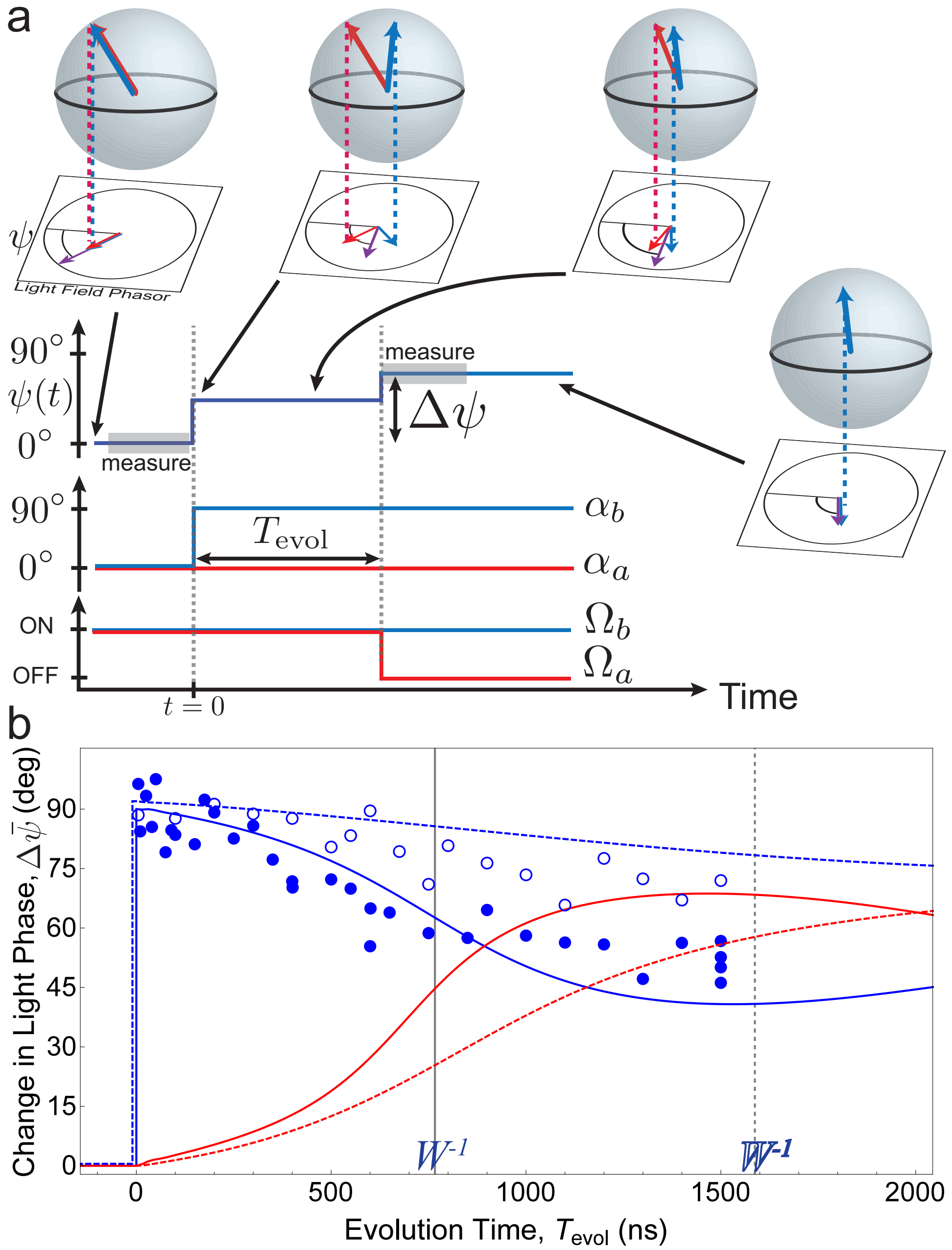

Figure 5.8: Healing of an instantaneous phase error between optical dipoles. (a) Timing diagram and visualization of atomic Bloch vectors. Before time $t = 0$ the two dipoles interact and synchronize. At $t = 0$, dressing laser phase α_b is jumped by 90°. The ensembles' interaction begins to heal the relative phase error. At $t = T_{\mathrm{evol}}$, dressing laser a is turned off ($\Omega_a \to 0$) so that only ensemble b radiates into the cavity. The difference $\Delta\bar{\psi}$ in the phases of the radiated light in the gray windows before $t = 0$ and after $t = T_{\mathrm{evol}}$ indicates the change in the optical dipole phase $\Delta\phi_b = \Delta\bar{\psi}$. The upper panels provide cartoon visualizations of phasors representing the radiated fields (red for a, blue for b, purple for the sum) and Bloch vectors. (b) Light phase change $\Delta\bar{\psi}$ vs. evolution time T_{evol}. The solid and open points correspond to experiments with dipole ratios $R_d = (1.5, 4.0)$, respectively. Vertical solid and dashed lines show the characteristic time scale of the respective single-atom repumping rates for the two data sets $W^{-1} = (0.77, 1.6)$ μs corresponding to (solid, open) data. The solid and dashed curves are simulations for the respective data (red for the unobserved ensemble a, blue for b).

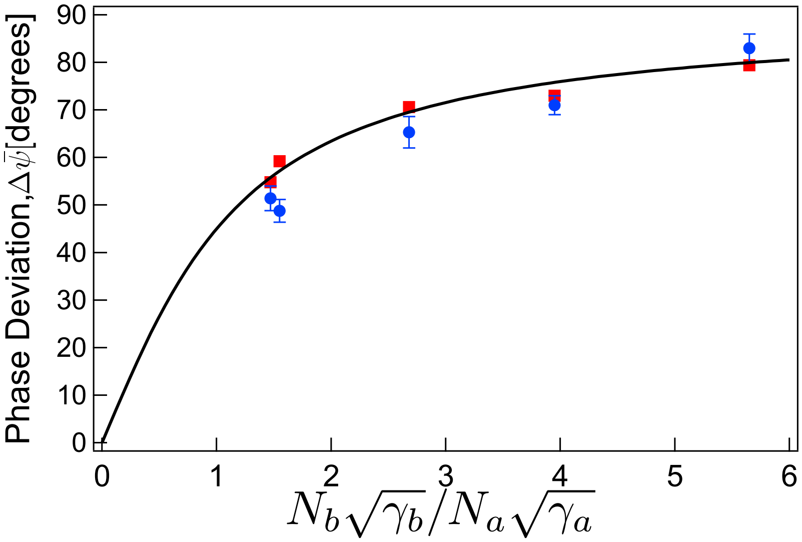

Figure 5.9: Light phase deviation $\Delta\bar{\psi}$ versus dipole fraction R_d. Data (blue circles) and prediction from the two-level model (red squares) are shown with the simple prediction of $\tan^{-1}(R_d)$ (solid line). The two-level model was averaged over several values for W, while the data was averaged over the last several points near the maximum $T_{\text{evol}} = 1500$ ns.

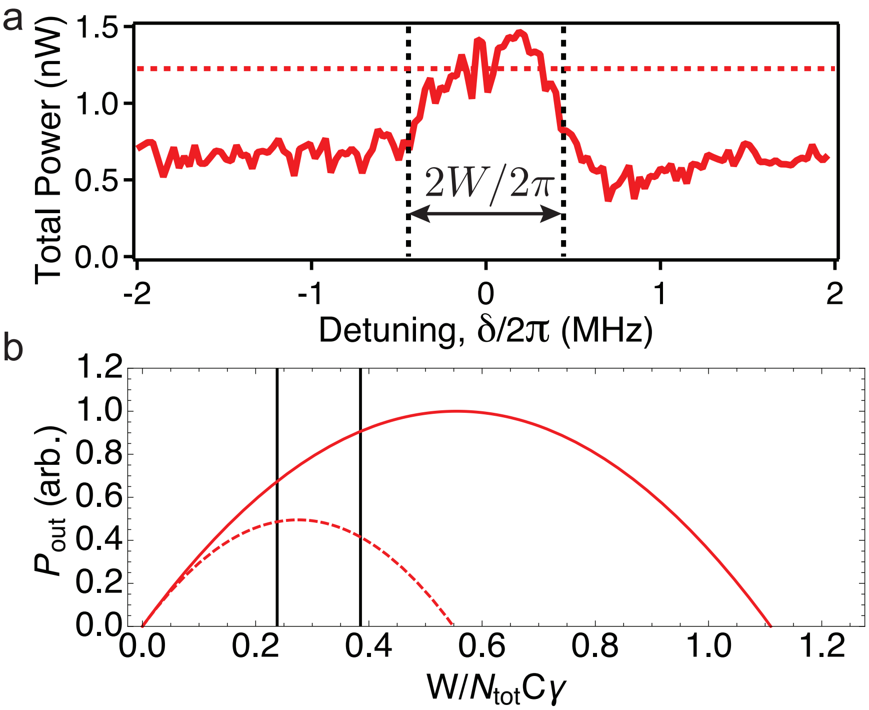

Figure 5.10: (a) Total output power versus detuning for the spectrograms of Figure 5.11. Vertical dashed lines are at the repumping rate $\pm W/2\pi$. The horizontal dashed line is the predicted maximum synchronized output power. (b) Theoretical plot of the expected output power versus $W/(N_{\text{tot}}C(\gamma_a+\gamma_b)/2)$ for the unsynchronized case (dashed) and synchronized case (solid). For a given W, the coherent power emitted from the synchronized ensembles is higher at $W>0$. The black line on the left corresponds to the expectation from the measured W, $\gamma^{a,b}$ and $N^{a,b}$, while the black line to the right corresponds to the ratio of the maximum power to the averaged $|\delta|>W$ from (a).

brighter colors indicating higher power. Each power spectrum is calculated from 80 μs of the time record. The two-dimensional power spectrum is created by repeating the measurement at a series of different detunings δ, with values shown along the vertical axis.

For $|\delta| \gg W$, the two ensembles of atoms emit at frequencies very close to the unperturbed Raman transition frequencies. As $|\delta|$ decreases, the emission frequencies ω_a and ω_b are pulled toward each other as the rate of relative phase error δ nears the error erasure rate W. We note that we do not observe nor expect a region of repulsive synchronization that appears when injection locking a single superradiant ensemble to an externally applied drive [43]. For $|\delta| \lesssim W$, the erasure of phase errors dominates and the two ensembles radiate at a single frequency.

The observed spectrum qualitatively agrees with the results of the mean-field model introduced in Equation 5.4, exhibiting a hyperbolic-like approach (Region I) to the synchronized state (Region II). However, there is significant asymmetry in the power spectrum. Part of this asymmetry arises from a finite detuning of the average Raman transition frequency from resonance with the cavity resonance frequency by amount $\delta_c = - = 2\pi \times 4$ MHz $\approx \kappa/3$, an operating condition favorable for suppressing relaxation oscillations [19], yet one that introduces an imbalance in the coupling to the cavity between ensembles. Other causes of asymmetry are imbalances in the optical dipole magnitudes (both N and γ) for the data in Figure 5.11. Numerical modeling indicates that the effects of these small asymmetries are magnified by the interaction between the ensembles.

We also show in Figure 5.11(b) that many different behaviors can be observed depending on the operating parameters. This data shows a significant asymmetry in the emitted power (iii) from each ensemble for $\delta > 0$ and $\delta < 0$. Many of these behaviors are observed in the numerical mean-field models of our system (reference earlier discussions here), but other features, indicated in Figure 5.11(b) are not: (i) the parallel-running frequency component in the lower right-hand quadrant, (ii) the extra frequency components at $\pm\delta/2\pi$, and the asymmetry in the observed linewidth of the two emission peaks of both Figure 5.11(a) and (b). Note the fractional power in each sideband (ii) is small, $< 8\%$ of the total power in each frequency spectrum.

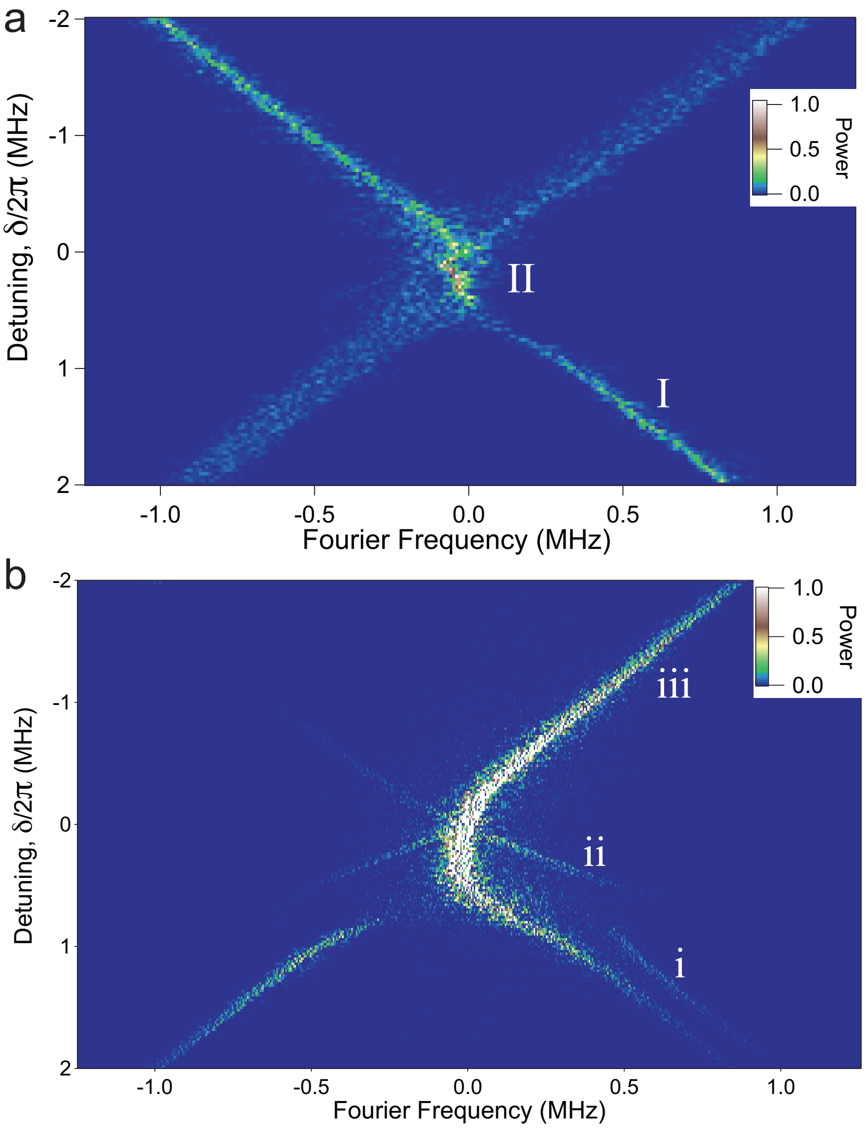

Figure 5.11: Symmetric and asymmetric spectrograms in the two-dressing-laser configuration of Section 5.8. The vertical axis is the detuning of the dressing lasers, δ, and the horizontal axis is the Fourier frequency of each power spectrum. The power (color scale) is normalized to the maximum power across the entire spectrogram. (a) Each power spectrum represents the average of 5 power spectra for each δ. Collective dipoles are roughly balanced with $N_a/N_b = 0.6$ and $\gamma_a/\gamma_b = 0.8$. (b) Asymmetric operating conditions, $N_a/N_b = 1.1$ and $\gamma_a/\gamma_b = 1.6$.

5.8.1 Reasons for Asymmetry

Here I briefly discuss some mechanisms that could be responsible for the broad lineshapes seen in the spectrograms of Figure 5.11. In prior studies, linewidth broadening was seen to arise from an inversion-dependent frequency pulling mechanism. Here, this effect would broaden both peaks [24, 22], and is therefore not the source of the difference in linewidths. Attempts to identify other classical mechanisms for the asymmetric broadening have been unsuccessful and the broadening remains an interesting topic for future theoretical and experimental study, with the intriguing possibility that this is a fundamental quantum noise effect [141].

Two representative single power spectra from Figure 5.11 are shown in Figure 5.12 for detunings $\delta = 55$ kHz and 1.4 MHz. A clear difference in the lineshapes for the positive and negative frequency ensembles can be seen–one is much broader and has less total power. At synchronization, there is still some broadening but more output power, corresponding to the central feature in Figure 5.10.

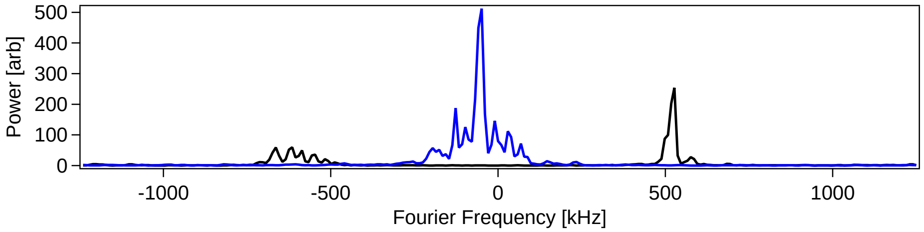

Figure 5.12: Averaged power spectra for two detunings. Data corresponds to Fig. 5.11 (a), with small detuning $\delta = 55$ kHz (blue) showing synchronized behavior and larger detuning $\delta = 1.4$ MHz showing two unsynchronized ensembles.

Classical Heterodyne Noise—Classical noise in the relative phase (e.g., due to fluctuating path length differences) between the dressing laser and the LO beam, or the LO beam and the light emitted by the atoms, ought to cause a common-mode shift of both frequency components. This noise ought to be common mode for both frequency components, and would also appear solely in an FFT of only the phase rather than the full phasor. We don't see the same lineshape for both frequency components, and the differential linewidth is present in both phase-only and amplitude-only FFTs.

Differential Cavity Pulling—We do not expect to have an effect that would cause significant differential cavity pulling for both ensembles, as the amount of cavity pulling does not depend on the detuning from cavity resonance [21]. This would have to mean that the transverse broadening rates $\gamma_\perp^{a,b}$ for each ensemble significantly differ and even might fluctuate (to explain very different lineshapes). To estimate the size of this effect, given a 30 MHz dressed cavity shift for 10^6 atoms total, and pulling coefficient $P = \gamma_\perp/\kappa = 0.02$, a loss of 5% of the atoms over an FFT window of 100 μs would cause a 30 kHz shift in the emission frequency. To explain a typical differential linewidth, there would have to be a factor of 5 difference in $P_{a,b}$, a very high value that is inconsistent with measurements of the repumping beam profile.

Quantum Noise in Linewidth Near Threshold—The expected fundamental linewidth is on the order of 5 Hz for a typical experiment. We know that $N_a/N_b = 1.6$ and $\gamma_a/\gamma_b = 1.2$. Then, $W/NC\gamma \approx 0.6$. This is very close to $NC\gamma/2$, the approximate location of the optimum repumping rate. To explain an increase in linewidth from 5 Hz to 30 kHz, a factor of 6×10^3 increase, the laser would have to be operated very near an upper quench threshold [94].

Fluctuating AC Stark Shifts from Intracavity Light—For this effect, we assume the following model: the larger ensemble's frequency is unperturbed, but it undergoes relaxation oscillations that modulate the AC Stark shift that the smaller ensemble experiences. This would correspond to the "repulsive" regime of injection locking [43], since the detuning $\delta \sim 1$ MHz and $W \sim 1.4 \times 10^6$ sec^{-1} = 220 kHz. In the repulsive regime of injection locking or synchronization, the laser emission frequency is AC Stark shifted as the power at the laser emission frequency decreases and the power at the drive increases. For the representative data set of Figure 5.12, the RMS AC Stark shift would have to be ≈ 80 kHz.

For the operating parameters of Figure 5.12, the ideal Rabi frequency of the stronger ensemble would be $\Omega = 2g\sqrt{M_c} = \frac{1}{2\sqrt{2}}\frac{(NC\gamma)^2}{\delta}$ at $W_{\text{opt}} = NC\gamma/2$. Then the peak AC Stark shift would be $\frac{\Omega^2}{4\delta} \approx \frac{1}{8}\frac{W^2}{\delta} = 6$ kHz. The absolute size of the frequency modulation in the data seems too large to be described by AC Stark shifts, even if relaxation oscillations of the large ensemble causes a large amount of amplitude modulation of its output light.

Modulation of Scattering Rate γ—There is electric field interference from the overlap of the leakage field of dressing laser a and dressing laser b, and vice versa. This provides a perturbation to the scattering rate γ^a which is proportional to $\Omega^a \Omega^b_{\mathrm{leak}} \cos(\delta t)$, where Ω^b_{leak} is the dressing beam leakage field from diffraction at the location of ensemble a. This leads to amplitude modulation sidebands on the light emitted from a , so that one of the modulation sidebands on ω_a are approximately at the frequency ω_b (as $|\omega_a - \omega_b| \approx \delta$ when $\delta \gg W$). However, the fractional size of the modulation sidebands in power is $< 1\%$ of the carrier power from a when $|\delta| = 500$ kHz, so this effect is likely too small to explain the large linewidth.

5.9 Additional Experimental Details

Here I provide some additional details about the optical setup, including the split waveplate and the optical setup used for the two dressing beam configuration of Section 5.6.

5.9.1 Split Waveplate

In both the magnetic field-sensitive and dressing laser configuration, a "split" waveplate was put in the beam path to address different sub-ensembles of the atoms to create ensembles a and b. This involved a CVI single-order quarter wave-plate being sliced in half along a diameter of the circular glass piece aligned 45° from the fast axis, and then reassembled with one half of the wave plate flipped by 180°. The respective fast and slow axes of the two halves are then rotated by a relative angle of 90° between the halves, leading to an opposite circular polarization rotation for linearly polarized light offset by 45° from the original fast axis for the top and bottom waveplates. In other words, if a given input state produced σ^+ polarization initially, it now produces σ^+ through the half of the waveplate in the original orientation and σ^- on the half of the waveplate that has been flipped.

In the dressing laser setup, we actually use an intensity filter to split up the dressing beam. We start by injecting dressing beam a and b with orthogonal polarizations along orthogonal fast and slow axes of a polarization-maintaining (PM) fiber (with extinction ratio > 20 dB). The beams exit the fiber and go through a half-wave plate and quarter-wave plate to correct for any static birefringence in the fiber owing to input misalignment and end up as σ^+ and σ^- beams heading toward the split waveplate. The split waveplate turns both σ^+ and σ^- components into the same linear polarization–with the B-field along the z-direction setting the quantization axis, this is linearly polarized light (a combination of σ^+ and $\sigma-$ in the atomic basis). A final PBS cube rejects the portions of the light that are not in the same linearly polarized basis. Figure 5.13 depicts this polarization selection setup.

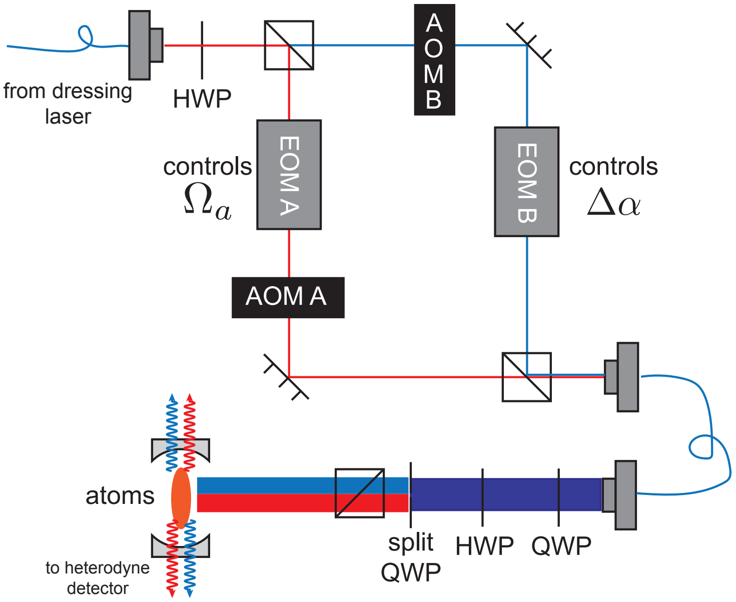

Figure 5.13: Schematic of the dressing laser "switchyard" of Section 5.6. The dressing laser gets split between two paths, which each feature an AOM (for controlling the beam power level and frequency difference δ) and an EOM for controlling either the amplitude of the a laser, Ω_a, or the phase of the b laser, $\Delta\alpha_b$. The overlap is then sent to the atoms, with a split waveplate and a PBS allowing the b to hit one sub-ensemble and a to hit another sub-ensemble.

However, due to the small gap between waveplates, there is some degree of diffraction that occurs. This produces an intensity pattern close to the standard Airy function that is normally seen at sharp transitions in apertures. Diffraction is especially important when the dressing lasers have opposite polarization, since small leakage fields from a into the volume addressed by b can, through interference with the strong b or a fields, result in a large intensity fluctuation at the difference frequency of the dressing lasers. The amount of diffraction we see is shown in Figure 5.14.

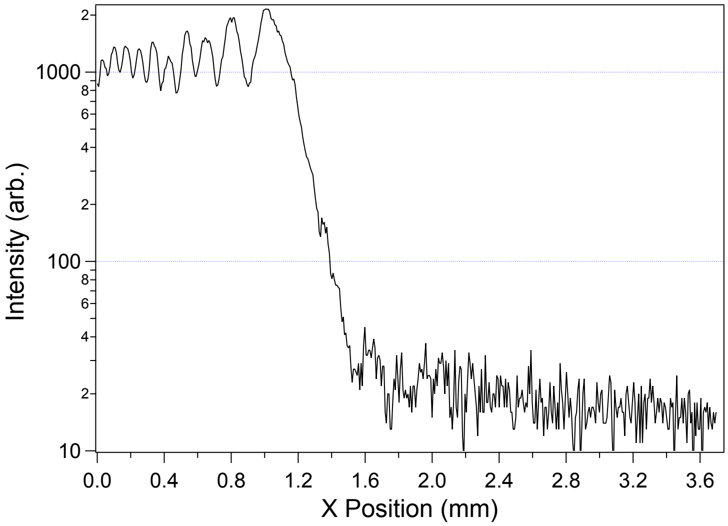

Figure 5.14: Intensity pattern of light diffracted from waveplate. Vertical axis has a log scale. This trace represents a single vertical slice along the 2D image of the beam after 3.75 in of propagation past the QWP and PBS cube. The leakage field is at least a factor of 100 less than the peak intensity of the beam (since there is no background subtraction in this plot).

Chapter 6

Enhancing Quantum Phase Resolution with Spin Squeezing: Beyond 10 dB

In this chapter, I describe efforts to generate a high degree (> 10 dB) of spin squeezing in our cavity QED system. First, I provide an overview of non-demolition measurements and squeezing generation in our atom-cavity system. I discuss the limitations to previous approaches, and describe improvements to the experimental system that will allow further squeezing and entanglement generation. I present measurements showing that our system is capable of the two key ingredients for performing phase measurements beyond the standard quantum limit: a detection noise floor well below the initial quantum level of noise, and the capability to preserve coherence. Finally, I outline the promising prospects for future improvements to our scheme.

6.1 Conditional Spin Squeezing

Our approach for generating spin squeezing is to use measurement-induced entanglement, representing a "top-down" approach to creating quantum correlations rather than a "bottom-up" paradigm that relies on precisely controlling interactions between two atoms at a time. By making collective quantum non-demolition (QND) measurements of populations of atomic spin states to first measure the quantum noise of an ensemble of atoms, we can subsequently subtract the correlated quantum noise from a second measurement. This is termed "conditional" spin squeezing since it is only the difference between successive measurements that has noise below that of unentangled atoms, i.e., the second measurement has less noise when *conditioned* on the outcome of the first measurement. Each measurement taken alone has the full quantum noise level, but the quantum noise is common to both measurements and cancels in the difference of the two. Conditionally spin squeezed states can be injected into standard Ramsey measurement sequences and achieve improved performance [110, 3].

Quantum non-demolition measurements also have advantages from their non-destructive nature. Cavity-aided QND measurements can impart very few photon recoils (< 0.1 photon recoils per atom), so unlike fluorescence measurements that necessarily produce many photon recoil events, the atomic sample is not significantly heated [31]. This could allow for a fast cycle time since if a measurement is fast enough, there could be minimal atom loss from the optical trap due to heating and atoms could potentially be re-cooled before being probed again. Our measurements are also fast, between 20 to 100 μs, so do not add significant delays that could preclude their usefulness in a real sensor.

6.1.1 Standard Quantum Limit

Coherent spin states (CSS) are classically correlated states commonly used in precision measurements using atoms. A CSS is composed of N atoms whose atomic Bloch vectors are oriented in the same direction on average. For a CSS on the equator of the Bloch sphere oriented along the x-axis, the CSS would be described by the product wavefunction $|\mathrm{CSS}\rangle = \bigotimes_{i=1}^{N} \frac{1}{\sqrt{2}}(|\uparrow\rangle + |\downarrow\rangle)$. This non-entangled or classically correlated state ideally has noise in each spin projection given by the Heisenberg uncertainty relations for non-commuting observables, e.g., for a Bloch vector $\vec{J}$,

$$\Delta J_z \Delta J_y \geq |J_x|/2. \tag{6.1}$$

Here, $\Delta J_k = \sqrt{\langle J_k^2 \rangle - \langle J_k \rangle^2}$ for $k \in x, y, z$ is the standard deviation of the measurement outcome [67, 135]. For the CSS oriented along the x-axis of the Bloch sphere mentioned above, the mean polar angle of the Bloch vector $\theta = 0$ and mean azimuthal phase $\phi = 0$. In the limit of large N, the noise $\Delta\theta \approx \Delta J_z / |\langle \hat{\mathbf{J}} \rangle|$ and $\Delta\phi \approx \Delta J_y / |\langle \hat{\mathbf{J}} \rangle|$. The noise distribution is isotropic in θ and ϕ so that $\Delta\theta_{SQL} = \Delta\phi_{SQL} = 1/\sqrt{N}$, a scaling termed the Standard Quantum Limit (SQL). The quantum noise is enhanced when the noise ΔJ_z is small while the signal $|\langle \hat{\mathbf{J}} \rangle|$ remains large.

Equivalently, the fundamental uncertainty relationship for the angular variables is

$$\Delta\theta\Delta\phi \geq \frac{1}{N}. \tag{6.2}$$

These angular quantities θ and ϕ corresponding to the spin projections ΔJ_z and ΔJ_y perpendicular to the average Bloch vector $\langle\hat{\mathbf{J}}\rangle$ oriented along $\hat{x}$ are the two relevant quadratures for the following discussion of spin squeezing.

6.1.2 Spin Squeezed States

Spin squeezed states can have angular resolution below the SQL, at the expense of increased noise in an orthogonal quadrature. In a similar system to the one discussed in this chapter, we have prepared states enhanced by an order of magnitude with $(\Delta\theta_{SQL}/\Delta\theta)^2 \geq 10$ [16]. For this to be possible, the noise in ΔJ_z is reduced while the signal $|\langle\hat{\mathbf{J}}\rangle|$ still persists. To satisfy the uncertainty relation of Eqn. 6.2, the noise in ΔJ_y is increased due to both fundamental quantum back-action and back-action from the method used to probe the atoms (discussed later in Section 6.2).

In the absence of any extra probe-added noise, the he fundamental limit to the quantum-enhanced reduced uncertainty in $\Delta\theta$ is the Heisenberg limit, which scales as $\Delta\theta_{HL} = 1/N$. The fully symmetric Dicke state on the equator has this lowest possible level of uncertainty at the expense of complete uncertainty in ϕ, represented as a narrow ring on the Bloch sphere equator [4]. The scaling of $1/N$ essentially means that there is “rounding error” on the order of the spin of a single atom. For the number of atoms in our experiment, $N \approx 10^6$, the Heisenberg limit corresponds to a 60 dB decrease in phase variance $(\Delta\theta_{SQL}/\Delta\theta)^2$ over the SQL. For $N = 10^6$ ^{87}Rb atoms in our cavity with finesse $F = 2700$, upwards of 30 dB of squeezing is theoretically possible assuming perfect detection efficiency of the light applied to the atoms [33].

6.1.3 Probing to Generate Spin Squeezed States

Our measurements reduce the noise in the atomic pseudospin projection J_z. As discussed in Chapter 1, we measure the collective spin operator $\hat{J}_z = (\hat{N}_\uparrow - \hat{N}_\downarrow)/2$ by performing successive measurements of the cavity resonance frequency. Here, the number operators are the projections $\hat{N}_\uparrow = \sum_i |\uparrow\rangle_i \langle\uparrow|_i$ and $\hat{N}_\downarrow = \sum_i |\downarrow\rangle_i \langle\downarrow|_i$. A typical experimental sequence to generate squeezing involves optical pumping into $|\downarrow\rangle$, performing a $\pi/2$-pulse, measuring the dressed cavity shift with result labeled ω_{cp} to infer the number of atoms in $|\uparrow\rangle$, performing a π-pulse to swap the populations in $|\uparrow\rangle$ and $|\downarrow\rangle$, then measuring the number of atoms that were originally in $|\downarrow\rangle$ by converting a second measurement of the cavity frequency ω_{cf} to $N_\downarrow$. The difference of these measurements of $N_\uparrow$ and $N_\downarrow$ constitute a measurement of J_z, labeled J_{zp}. This creates an entangled state that has reduced ΔJ_z and still maintains coherence. Once this entangled state is generated, we perform another measurement of J_z, with measurement outcome labeled J_{zf}. The quantum noise cancels in the difference of two successive measurements $(J_{zf} - J_{zp})$, so the noise $\Delta(J_{zf} - J_{zp})$ is limited by detection noise (e.g., photon shot noise or other technical backgrounds) and back-action due to probing the atoms with a large number of photons in a measurement window.

This measurement sequence and the resulting states of the collective Bloch vector are illustrated in Figure 6.1. The quantities $J_{zp} = (N_\uparrow - N_{\downarrow p})/2$ and $J_{zf} = (N_\uparrow - N_{\downarrow f})/2$ are constructed using the cavity frequency shift measurements $\omega_{\uparrow c}$, ω_{cp}, and ω_{cf} to infer atom numbers $N_\uparrow$, $N_{\downarrow p}$, and $N_{\downarrow f}$. In taking the difference $(J_{zf} - J_{zp})$, the noise in $N_\uparrow$ is common mode and we only see the noise $\Delta(N_{\downarrow p} - N_{\downarrow f})$. The quantum projection noise is common mode to the two measurements so only technical noise remains, setting the level of squeezing when signal loss is taken into account. The collective Bloch vector goes from a CSS on the equator of the Bloch sphere to a spin squeezed state offset from the equator due to the quantum projection noise in the initial measurement J_{zp}.

For the purposes of this chapter, I label the result of two successive cavity frequency measurements ω_{cp} and ω_{cf} and the RMS noise in the difference $\Delta\omega_d = \Delta(\omega_{cf} - \omega_{cp})$. The fluctuation due to projection noise in a single measurement ω_{cp} or ω_{cf} is $\Delta\omega_{PN}$, which is about 100 kHz for the range of atom number and cavity detuning presented here. The challenge for spin squeezing via QND measurements is to make the noise $\Delta\omega_d$ low compared to $\Delta\omega_{PN}$. The ratio $R = (\Delta\omega_{PN}/\Delta\omega_d)^2$ is the spin noise reduction.

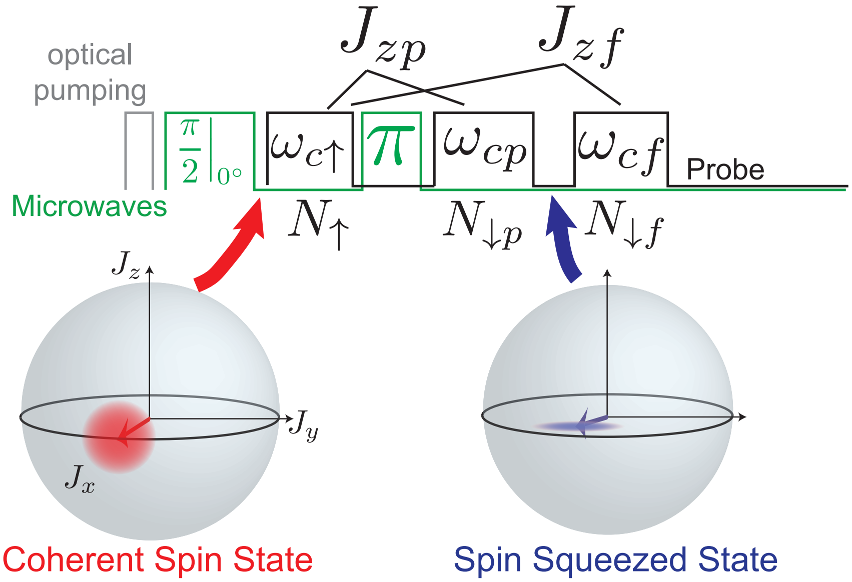

Figure 6.1: Spin squeezing measurement sequence and Bloch vectors representing the resulting states. Time goes from left to right. First, a CSS is prepared with optical pumping and a $\pi/2$ pulse. Then, the number of atoms $N_\uparrow$ in $|\uparrow\rangle$ is measured via the cavity shift $\omega_{\uparrow c}$. Next, a π-pulse is performed to swap the populations in $|\uparrow\rangle$ and $|\downarrow\rangle$ and $N_{\downarrow p}$ is measured. This generates a spin squeezed state. To verify the squeezing, $N_{\downarrow f}$ is measured soon after. The quantum projection noise ΔJ_{PN} cancels in the difference $J_{zf} - J_{zp}$.

6.2 Sources of Back-action

Probe-induced back-action in our QND scheme can cause signal loss or induce noise in J_z and ultimately limit the amount of spin squeezing we can generate. Here I discuss the sources of back-action in a QND measurement arising from fundamental and technical sources. The back-action can take the form of decreasing the signal $|\langle\hat{\mathbf{J}}\rangle|$ or causing extra noise in ΔJ_z. I discuss the fundamental back-action in the atomic spin projection and explain other sources of back-action (loss of signal and added noise) that are present in our QND measurement scheme.

6.2.1 Back-action: Loss of Signal

Free space scattering can cause loss of signal via single-atom collapse. When an atom emits into free space rather than the cavity, in principle it is possible to determine which atom emitted the photon. The information gained by the universe collapses the atom that scattered the photon into a definite spin state ($|\uparrow\rangle$ in the case of a Rayleigh transition and $|\downarrow\rangle$ in the case of a Raman spin-flip). This is equivalent to a loss of coherence or a shortening of the mean length of the collective Bloch vector. Because the phase resolution depends on the degree of coherence, $\Delta\theta = \Delta J_z/|\langle\hat{\mathbf{J}}\rangle|$, a loss of coherence directly translates to a reduction in phase sensitivity. We mitigate this effect in our system by increasing the coupling to the cavity with high optical depth or increasing NC, where $C = 4g^2/(\kappa\Gamma)$ is the single-atom cooperativity. This results in a decrease in the number of photons scattered (per atom) at a fixed number of probe photons.

Another significant contribution to the contrast loss is uncanceled inhomogeneous AC Stark shifts from the atomic-probe light. Because of inhomogeneous coupling g_i to the cavity for the ith atom, during the first probe window to determine $\omega_{\uparrow p}$ there is a significant amount of dephasing [41, 110]. However, the π-pulse in a real squeezing sequence between measurements $\omega_{\uparrow p}$ and ω_{cp} can spin-echo away the dephasing, yet not perfectly. This is because of fluctuations in the number of in-coupled photons in the two windows due to the atomic-probe/dressed cavity detuning being off-resonance. The result is a quadratic decrease in the contrast versus probe photon number since for small angular errors $\delta\phi_j$ in the azimuthal phase of individual atoms' Bloch vectors (assuming the average phase is aligned to $\phi = 0$), $\vec{J} = \sum_{j=0}^{N} g_j^2 \cos^2(\delta\phi_j) \approx \sum_{j=0}^{N} g_j^2 (1 - \delta\phi_j^2/2)$.

The final contribution to signal loss is from the anti-squeezing, which can lead to an effective shortening of the Bloch vector if ΔJ_y is comparable to $|\langle \hat{\mathbf{J}} \rangle|$. For large atom numbers, this effect is small since the contribution is only second order in ΔJ_y. For example, with $N = 10^6$ atoms, the azimuthal phase uncertainty $\Delta\phi_{SQL} = 1$ mrad so that with 20 dB of squeezing in $\Delta\theta$, the RMS size of the anti-squeezed quadrature would be $\Delta\phi_{AS} = 10$ mrad.

6.2.2 Back-action: Added Noise

There are several forms of noise that should become relevant as the probe photon number is increased and photon shot noise is averaged down. Noise in the cavity frequency measurement from atomic motion changing the coupling to the cavity, spin flip noise due to the optical cycling transition not being perfect, and opto-mechanical effects from spin-dependent motion are the major known sources of noise.

6.2.2.1 Noise from Atomic Motion

Radial atomic motion is an important contributor to the noise $\Delta\omega_d$. This is the current limitation to our spin noise reduction R at 17 dB and accounts for the apparently flat noise floor at high M_d. During the probing, the atoms are moving in the transverse radial direction with trap frequency $\omega_{rad} = 2\pi \times 800$ Hz. Also, the probe intensity is not uniform, with a 70 μm waist compared to the 15 μm RMS extent of the atom cloud in the optical lattice. The period of the transverse mode is much longer than the measurement time T_m, meaning the atoms can change their coupling to the probe mode g_i^2 between successive measurements to create noise in the cavity frequency measurement.

This is a very small effect compared to $\Delta\omega_{PN}$, but is a limitation here because our technical noise floor is a factor of 100 in variance below $(\Delta\omega_{PN})^2$. Assuming the atoms are in a thermal state, the motional added noise in $\Delta\omega_d$ scales with atom number like quantum projection noise.

Figure 6.9 shows the oscillatory behavior of this noise term. The two measurements ω_{cp} and ω_{cf}, each 40 μs long, are separated by a dark evolution time T_{evol}. The noise oscillates because at half period of the radial motion, the atoms have returned to their original positions.

If we were able to make the atoms colder, we could get closer to the technical noise floor and improve the squeezing beyond 17 dB. The noise in the cavity frequency measurement $(\Delta\omega_c)^{\mathrm{motion}} \propto T_{\mathrm{atoms}}/\sqrt{T_{\mathrm{trap}}}$, where T_{atoms} is the temperature of the atoms just before the first probing step and T_{trap} is the optical lattice depth (expressed as a temperature) just before the start of probing. Our system operates far from the fundamental recoil limit temperature of 400 nK, so there is room for improvement (assuming that we can overcome the limitations that the optical lattice puts on our ability to cool the atoms).

6.2.2.2 Raman Spin-Flip Noise

Raman spin-flips during the probing process can cause extra noise in the measurement of J_z. The spin-flip process is random and creates diffusion of J_z during probing. As atoms transition from $|\uparrow\rangle$ to $|\downarrow\rangle$, there is resulting randomness in the population difference $N_\uparrow - N_\downarrow$. This process is mitigated by the use of an optical cycling transition, where the probability of an atom in $|\uparrow\rangle$ to undergo a spin flip (per photon) can be $p < 10^{-2}$ in our system [16, 33].

6.2.2.3 Opto-Mechanical Motion

Finally, another possible source of noise is opto-mechanical motion of the atoms creating a noisy time-varying cavity frequency. This effect arises from the blue-detuned atomic probe light causing forces on the atoms by perturbing the confining potential, since the 780 nm probe light is incommensurate with the 823 nm trapping potential. The forces are strongest for atoms that have half the maximum coupling to the cavity because of the $\sin^2(kz)$ profile of the AC Stark shift created by the probe. As the atoms are pushed away from the probe intensity maxima, their effective g_i also decreases. Atomic motion then continues in a periodic manner due to the harmonic trap potential. While we do see opto-mechanics in the current iteration of the experiment, the noise it contributes is smaller than the radial atomic motion.

6.3 Measuring Atomic Populations with a Cavity

Now I discuss how to convert from atom number measurements to cavity frequency measurements, and associated noise. Atoms coupled homogeneously to an optical cavity create dressed cavity modes with resonance frequencies $\omega_\pm$ [146]

$$\omega_\pm = \frac{\delta_c \pm \sqrt{\delta_c^2 + \Omega_\uparrow^2}}{2}. \tag{6.3}$$

Here, $N_\uparrow$ atoms in $|\uparrow\rangle$ with collective coupling rate $\Omega_\uparrow = 2g\sqrt{N_\uparrow}$ and bare cavity detuning from atomic resonance $\delta_c = \omega_c - \omega_a$, and g is the coupling frequency at an anti-node of the probe. The classical description of this effect is the small single-particle phase shift imposed on the light by the atoms (due to having finite polarizability) being amplified by many round-trip passes. By very precisely measuring the dressed mode shift ω_+ with known detuning δ_c and cavity-atom coupling rate g, we can in principle invert this relationship to infer the atom number. The dressed mode frequencies $\omega_\pm$ from Equation 6.3 and bare cavity frequency ω_c are plotted in Figure 6.2 versus bare cavity detuning δ_c.

In our system, the atoms are inhomogeneously coupled to the cavity mode. To account for the effect of inhomogeneities, I use an effective coupling rate $g_{\text{eff}} = \sqrt{3/4}g$. The effective atom number $N_{\text{eff}} = (2/3)N_0$, where N_0 is the total number of atoms trapped in the lattice including the atoms not coupled to the cavity mode. These factors account for two effects in our standing-wave cavity: (1) the observed average cavity shift and (2) its fluctuation about the average [110, 32]. In other words, these factors consistently express the notion that atoms confined in the optical lattice do not contribute equally to the dressed cavity mode shift or quantum projection noise. This parametrization conveniently allows the same N to be used for calculating the noise and the mode shift in the presence of inhomogeneous coupling g_i for individual atoms. So, in Eqn. 6.3 and onward, g is understood to be g_{eff} so that $\Omega_\uparrow \to 2g_{\text{eff}}\sqrt{N_{\text{eff}}}$. Likewise, N is really N_{eff} where it appears outside of $\Omega_\uparrow$.

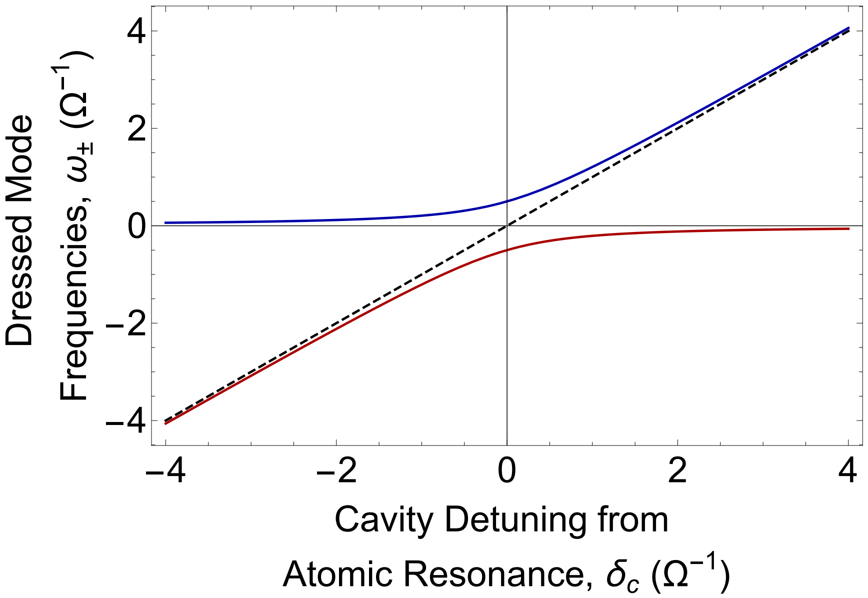

Figure 6.2: Dressed mode frequencies ω_+ (blue) and ω_- (red) and bare cavity frequency ω_c (black dashed line) versus bare cavity detuning δ_c. All the units are normalized in terms of the vacuum Rabi splitting Ω. Vertical axis offset is chosen so that $\omega_c = \delta_c$. Our experiment operates in the cross-over regime at $\delta_c \sim \Omega_\uparrow$.

To form the spin-1/2 system, we use the hyperfine ground states of ^{87}Rb defined by $|\uparrow\rangle \equiv \left|5^2S_{1/2}, F=2, m_F=2\right\rangle$ and $|\downarrow\rangle \equiv \left|5^2S_{1/2}, F=1, m_F=1\right\rangle$. The finesse $F = 2700$ optical cavity is set within 1 GHz of resonance of the $|\uparrow\rangle$ to $|e\rangle \equiv \left|5^2P_{3/2}, F'=3, m_f=3\right\rangle$ optical cycling transition at 780 nm. A magnetic field of 1 G in the z-direction breaks the degeneracy between magnetic sublevels and sets a quantization axis for the system.

The projection noise level or cavity frequency shift noise is set by the RMS atom number fluctuation of the CSS, $\Delta N_\uparrow = \sqrt{N/2}$. By linearizing the cavity shift at average atom number $\langle \hat{N}_\uparrow \rangle = N/2$, we can approximate the projection noise [33]

$$\Delta\omega_{\mathrm{PN}} = \frac{g}{2\sqrt{2}} \frac{\Omega_\uparrow}{\sqrt{\Omega_\uparrow^2 + \delta_c^2}}. \tag{6.4}$$

Notably, the projection noise variance $(\Delta\omega_{PN})^2$ scales as a Lorentzian, so for detunings $\delta_c \leq \Omega_\uparrow$ the noise level changes weakly with detuning δ_c. We can define the spin noise reduction parameter $R = (\Delta(\omega_{cf} - \omega_{cp})^2/(\Delta\omega_{PN})^2$.

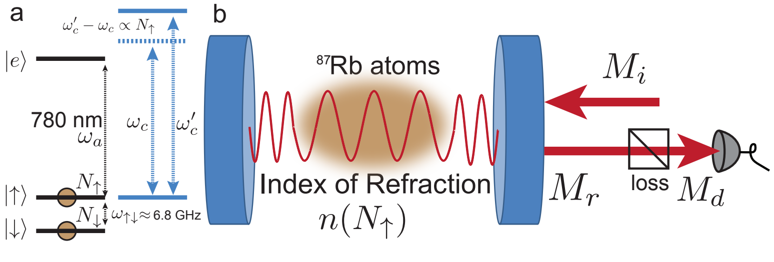

Figure 6.3: Schematic of the energy levels and cavity frequency and the effect of the atoms on the intracavity light. (a) A CSS with half the population in $|\uparrow\rangle$ and half in $|\downarrow\rangle$ (up to the projection noise level) forms the spin-1/2 system. The hyperfine splitting between the energy levels is approximately 6.834 GHz in ^{87}Rb. An optical cavity with bare resonance ω_c is shifted in the presence of atoms to dressed frequency ω_c' from the phase shift of the atoms. (b) The atoms confined in the optical lattice create a phase shift of the light due to their collective index of refraction that in general is a function of the number of atoms in $|\uparrow\rangle$, $n(N_\uparrow)$.

As the atom and cavity modes mix, the damping rate of excitations changes due to the exchange between atomic and photonic excitations. This can be expressed as a modified linewidth of the dressed cavity mode $\kappa \to \kappa'_\pm$ for the $\omega_\pm$ modes given by the weighted average

$$\kappa'_\pm = \frac{\kappa + \left(\frac{\Omega_\uparrow}{2\omega_\pm}\right)^2 \Gamma}{1 + \left(\frac{\Omega_\uparrow}{2\omega_\pm}\right)^2}. \tag{6.5}$$

This broadening affects the details of the cavity frequency measurement by changing the frequency-to-phase conversion factor as a function of cavity detuning and atom number, as discussed below.

6.4 Measuring Cavity Frequency Noise: Experimental Details

This section describes the measurement of cavity frequency that provides a collective measurement of spin populations. First, I outline how a measurement of the phase shift of light interacting with the dressed cavity mode can act as a low-noise measurement of the cavity frequency and therefore the atomic populations. Next, I discuss the details of the measurement, which allow for quantum projection noise a factor of 23 in variance below $(\Delta\theta_{SQL})^2$ [42].

6.4.1 Converting Phase Shifts to Frequency Measurements

Following the description of cavity-aided non-demolition measurements given in Refs. [33, 31], in this section I describe how our measurement of light phase in heterodyne gives us information about atomic populations. I try to provide some physical intuition and touch on some challenges we faced when setting up the measurement. The primary difference between the new cavity and the cavity used for prior experiments is the asymmetry between mirror transmission coefficients, while the length and radius of curvature of the mirrors is about the same as before.

A convenient description of the electric field of the laser that has interacted with the cavity is the phasor picture with quadrature amplitudes $I(t)$ (in-phase) and $Q(t)$ (out-of-phase) viewed in the frame of the laser frequency. The generalized response of the reflection quadratures as a function of laser detuning from the dressed cavity is

$$I_r = 1 - \sqrt{\frac{\kappa_1}{\kappa_2}} \frac{\mathcal{A}}{1 + \delta^{*2}} \tag{6.6}$$

$$Q_r = \sqrt{\frac{\kappa_1}{\kappa_2}} \frac{\mathcal{A}\delta^{*2}}{1 + \delta^{*2}}, \tag{6.7}$$

where $\delta^* = \delta_p/(\kappa'/2)$, κ' is the dressed cavity linewidth, δ_p is the atomic probe laser detuning from dressed cavity resonance, and the field amplitude parameter

$$\mathcal{A} = \frac{2\sqrt{\kappa_1\kappa_2}}{\kappa + \Gamma\left(\frac{\Omega_\uparrow}{2\omega}\right)^2}. \tag{6.8}$$

Here, $\kappa_1 = T_1 \times FSR = 2\pi \times 2.75$ MHz is the loss rate through the open mirror on the bottom of the cavity and $\kappa_2 = T_2 \times FSR = 2\pi \times 160$ kHz is the loss rate through the top closed mirror. The total bare cavity linewidth is $\kappa = \kappa_1 + \kappa_2 + \kappa_L$, where $\kappa_L = 2\pi \times 290$ kHz is the measured excess loss rate. These expressions include the effect of the atoms on impedance matching, i.e., the atoms cause light loss due to free space scattering. With just the bare cavity and no atoms, the expressions simplify to $\kappa' \to \kappa$ and $\mathcal{A} \to \frac{2\sqrt{\kappa_1\kappa_2}}{\kappa}$.

Practically, we extract the reflected quadratures I and Q in heterodyne detection, as first described in Chapter 3. The reflected phasors here are thus converted into time-varying voltage signals that can be analyzed in software.

To convert from the phase response of $\psi = \tan^{-1}(Q_r/I_r)$ into a cavity frequency f_c, we measure the slope of the phase response $d\psi/d\omega$. On each experimental trial, we introduce a small frequency offset $\pm\omega_{\mathrm{slp}}$ to the probe laser in both the red and blue directions to measure two phases ψ_+ and ψ_- (corresponding to blue and red frequency offsets, respectively). We then take the difference between the two phases divided by the optical frequency offset to estimate $d\psi/d\omega \approx (\psi_+ - \psi_-)/(2\omega_{\mathrm{slp}})$. This allows us to construct frequency measurements $\omega_c' - \omega_p = \psi/(d\psi/d\omega)$ in the near-resonant regime $\delta^* \ll \kappa'/2$ where ω_p is the frequency of the atomic-probe laser.

The quadrature response of the reflected light phasor versus detuning is shown in Figure 6.4. The range of values that the light phasor can attain is very different from the closed cavity ($\kappa_1 = \kappa, \kappa_2 = 0$) cases with no loss ($\kappa_L = 0$). In the closed cavity case, the phasor (I_r, Q_r) traces out a circle with radius 1 centered on the origin. The interpretation is that on resonance, all the light that gets into the cavity also ends up leaking back out the same mirror but with a π phase shift compared to the promptly reflected far off-resonance case.

Intra-cavity loss at rate κ_L reduces the size of the phasor since not all of the light coupled in finds its way out of the cavity. Imperfect mode-matching of the probe light to the cavity mode produces an extra in-phase offset in the I quadrature with normalized magnitude I_0. This DC offset just comes from having extra background light that did not couple into the cavity overlapping with the LO when it hits the photodetector—a mode mismatch between cavity mode and detection mode.

Imperfections due to loss or errors in mode-matching also modify the reflected phasor. Intracavity loss at rate κ_L reduces the size of the phasor since not all of the light coupled in finds its way out of the cavity. Also, imperfect coupling of the probe to the cavity mode will affect the center-point of the phasor, assuming the heterodyne LO is mode-matched perfectly to the probe. The extra light in the probe beam that did not interact with the cavity (because of imperfect mode-matching) adds a DC offset in the I quadrature of normalized magnitude I_0.

These modifications can provide experimental challenges by making the effective signal size on resonance (where we want to take data) close to the noise. If the magnitude of the phasor fluctuates through the zero, it means that the phase fluctuates from $[0, 2\pi)$, essentially an ambiguity in where the phasor is pointing. Since we use the phase ψ to establish the change in cavity frequency ω_c, it makes it very difficult to say what the frequency shift is.

For the results presented here, we avoided this ambiguity due to a DC offset in the I quadrature in two ways. First, we drove the cavity mode from the closed end with a strong beam to get a pure cavity mode coming out of hte detection mirror. We then coupled the cavity mode into a detection fiber, in the hope that a minimal amount of light in the probe beam that was not coupled to the cavity would make it to the detector. Also, we chose detunings δ_c where the loss due to free space scattering from atoms did not put the phasor near the origin on resonance.

6.4.2 Noise in the Cavity Frequency Measurement

The background noise level for measuring the cavity frequency, without the presence of atoms, is a function of the amount of power used to probe the cavity. Higher intensity corresponds to a higher rate of detected photons, with the phase variance of the light measurement scaling as

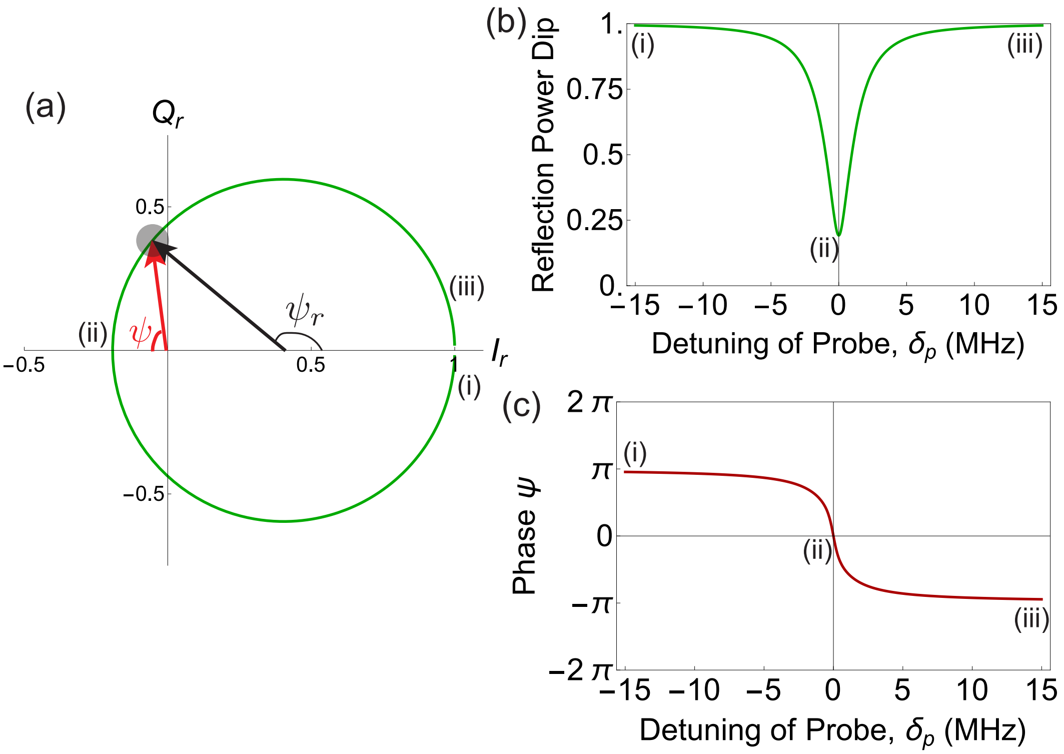

Figure 6.4: Diagram of the atomic probe phasor with measured cavity parameters and in the presence of $N_\uparrow = 200 \times 10^3$ atoms. (a) (Green) Circle in phase space traced out by the atomic probe cavity phasor as the detuning δ is changed from $-\infty$ to $+\infty$. The circle is offset from the origin owing to losses from the cavity κ_L, atoms, and the fact that it is not completely closed ($\kappa_2 \neq 0$). The black arrow represents the phasor of length $\mathcal{A}/2$ with phase ψ_r measured from the center of the circle that represents the normalized size of the light phasor. The gray blob represents photon shot noise. The phase $\psi = \tan^{-1}(Q_r/I_r)$ is the measured quantity. (b) Power reflection dip versus detuning of the probe δ_p. Note that unlike a perfect symmetric cavity, the reflection dip does not go to zero at $\delta_p = 0$. (c) Phase of reflected light $\psi = \tan^{-1}(Q_r/I_r)$, measured with respect to the I_r axis, versus probe detuning δ_p. Note that the peak-to-peak size is about 2π and not π.

$1/(2M_d)$ where M_d is the number of detected photons in a single measurement time window T_m. In terms of the number of photons M_i incident on the cavity, $M_d = q_d M_i$ where q_d is the detection quantum efficiency. Here, I have assumed that the cavity frequency measurement is a differential measurement between two windows with time spacing τ and symmetric length T_m. At high photon numbers, there is a technical noise floor set by the residual relative frequency noise between the cavity and the atomic probe. Part of this comes from finite gain in the atomic probe-to-cavity probe lock, but most comes from the technical noise floor of the cavity probe-to-science cavity PDH lock.

Successive measurements allow for cancellation of low-frequency noise when the difference is constructed. Low-frequency contributions are largely canceled by the differential measurement, with the primary contribution coming from frequencies close to $1/T_m$ or tens of kHz. In the presence of a spectral density of frequency fluctuations of the cavity S_ν, the resulting variance in a bare cavity measurement is $(\Delta f_d)^2 = \int_0^\infty S_\nu(f)T(f)df$. The transfer function is $T(f) = 4\sin^2(\pi f(T_m+\tau))\sin^2(\pi f T_m)/(\pi f T_m)^2$. The measured spectrum $S_\nu(f)$ due to technical noise in the heterodyne probing is shown in Figure 6.5(a), showing a reduction of a factor of 50 in the relative laser-cavity frequency noise that one would expect for a free-running ECDL laser with 200 kHz linewidth. Figure 6.5(b) shows the integrated (Δf_d) for the technical noise versus measurement time T_m with no gaps between the measurements, $\tau = 0$. The minimum at about 6 kHz corresponds to a noise variance of 24 dB below $(\Delta w_{PN})^2$.

An experimental sequence for the cavity frequency noise in the presence of atoms is the following: the atoms are cooled and loaded into the lattice, then optically pumped into $|\downarrow\rangle$. A $\pi/2$ pulse creates a CSS on the equator of the Bloch sphere. A “pre-centering” step with the atomic probe turned on puts the atomic probe on the dressed cavity resonance at which time the tuning is turned off. To mitigate the effects of optical pumping during the pre-centering step, the atoms are then re-optically pumped into $|\downarrow\rangle$ and another $\pi/2$-pulse is applied. Due to a small amount of atom loss, a constant frequency shift from the initial lock point is applied to the atomic probe (fluctuations in the atom loss are fairly small compared to κ). The atomic probe beam is once again turned on at a fixed power with total average number of incident photons M_i for a period

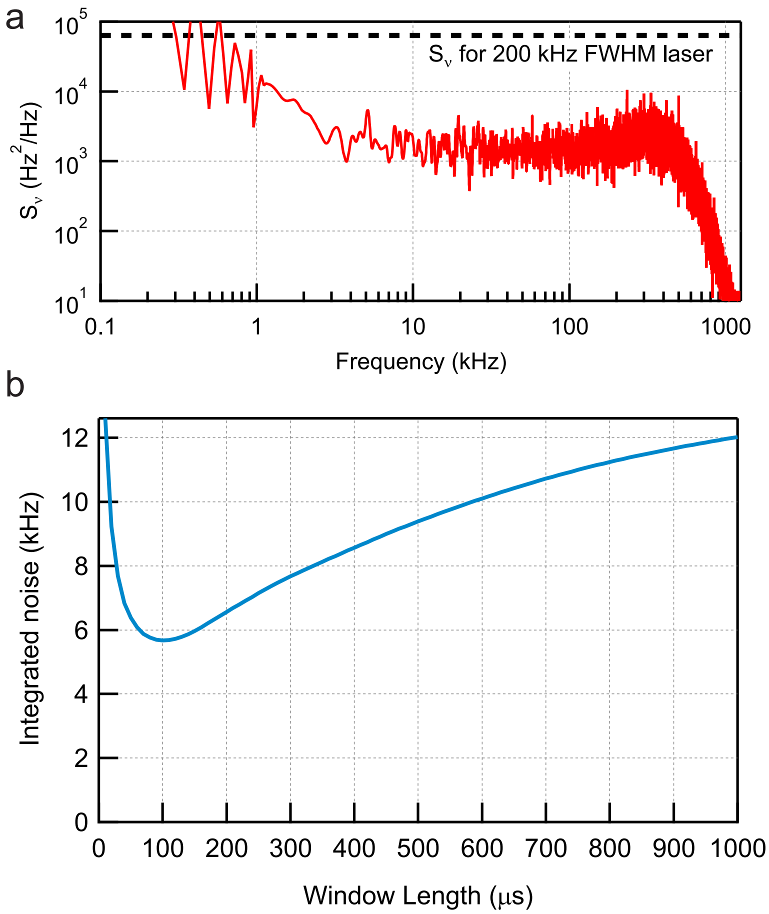

Figure 6.5: Power spectral density of frequency fluctuations $S_\nu(f)$ for the reflection signal of the atomic probe laser from the bare cavity and integrated noise as a function of measurement time T_m. (a) The measured power spectral density of instantaneous frequency fluctuations, $S_\nu(f)$, between the atomic-probe and an empty cavity. The frequency stabilization scheme reduces the noise by a factor of 50 compared to the expected S_ν for a free-running laser with 200 kHz FWHM Lorentzian linewidth. For this data, the atomic- and cavity-probe power was increased until the measured S_ν did not change, meaning technical noise was the dominant contribution over photon shot noise. The rise below 2 kHz corresponds to acoustic path length noise between the LO and the atomic-probe. (b) The integrated noise in the difference of two successive frequency measurements with the transfer function $T(f)$ using the spectrum for S_ν in (a) as a function of the measurement time T_m. The separation between windows was $\tau = 0$ for this calculation.

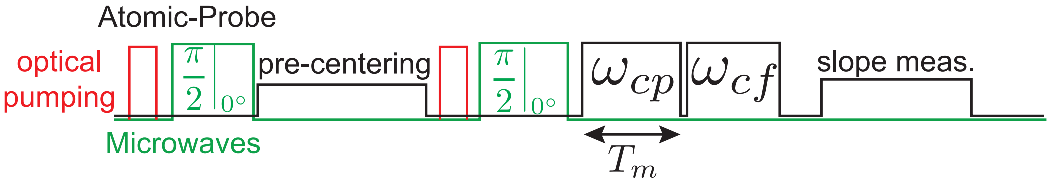

Figure 6.6: Timing diagram for an experimental sequence measuring the dressed cavity frequency. Time increases to the right. The black line represents the state of the atomic-probe laser (high is on, low is off). Green represents microwaves and red optical pumping. The atoms are initialized in a CSS and we perform a pre-centering step to bring ω_{pa} to ω_{ca}. The atoms are re-initialized and we probe the cavity frequency. Lastly, a slope measurement is performed by detuning the laser.

of 20 to 100 μs, performing the first measurement of ω_c. The probe beam is briefly turned off for the amount of time a π-pulse would take, and is turned on again and left on for 200 μs. At the end of the sequence, the atomic probe laser is shifted in frequency by ±100 kHz once again to get a measurement of the local slope of the phase curve.

To perform a low-noise measurement of the cavity frequency, we use high-bandwidth servos to stabilize the frequency of an atomic probe laser with frequency ω_{pa} to another cavity probe laser with frequency ω_{pc} that is stabilized to another longitudinal mode of the cavity many free spectral ranges away. The science cavity is meanwhile stabilized to an optical lattice laser at 823 nm. Even with an ECDL linewidth of 200 kHz, these $\approx$ 1 MHz bandwidth locks ensure that the cavity frequency noise not related to atomic projection noise is common-mode to the atomic probe laser and the cavity.

To stabilize the cavity probe laser, we Pound-Drever-Hall lock it to a longitudinal mode $\Delta n = 15$ orders away (in the red direction) from the longitudinal mode close to the $|\uparrow\rangle$ to $|i\rangle$ transition. We provide PDH sidebands by sending the cavity probe light through a free-space lithium niobate EOM crystal driven at 9.7 MHz and embedded in a parallel LC resonator that we drive inductively. The cavity probe signal is reflected from the cavity and detected on a reverse-biased avalanche photodiode. With a FSR of 8.090 GHz, this creates a frequency difference of approximately 122 GHz between ω_{ca} and ω_{cp}.

Having stabilized the cavity-probe laser, we offset beatnote lock the atomic-probe to the cavity-probe. We pick off light from the cavity probe and drive a fiber modulator (EOSPACE PN: PM-0S5-10-PFAPFA-780-UL) with low-noise 13.6 GHz microwave signal produced by frequency-doubled tooth of an RF frequency comb [35]. The resulting 9th order PM sideband is within 2 GHz of the dressed cavity mode frequency ω_{ca}.

The atomic probe laser is sent through an AOM at 82.5 MHz and an EOM at 137.5 MHz before it reaches the cavity. The blue PM sideband is then put on cavity resonance by tuning a DDS reference that sets the atomic probe-to-cavity probe beatnote lock. This puts a strong carrier beam 137.5 MHz from the cavity, but due to the finite cavity linewidth $\kappa \approx 2\pi \times 3$ MHz, a fraction of 10^{-4} of this carrier light leaks into the cavity off-resonantly. In practice, this does not cause much contrast loss due to free space scattering or uncancelled AC Stark shifts compared to the probe light that is directly on resonance with the cavity. The light in the atomic probe sideband that interacts with the cavity is detected in reflection by overlapping it with a LO beam derived from the atomic probe laser, at frequency offset 55 MHz. As in prior experiments, we used a custom circuit based on a reverse-biased S5973 photodiode connected to an AD8015 wideband transimpedance amplifier to generate a RF tone that is then sent to IQ demodulators so both quadratures of the phasor can be detected.

In order for both the cavity probe and the atomic probe to be able to reach the “open” mirror side of the cavity, they must be injected with orthogonal polarizations. To take advantage of the low back-action associated with the optical cycling transition, the atomic probe must be σ^+ polarized when it reaches the cavity. For polarization-selective separation to not contaminate the atomic probe and cavity probe signals with extra photon shot noise from each laser, the cavity probe is injected with σ^- polarization at the cavity. This is made possible by injecting the cavity-probe into the rejected port of an opto-isolator and detecting it off of another rejected port of a different opto-isolator. The breaking of time-reversal symmetry from the opto-isolator crystals makes this possible. Figure 6.7 shows the optical layout and frequency schemes for the two lasers.

There is still a small residual effect of the cavity probe on the contrast loss. Because of the large detuning of the cavity probe from atomic resonance, the dominant deleterious effect is an AC

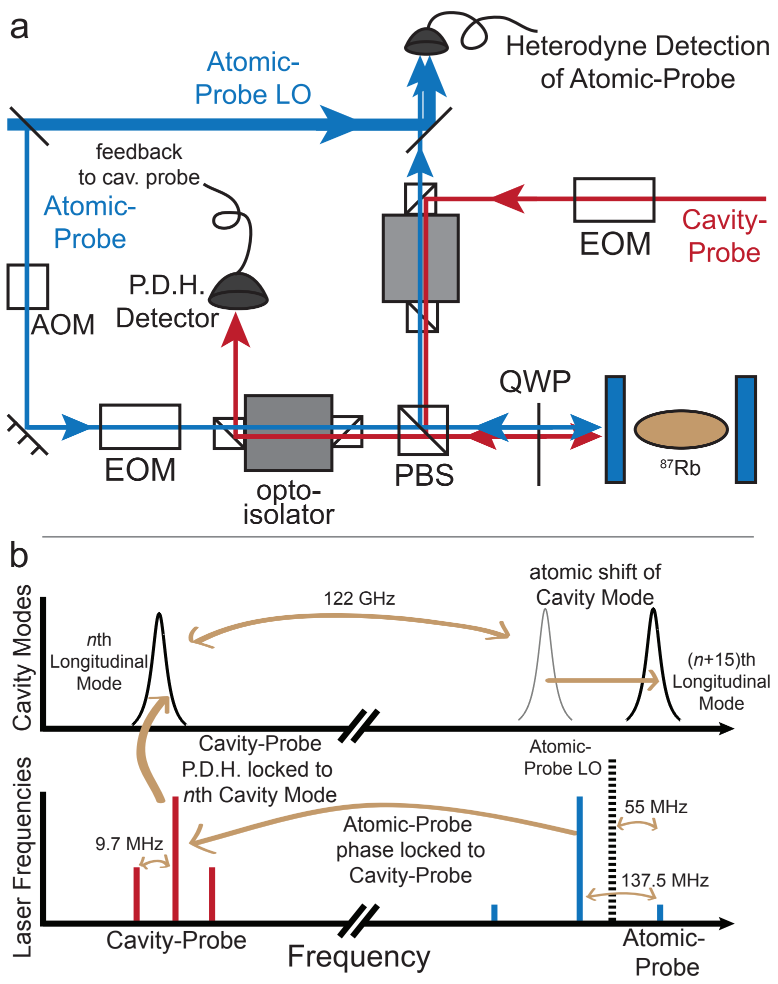

Figure 6.7: Diagram of the physical layout and laser frequencies for the atomic and cavity probe lasers. (a) Simplified optical setup for simultaneously probing two cavity modes to suppress relative laser-cavity frequency noise. The cavity-probe (red) is inserted and picked off through the rejected ports of opto-isolators that are set to transmit the atomic probe (blue). A quarter-wave plate near the cavity sets the polarization of the atomic probe to σ^+ and that of the cavity probe to σ^-. (b) Frequencies of the cavity modes and the probe lasers. The cavity probe is PDH locked to a different longitudinal TEM_{00} mode, which experiences a relatively small dispersive shift from the atoms. The atomic probe laser is phase-locked to the cavity probe for common mode rejection of cavity frequency noise not due to atoms, and is resonant with a cavity mode tuned close to resonance with an optical cycling transition. The dressed cavity mode is therefore sensitive to $N_\uparrow$. A LO beam with frequency offset 55 MHz from the atomic probe sideband that is resonant with the dressed cavity mode allows for heterodyne detection of the reflected light.

Stark shift (which scales as the inverse of detuning rather than off-resonant scattering scaling as the inverse of detuning squared). The APD is necessary for workable signal-to-noise on the PDH lock since the power in the cavity probe must be turned as low as possible to prevent extra background contrast loss. For total cavity-probe power less than 100 nW, the background contrast loss is a few percent.

Shot-to-shot variation in N of just a few percent causes fluctuations in f_c that are larger than κ'. Our probing scheme relies on the probe light being well within $\kappa/2$ of cavity resonance for a maximally sensitive phase measurement. To solve this cavity frequency fluctuation problem, we add in a "pre-centering" step at the beginning of an experimental sequence, when a CSS has been prepared along $\hat{x}$. We turn on the atomic-probe laser and square the heterodyne detector voltage $V(t)$ to generate a RF signal at the difference frequency of the atomic probe sideband (near resonance) and the atomic probe carrier (137.5 MHz away). We demodulate at the sum frequency of 137.5 MHz and low-pass filter to create a dispersive error signal, analogous to a Pound-Drever-Hall error signal. This error signal drives a loop filter whose output tunes "Digital VCO" made up of an ADC converter (Analog Devices AD9246) whose outputs program a real-time parallel programmable DDS chip (Analog Devices AD9910). This setup has the advantage of digital control, i.e., the DDS can hold its frequency depending on the value of a digital TTL input. The DDS provides the frequency LO reference for the atomic-probe to cavity-probe beatnote lock, closing the feedback loop.

The result is that the atomic probe can be driven quickly (within < 100 μs) to the dressed cavity resonance while causing little atom loss. Once the atomic probe reaches resonance, the probe is turned off and the atoms are re-prepared into a CSS. A constant frequency offset is applied to the atomic-probe laser by shifting the digital VCO output with a mixing stage with another DDS channel. This sets the laser close to the dressed cavity resonance after the re-preparation step, accounting for a small amount of atom loss between the pre-centering step and the first measurement window. Fluctuations in the final cavity frequency relative to the atomic-probe are much less than κ, which was the desired result of the pre-centering. A full measurement sequence for spin noise is shown in Figure 6.6.

A full list of cavity parameters is in Tables 3.1 and 3.2 of Chapter 3. The linewidth is $\kappa = 2\pi \times 3.05(5)$ MHz and the peak Jaynes-Cummings coupling constant for the $\left|5^2S_{1/2}, F = 2\right\rangle$ to $\left|5^2P_{3/2}, F' = 3\right\rangle$ cycling transition and at the anti-node of the probe is $g_0 = 2\pi \times 526$ kHz or $g_{\text{eff}} = 2\pi \times 456$ kHz. A typical atom number in the lattice is $N_{\text{eff}} = 2N_{\uparrow} = 4 \times 10^5$. A typical detuning is $\delta_c = +400$ MHz from the $|\uparrow\rangle$ to $|e\rangle$ transition. A simplified depiction of our cavity-aided probing scheme is illustrated in Figure 6.3. The number of photons in the atomic-probe laser incident on the cavity in a single measurement of ω_c is M_i. What we measure is the average number of photons detected, or M_d which is related to M_i through $M_d = qM_i$.

6.5 Spin Noise Reduction

The degree to which the noise in the cavity frequency measurement is reduced is the spin noise reduction. Figure 6.8 shows a spin noise reduction measurement sequence as well as data corresponding to individual runs of the experiment and simulated noise from QPN for comparison. The top shows a measurement sequence. Once a CSS on the equator of the Bloch sphere is prepared, the cavity frequency is probed two successive times with $T_m = 100$ μs with results labeled ω_{cp} and ω_{cf}. The difference $(\omega_{cp} - \omega_{cf})$ between the two measurements is displayed in units of the projection noise $\Delta\omega_{PN}$. On each trial, the process is deterministic but the process needs to be repeated many times for the statistical nature of the reduced noise to be apparent. For comparison, the red points are a result of a simulation of noise in a CSS for the same measurement conditions. Simulated data was used for the purposes of this illustration since excess classical noise in the initial $\pi/2$ pulse causes classical excess noise in the observed spin noise fluctuations when there is no differential measurement. The blue points show a partial cancellation of the quantum noise at the level of 50 times below un-squeezed atoms in units of the quantum noise variance by a factor of 50 relative to the quantum projection noise level.

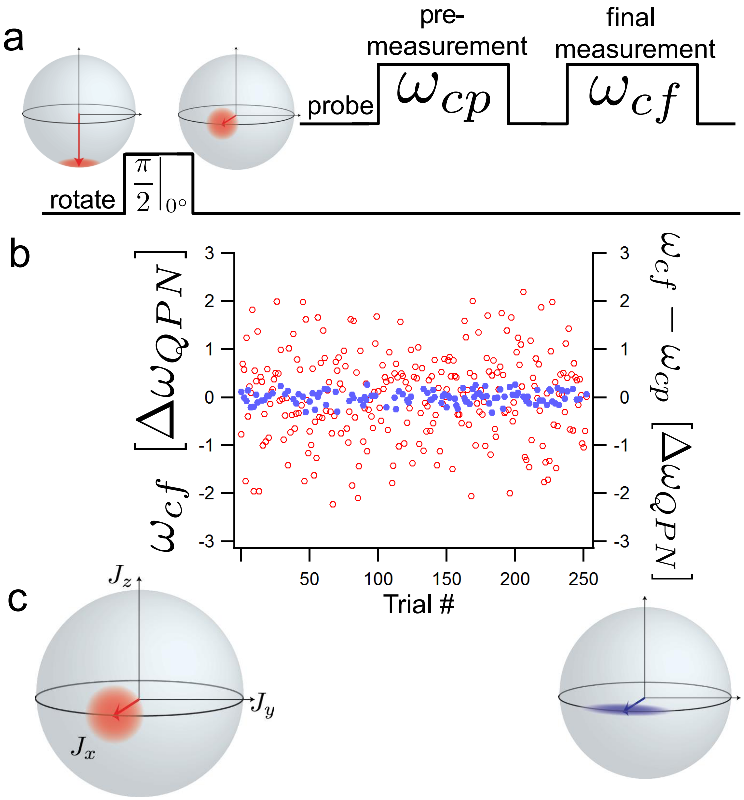

Figure 6.8: Measurement sequence for and demonstration of spin noise reduction. (a) Measurement sequence for probing the atoms. A coherent spin state is prepared by optically pumping all of the atoms into $|\downarrow\rangle$. Each atom is rotated into a superposition of $\frac{1}{\sqrt{2}}(|\uparrow\rangle + e^{i\phi}|\downarrow\rangle)$, corresponding to the total spin or Bloch vector oriented along the equator. Two consecutive measurements of the spin projection J_z are then performed (100 μs each) with the pre- and final-measurement outcomes for a single trial labeled J_{zp} and J_{zf}. The entire experimental sequence is then repeated many times. (b) Measurement outcomes versus trial number. Classical rotation noise in the $\pi/2$ pulse causes classical excess noise in the observed spin noise fluctuations, so here we display simulated Gaussian noise with rms distribution equal to the predicted projection noise level fluctuations $\Delta\omega_{PN}$ (left axis, red open circles). The measured differential quantity $\omega_{cf} - \omega_{cp}$ (blue, right axis) shows partial cancellation of both the quantum projection noise and the excess classical noise. The differential quantity's noise variance is 50 times below the projection noise level (or 17(1) dB). (c) (left) The red data can be visualized as arising from a fundamental blurriness of the orientation of the collective Bloch vector. (right) The measurement process projects the collective atomic state into a squeezed state with reduced uncertainty in the polar angle, at the expense of increase uncertainty in the azimuthal angle.

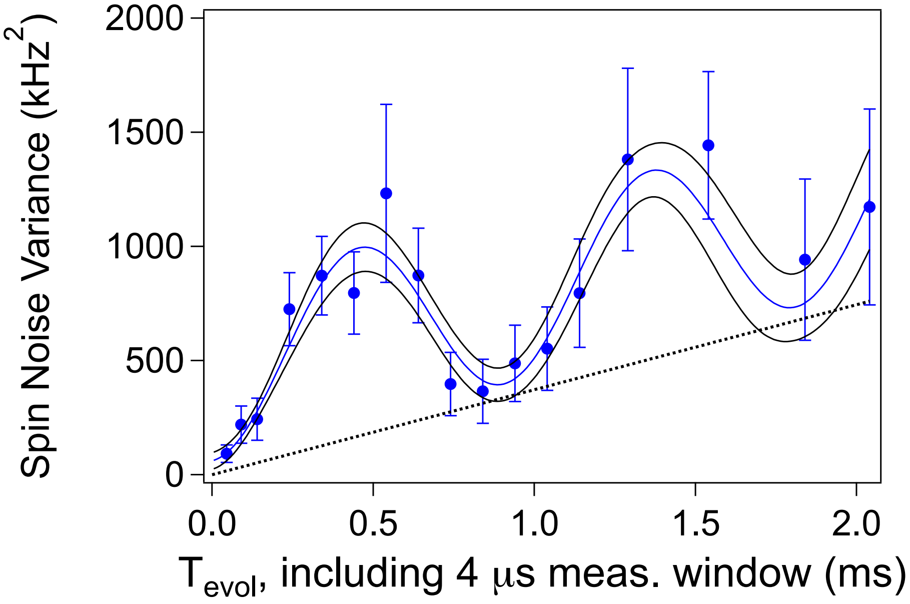

Figure 6.9: Apparent spin noise from radial motion of atoms versus time. The vertical axis is the spin noise variance in kHz^2, and the horizontal axis is the sum of the time between the measurement windows T_{evol} and the measurement window length T_m. The blue line is a fit to a sinusoidal model including linear increase and constant offset terms. The linear term (black dashed line) is shown for reference. The points at low time correspond to about 17 dB of spin noise reduction. The frequency of the oscillations agrees well with the expected radial frequency of motion of about 500 Hz for the trap depth used in the experiment.

6.6 Measured Loss of Signal

Preserving the signal is crucial for having useful coherence left over that can be used in a precision measurement. Without a "clock hand" of a collective Bloch vector remaining, the atomic ensemble is incoherent and cannot be used for interferometry. There is a trade-off for probing with a greater number of photons: a reduction in signal, as discussed in Section 6.2.1.

The fundamental source of signal or contrast loss in our system is free space scattering. The ratio NC of forward scattering into the cavity to free space scattering can be made on the order of 10^3 in our system, but there is still finite coupling to free space modes. The scattering rate into free space in the far-detuned limit $\delta_c \gg \Omega_\uparrow$ scales as $1/\delta_c^2$. At the same time, the cavity shift signal decreases as δ_c meaning that to resolve the same frequency shift of the cavity, more photons need to be sent through the cavity $\propto \delta_c^2$ to maintain the signal-to-noise in variance. However, there is always a fixed technical background underlying the photon shot noise level, so there is a net loss in signal-to-noise with ever-increasing detuning. So, detuning farther away from atomic resonance does not enhance the non-destructive quality of the measurement.

We measure the atomic coherence by performing contrast measurements using a spin-echo Ramsey experiment. The measurement sequence starts with a $\pi/2$ pulse followed by a measurement window of length T_m and detected photon number M_d, then a π-pulse, a second measurement window (with same T_m and M_d), and final $\pi/2$ pulse with variable LO phase. This maps out a sinusoidal fringe of cavity frequency shift versus the phase of the final $\pi/2$-pulse. This pulse sequence is illustrated at the top of Figure 6.10. The fringe amplitude is normalized to the no-photon case ($M_d = 0$), which represents the initial contrast $\mathcal{C}_i$.

Figure 6.10 shows two example contrast curves for $N = 250 \times 10^3$ atoms and $\delta_c = 500$ MHz. The atoms are probed twice with a single-window detected photon number $M_d = 0$ (black data set) and $M_d = 17.7 \times 10^3$ (red data set) in a measurement time $T_m = 40$ μs. The extra scatter in the red data corresponds to a fluctuating average AC Stark shift between trials due to fluctuations of intra-cavity photon number. These fluctuations can arise from pulse errors in both the $\pi/2$ and

π-pulses causing the dressed cavity frequency center to be off resonance with the atomic-probe. Pulse errors result in the dressed cavity frequency shifts differing more than projection noise and changing the amount of in-coupled light. There is incomplete cancellation of the AC Stark shift between windows, due to the π-pulse leading to an average uncancelled phase shift of the Bloch vector.

We then analyze the reduction in size of the contrast fringe versus probe strength, characterized by M_d. A model $\exp(-aM_d - bM_d^2)$ is fit to the data to account for free-space scattering (the exponential term, coefficient a) and uncanceled inhomogeneous AC Stark shifts (the Gaussian term, coefficient b). Figure 6.11(a) shows an example of a fit to the contrast versus number of detected photons in one measurement window M_d, with the bare cavity detuning $\delta_c = 2000$ MHz. In this data, corresponding to the far-right point in Fig. 6.11(b), the quadratic term is dominant.

Given a certain number of detected photons M_d, the ratio of scattered photons to detected photons R_s is

$$R_s = \frac{1}{q_d \eta_s} \frac{\Gamma}{\kappa} \frac{\Omega_\uparrow^2}{4\omega_c^2}. \tag{6.9}$$

The contrast $\mathcal{C}_f$ after probing if there are no other sources of signal loss is given by $\mathcal{C}_f = \mathcal{C}_i e^{-\frac{2R_s}{N} M_d}$, where $\mathcal{C}_i$ is the initial contrast before the measurement sequence. The term $m_s = \frac{2R_s}{N} M_d$ represents the number of free space scattered photons per atom after two measurement windows each with detected photon number M_d. Figure 6.11 shows the no-free-parameter prediction for R_s and our measured exponential loss factor versus detuning, given our measured quantum efficiency for detection $q_d = 41\%$.

The fit parameters a are plotted versus δ_c in Figure 6.11(b), along with a prediction line for the coefficient $2R_s/N$, where the factor of 2 accounts for the two measurement windows since we define M_d to be the number of photons in a single measurement window. The prediction line was generated by using the measured quantum efficiencies in the detection path to estimate the number of photons that actually interacted with the atoms. Although the fractional error on the values of a are somewhat large, we see reasonable agreement with the prediction curve, giving us some

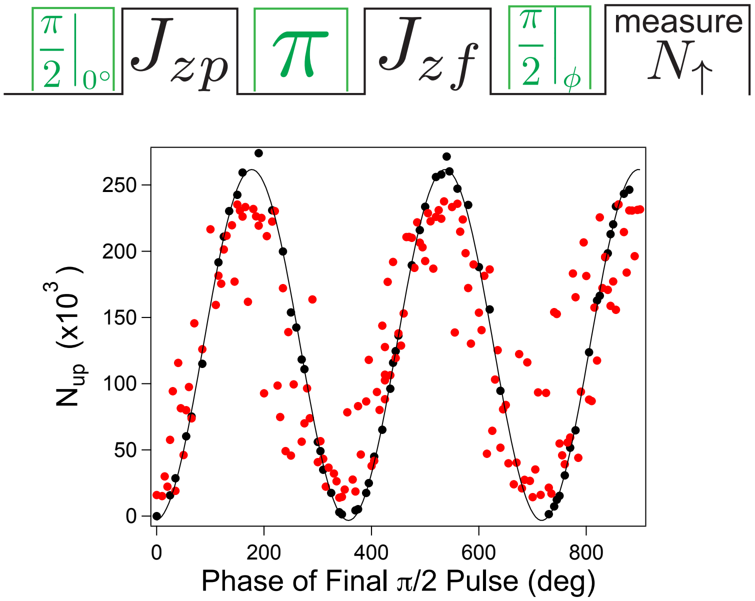

Figure 6.10: Measurement sequence and Ramsey spin-echo contrast fringe for $\delta_c = 500$ MHz and $N = 250 \times 10^3$ atoms. (Top) Measurement sequence showing microwave pulses in green and cavity probing in black. Following an initial $\pi/2$ pulse, one measurement is performed and then a spin-echo π pulse is applied before a second measurement sequence. Finally, a $\pi/2$ readout pulse is performed. (bottom) Plot of contrast versus phase of the final $\pi/2$. Black points correspond to $M_d = 0$, red points to $M_d = 17.7 \times 10^3$ with measurement windows $T_m = 40$ μs separated by the π-pulse time of 15 μs. The black line is a sinusoidal fit to the black points, with frequency held fixed. Scatter in the red data at high photon number comes from fluctuations in the average AC Stark shift between the two measurement windows due to fluctuations in the in-coupled power.

confidence that with proper tuning of the system we ought to be able to realize the fundamental quantum limit for contrast for low photon numbers $M_d < 2 \times 10^4$ and low detunings $\delta_c < 1$ GHz, where the quadratic contribution is not large. The large error bars likely come from coupling to the quadratic parameter b (not shown here) in the presence of a finite amount of data points for each contrast versus M_d curve.

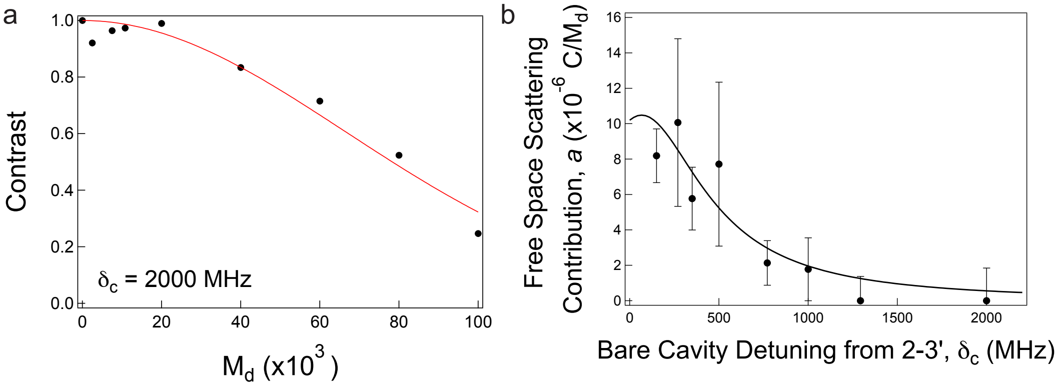

Figure 6.11: Contrast versus detected photon number M_d and contrast loss from scattering versus bare cavity detuning δ_c. (a) Contrast versus single-window detected photon number M_d at detuning $\delta_c = 2000$ MHz. The contrast data (black points) is normalized to the amplitude of the fringe in the dark measurement with $M_d = 0$. The red line is a fit to a model including a product of exponential and Gaussian terms. For the data shown here, the Gaussian term from uncanceled AC Stark shifts is dominant. (b) Contrast loss parameter from free space scattering a versus bare cavity detuning from the optically excited state, δ_c. Points correspond to the value of a from fits to contrast curves like in (a). The black line shows a prediction based on measured quantum efficiency $q_d = 41\%$, atom number N (varies between points), and cavity parameters.

We see that we can realize for most detunings a reduction in contrast at low probe photon number that agrees fairly well with the prediction. The free space scattering limit represents the minimum contrast loss for our system given the fixed cavity parameters. By increasing the quantum efficiency of detection, we can improve the contrast by sending through fewer photons while still realizing a fixed frequency measurement noise Δf_d.

6.7 Prospects for Spin Squeezing

Combining our measurements of spin noise reduction R and contrast loss, we can understand the limits to our current technique. The full spin squeezing sequence of Figure 6.1 was not used for the lowest spin-noise data. Instead of measuring $N_\uparrow$ before a π-pulse and the two successive measurements of $N_\downarrow$, the sequence of Figure 6.8 was used. This is suitable for characterizing the noise, but does not represent squeezing. We expect, however, that technical challenges associated with pulse tuning will not significantly impact our ability to generate spin squeezed states when we take data in the squeezing configuration of Figure 6.1 including all three cavity frequency measurements and an additional π-pulse.

Figure 6.12 shows spin noise reduction R and contrast loss $\mathcal{C}_f^2$, as well as the degree of squeezing accounting for the reduction in noise versus the reduction in atomic coherence. The black points are the spin noise reduction for a dataset with $\delta_c = 500$ MHz and $N_{\text{eff}} = 400 \times 10^3$, with 100 μs measurement windows. Notably, there appears to be a flat noise floor in the spin noise reduction at about 17 dB below the SQL. We believe this represents decorrelation between the two measurements due to radial motion of the atoms in the optical trap between the two measurement windows, as shown in Figure 6.9. The black line represents a fit to the PSN scaling plus the technical background noise offset. As M_d increases, the noise decreases until it hits the floor associated with radial motion. Here I note that we do not yet see either quantum (spin-flip) or classical back-action, which would correspond to an increase in R at high M_d.

The contrast $\mathcal{C}_f^2$ is also shown. Metrologically relevant contrast loss is really $\mathcal{C}_f^2/\mathcal{C}_i$ [135], but here we have taken $\mathcal{C}_i = 1$ to estimate the worst-case scenario. An exponential multiplied by gaussian fit and corresponding 68% confidence level is represented by the solid blue curve and shaded region. At short times, exponential contrast loss dominates but at long times the Gaussian decay from uncanceled AC Stark shifts dominates.

Multiplying the two curves together gives the expected amount of squeezing, or red line, with a minimum of -13.7(1.0) dB or a factor of 23(5) enhancement in quantum phase estimation.

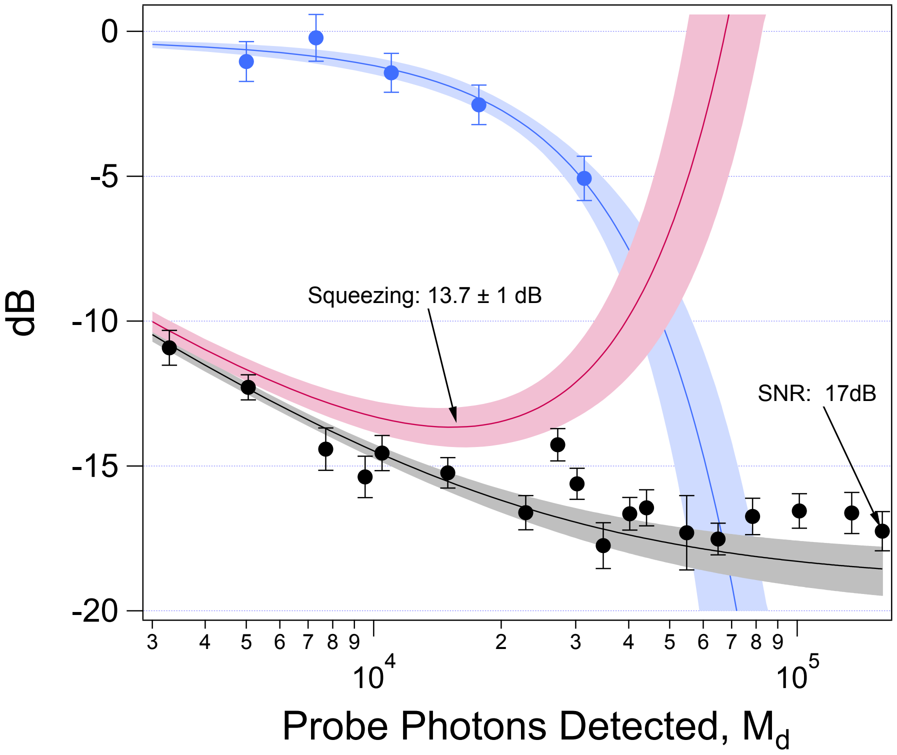

Figure 6.12: Spin noise reduction, contrast loss, and expected squeezing versus M_d in one 100 μs window. Vertical axis is on a dB scale, and horizontal axis is on a log scale. Bare cavity detuning $\delta_c = 500$ MHz, and $N_{\text{eff}} = 400 \times 10^3$. The black points are the measured spin noise reduction with statistical error bars. The black solid line is a fit to a photon shot noise scaling with a constant noise background added in quadrature. The gray fill represents the uncertainty (68% CL) in the fit. Blue points are relative contrast data for similar parameters, but not taken at the same time as the spin noise reduction. The solid blue line is a fit with a model including both exponential and Gaussian terms to include the effects of both free space scattering and residual dephasing that is not spin-echoed away. The red curve represents the expected squeezing through taking the product of the black and blue curves. Its minimum occurs at -13.7(1.0) dB or an enhancement in variance of a factor of 23(5).

I note that this would correspond to a directly observed amount of squeezing without subtraction of technical background noise—an important point, since this is the true amount of squeezing that would be applicable in a precision measurement. For reference, the previous result at 10 dB [16] was already the highest absolute degree of phase enhancement reported in the literature without subtraction of technical noise floor. The most squeezing reported to date is 12.3 dB of quadrature squeezing in light [91].

6.8 Outlook

This work represents a third generation of spin squeezing experiments by our group. Our preliminary results are very encouraging, since straightforward technical improvements ought to only improve the spin noise reduction at low M_d.

Chiefly, the effective quantum efficiency of the detection system has room for improvement. This work was done using heterodyne detection, which has in principle a factor of 2 more photon shot noise than a homodyne measurement, in which the detection LO beam is frequency degenerate with the atomic probe. By using path length stabilization combined with a low-noise balanced homodyne scheme, the spin noise in the PSN-limited regime ought to be improved by 3 dB. Also, straightforward increases in real path efficiency through elimination of non-critical fiber-coupling steps should give at least a factor of 13% in increased quantum efficiency. In the near term, then, a phase enhancement of 17 dB is quite feasible, and steps are currently underway to achieve that extra factor of 2 (i.e., 3 dB).

Chapter 7

Summary and Conclusion

7.1 Summary of Results

This thesis emphasized the role of coherence-preserving interactions between atoms for creating sensors and exploring synchronization, in both steady state superradiance in a Raman system and cavity-aided spin squeezing.

In Chapter 4 I presented a proof-of-principle vector magnetometer based on steady state superradiance in a Raman system. The best sensitivity was 190 $\mathrm{pT}/\sqrt{\mathrm{Hz}}$ at 1 kHz in a broadband, active sensing mode during continuous superradiant emission. The fundamental sensitivity of the magnetometer was not achieved here but was theoretically estimated to be set by phase diffusion noise at low frequencies and photon shot noise at high frequencies. A sensing scheme based on dark evolution, analogous to a Ramsey sequence, was also experimentally demonstrated and shown to exceed the broadband sensitivity (limited by photon shot noise) at 36 kHz. The expected scaling of the signal due to coherent π-pulse manipulations in a Carr-Purcell-Meiboom-Gill-like sequence [92] was also shown to agree with the measured value. This sensor represents the potential of controlled steady state superradiance for creating versatile sensors in which the superradiant process continuously re-establishes coherence while allowing non-destructive probing of the coherence.

The behavior of coupled superradiant lasers operating within the same cavity mode was explored theoretically (building on the concepts introduced in Chapter 2) and experimentally in Chapter 5. A discussion of the underlying synchronization mechanism was discussed and the role of dissipation in creating synchronization, and may enable observation of quantum behavior in synchronization processes. The steady state response of the two lasers with natural frequencies ω_a and ω_b to changing detuning $\delta = \omega_a - \omega_b$ was investigated both theoretically (using an extension of the concepts introduced in Chapter 2) and experimentally. The coupled superradiant lasers underwent a transition from unsynchronized behavior at high δ to synchronized below a critical detuning $|\delta| < W$, where both ensembles a and b emitted light at a common frequency despite having different natural frequencies ω_a and ω_b. In the time domain, the capacity of the superradiant laser to heal phase errors was experimentally shown to agree with both a simple theoretical model and a full numerical simulation. This work points toward multiple superradiant ensembles as a platform for exploring phase synchronization models in open quantum systems. Also, using multiple superradiant ensembles to reduce the impact of systematic errors (e.g., operating two lasers with opposite frequency sensitivity to magnetic fields) in future technologically relevant implementations for narrow-linewidth phase references.

Lastly, in Chapter 6 I described a next generation of spin squeezing experiments made possible through technical improvements to the experimental apparatus, culminating in 13.7 dB of possible enhancement in phase resolution. Previously, due to low quantum efficiency and excess technical noise, the squeezing was limited to 10.2(6) dB [16]. Both the effects of reduced measurement noise and signal loss were discussed, including the dominant effects of back-action in signal loss and excess noise from atomic motion that currently limit the expected squeezing. We expect that this is far from the most squeezing we can achieve in the current generation of the experiment. Straightforward extensions of this technique promise even more gain in spectroscopic enhancement, showing cavity-aided QND measurements as a very promising route for generating a practically useful amount of spin squeezing.

During the preparation of this thesis, more improvements to the experimental apparatus were implemented by Kevin Cox and Graham Greve. Most importantly, the substitution of a balanced homodyne detection scheme for the heterodyne scheme presented here increased the effective quantum efficiency of detection by about 3 dB, translating to a direct 3 dB in spin noise reduction. Preliminary explorations indicate that 17 dB of spin squeezing is feasible. To our knowledge, 17 dB of spin squeezing would represent a higher degree of spectroscopic enhancement via entanglement than has been reported in any quantum system.

7.2 Future Directions

Given the current state of the apparatus, there are some promising routes for exploring spin squeezing. The optical cavity and detection system is highly optimized for measuring cavity frequency shifts with low technical noise, so generating a higher level of spin squeezing and showing the feasibility of atom interferometry aided by spin squeezing are natural progressions

As discussed in Chapter 6, cavity frequency noise arising from radial atomic motion in the optical trap is the dominant noise contribution at high probe photon number. If we were able to make the atoms colder, we could get closer to the technical noise floor and improve the squeezing beyond 17 dB. The noise in the cavity frequency measurement $(\Delta\omega_c)^2_{\text{motion}} \propto T^2_{\text{atoms}}$, where T_{atoms} is the temperature of the atoms just before the first probing step. We have as yet been unable to identify the mechanism limiting our final temperature at high lattice depths and investigations into better cooling are ongoing.

Another direction is preparing homogeneously coupled ensembles appropriate for use in atom interferometers. Since the standing wave of our optical lattice (823 nm) is incommensurate with the probe mode standing wave (780 nm), our system has inhomogeneous probe coupling with $g^2(z) = g_0^2 \cos^2(kz)$ where the wavenumber $k = 2\pi/\lambda$ for a wavelength of light λ and z is the location along the cavity axis. We could generate an effective homogeneous coupling by allowing the atoms to move in the axial direction, so they average their coupling within a measurement window by moving several spatial periods $\lambda/2$. At a temperature of 40 μK (where our experiment commonly operates), the ^{87}Rb atoms would move λ in about 1 μs. As discussed in Chapter 6, typical measurement times $T_m = 40$ μs can generate > 10 dB, ensuring good averaging of the axial coupling for individual atoms. Once the homogeneously squeezed ensemble has been created, it could be released into a free-space atom interferometry experiment [12] or could be used in a cavity-aided atom interferometer [55].

We can allow the atoms to move in the axial direction by creating an effective optical dipole trap composed of out-of-phase optical lattices. One scheme for generating an intra-cavity optical dipole trap in the axial direction is to drive adjacent longitudinal cavity modes with sidebands of the lattice laser. This works in the following way: If the nth cavity mode has an electric field profile $\propto \cos(k_1 z)\cos(\omega_1 t)$ near the center of the cavity, the $(n+1)$ cavity mode has a $\sin(k_2 z)\cos(\omega_2 t)$ field. Here, $\{k_1, k_2\}$ and $\{\omega_1, \omega_2\}$ are the slightly different wavenumbers and angular frequencies separated by the free spectral range of the cavity. Near the center of the cavity, the intensity profile has $\sin^2(k_2 z)\cos^2(\omega_2 t)$ and $\cos^2(k_1 z)\cos^2(\omega_1 t)$ terms and cross-terms $\cos(\Delta k z)\cos(\Delta\omega t)$ and $\cos((2k_1 + \Delta k)z)\cos((2\omega_1 + \Delta\omega)t)$, where $\Delta\omega = \omega_2 - \omega_1$ and $\Delta k = k_2 - k_1$. The frequency of oscillation of the cross-terms are $2\omega_1 + \Delta\omega \gg \Delta\omega = 2\pi \times FSR$, where $FSR = 8$ GHz. The time-average gives DC contributions $\cos^2(k_1 z)$ and $\sin^2(k_2 z)$, while the cross-terms should average to zero on the timescales of atomic motion. This ought to result in a smooth potential with no axial confinement, allowing z-translation symmetry in time-averaged coupling.

In the long run, our "quantum playground" could explore other physics like entangled states generated by optical pumping [46] or exploring quantum phase transitions in the Dicke model [49, 10]. Still further on the horizon are experiments in a ring cavity (with intrinsic homogeneous coupling) that could support multiple well-separated atomic ensembles for generating entanglement between distant and separately-addressable atoms.

Bibliography

[1] J Aasi, J Abadie, BP Abbott, R Abbott, TD Abbott, MR Abernathy, C Adams, T Adams, P Addesso, RX Adhikari, et al. Enhanced sensitivity of the ligo gravitational wave detector by using squeezed states of light. Nature Photonics, 7(8):613–619, 2013.

[2] Juan A. Acebrón, L. L. Bonilla, Conrad J. Pérez Vicente, Félix Ritort, and Renato Spigler. The kuramoto model: A simple paradigm for synchronization phenomena. Rev. Mod. Phys., 77:137–185, Apr 2005.

[3] J. Appel, P. J. Windpassinger, D. Oblak, U. B. Hoff, N. Kjrgaard, and E. S. Polzik. Mesoscopic atomic entanglement for precision measurements beyond the standard quantum limit. Proceedings of the National Academy of Sciences, 106(27):10960–10965, 2009.

[4] FT Arecchi, Eric Courtens, Robert Gilmore, and Harry Thomas. Atomic coherent states in quantum optics. Physical Review A, 6(6):2211, 1972.

[5] Markus Aspelmeyer, Tobias J. Kippenberg, and Florian Marquardt. Cavity optomechanics. Rev. Mod. Phys., 86:1391–1452, Dec 2014.

[6] Mahmood Bagheri, Menno Poot, Linran Fan, Florian Marquardt, and Hong X. Tang. Photonic Cavity Synchronization of Nanomechanical Oscillators. Phys. Rev. Lett., 111(21):213902, November 2013.

[7] C A Baker, S N Balashov, V Francis, K Green, M G D van der Grinten, P S Iaydjiev, S N Ivanov, A Khazov, M A H Tucker, D L Wark, A Davidson, J R Grozier, M Hardiman, P G Harris, J R Karamath, K Katsika, J M Pendlebury, S J M Peeters, D B Shiers, P N Smith, C M Townsley, I Wardell, C Clarke, S Henry, H Kraus, M McCann, P Geltenbort, and H Yoshiki. Cryoedm: a cryogenic experiment to measure the neutron electric dipole moment. Journal of Physics: Conference Series, 251(1):012055, 2010.

[8] Ben Q. Baragiola, Leigh M. Norris, Enrique Montaño, Pascal G. Mickelson, Poul S. Jessen, and Ivan H. Deutsch. Three-dimensional light-matter interface for collective spin squeezing in atomic ensembles. Phys. Rev. A, 89:033850, Mar 2014.

[9] Jacob Baron, Wesley C Campbell, David DeMille, John M Doyle, Gerald Gabrielse, Yulia V Gurevich, Paul W Hess, Nicholas R Hutzler, Emil Kirilov, Ivan Kozyryev, et al. Order of magnitude smaller limit on the electric dipole moment of the electron. Science, 343(6168):269–272, 2014.

[10] Kristian Baumann, Christine Guerlin, Ferdinand Brennecke, and Tilman Esslinger. Dicke quantum phase transition with a superfluid gas in an optical cavity. Nature, 464(7293):1301–1306, April 2010.

[11] Matthew Bennett, Michael F. Schatz, Heidi Rockwood, and Kurt Wiesenfeld. Huygens's clocks. Proceedings of the Royal Society of London A: Mathematical, Physical and Engineering Sciences, 458(2019):563–579, 2002.

[12] S Bernon, T Vanderbruggen, R Kohlhaas, A Bertoldi, A Landragin, and P Bouyer. Heterodyne non-demolition measurements on cold atomic samples: towards the preparation of non-classical states for atom interferometry. New Journal of Physics, 13(6):065021, 2011.

[13] Adam T. Black, James K. Thompson, and Vladan Vuletić. On-demand superradiant conversion of atomic spin gratings into single photons with high efficiency. Phys. Rev. Lett., 95:133601, Sep 2005.

[14] Eric D Black. An introduction to pound–drever–hall laser frequency stabilization. American Journal of Physics, 69(1):79–87, 2001.

[15] B J Bloom, T L Nicholson, J R Williams, S L Campbell, M Bishof, X Zhang, W Zhang, S L Bromley, and J Ye. An optical lattice clock with accuracy and stability at the 10-18 level. Nature, 506(7486):71–75, February 2014.

[16] J. G. Bohnet, K. C. Cox, M. A. Norcia, J. M. Weiner, Z. Chen, and J. K. Thompson. Reduced spin measurement back-action for a phase sensitivity ten times beyond the standard quantum limit. Nature Photonics, 8(9):731–736, 09 2014.

[17] Justin G Bohnet. A Superradiant Laser and Spin Squeezed States : Collective Phenomena in a Rubidium Cavity QED System for Enhancing Precision Measurements. PhD thesis, University of Colorado Boulder, 2014.

[18] Justin G. Bohnet, Zilong Chen, Joshua M. Weiner, Kevin C. Cox, Dominic Meiser, Murray J. Holland, and James K. Thompson. A quasi-continuous superradiant raman laser with ¡ 1 intracavity photon. EPJ Web of Conferences, 57:03003, 2013.

[19] Justin G. Bohnet, Zilong Chen, Joshua M. Weiner, Kevin C. Cox, and James K. Thompson. Relaxation oscillations, stability, and cavity feedback in a superradiant raman laser. Phys. Rev. Lett., 109:253602, Dec 2012.

[20] Justin G. Bohnet, Zilong Chen, Joshua M. Weiner, Kevin C. Cox, and James K. Thompson. Active and passive sensing of collective atomic coherence in a superradiant laser. Phys. Rev. A, 88:013826, Jul 2013.

[21] Justin G. Bohnet, Zilong Chen, Joshua M. Weiner, Kevin C. Cox, and James K. Thompson. Linear-response theory for superradiant lasers. Phys. Rev. A, 89:013806, Jan 2014.

[22] Justin G. Bohnet, Zilong Chen, Joshua M. Weiner, Kevin C. Cox, and James K. Thompson. Linear-response theory for superradiant lasers. Phys. Rev. A, 89:013806, Jan 2014.

[23] Justin G. Bohnet, Zilong Chen, Joshua M. Weiner, Dominic Meiser, Murray J. Holland, and James K. Thompson. A steady-state superradiant laser with less than one intracavity photon. Nature, 484(7392):78–81, April 2012.

[24] Justin G. Bohnet, Zilong Chen, Joshua M. Weiner, Dominic Meiser, Murray J. Holland, and James K. Thompson. A steady-state superradiant laser with less than one intracavity photon. Nature, 484(7392):78–81, Apr 2012.

[25] Carlos Alexandre Brasil, Felipe Fernandes Fanchini, and Reginaldo de Jesus Napolitano. A simple derivation of the lindblad equation. Revista Brasileira de Ensino de Física, 35(1):01–09, 2013.

[26] Robert Bücker, Julian Grond, Stephanie Manz, Tarik Berrada, Thomas Betz, Christian Koller, Ulrich Hohenester, Thorsten Schumm, Aurélien Perrin, and Jörg Schmiedmayer. Twin-atom beams. Nat. Phys., 7(8):608–611, 2011.

[27] D. Budker, W. Gawlik, D. F. Kimball, S. M. Rochester, V. V. Yashchuk, and A. Weis. Resonant nonlinear magneto-optical effects in atoms. Rev. Mod. Phys., 74:1153–1201, Nov 2002.

[28] Dmitry Budker and Michael Romalis. Optical magnetometry. Nat. Phys., 3(4):227–234, April 2007.

[29] A. M. Chang, H. D. Hallen, L. Harriott, H. F. Hess, H. L. Kao, J. Kwo, R. E. Miller, R. Wolfe, J. van der Ziel, and T. Y. Chang. Scanning hall probe microscopy. Applied Physics Letters, 61(16):1974–1976, 1992.

[30] JingBiao Chen. Active optical clock. Chinese Science Bulletin, 54:348–352, 2009.

[31] Zilong Chen. Breaking Quantum Limits with Collective Cavity-QED : Generation of Spin Squeezed States via Quantum Non-Demolition Measurements. PhD thesis, University of Colorado Boulder, 2013.

[32] Zilong Chen, Justin G. Bohnet, Shannon R. Sankar, Jiayan Dai, and James K. Thompson. Conditional spin squeezing of a large ensemble via the vacuum Rabi splitting. Phys. Rev. Lett., 106:133601, Mar 2011.

[33] Zilong Chen, Justin G. Bohnet, Joshua M. Weiner, Kevin C. Cox, and James K. Thompson. Cavity-aided nondemolition measurements for atom counting and spin squeezing. Phys. Rev. A, 89:043837, Apr 2014.

[34] Zilong Chen, Justin G. Bohnet, Joshua M. Weiner, and James K. Thompson. General formalism for evaluating the impact of phase noise on bloch vector rotations. Phys. Rev. A, 86:032313, Sep 2012.

[35] Zilong Chen, Justin G. Bohnet, Joshua M. Weiner, and James K. Thompson. A low phase noise microwave source for atomic spin squeezing experiments in 87rb. Review of Scientific Instruments, 83(4):–, 2012.

[36] C. W. Chou, D. B. Hume, T. Rosenband, and D. J. Wineland. Optical clocks and relativity. Science, 329(5999):1630–1633, 2010.

[37] J. Clarke. SQUID Sensors: Fundamentals, Fabrication and Applications. Kluwer Academic Publishers, 1996.

[38] C. Cohen-Tannoudji, J. DuPont-Roc, S. Haroche, and F. Laloë. Detection of the static magnetic field produced by the oriented nuclei of optically pumped ^{3}He gas. Phys. Rev. Lett., 22:758–760, Apr 1969.

[39] Garrett D Cole, Wei Zhang, Michael J Martin, Jun Ye, and Markus Aspelmeyer. Tenfold reduction of brownian noise in high-reflectivity optical coatings. Nature Photonics, 7(8):644–650, 2013.

[40] Alan Corney. Atomic and Laser Spectroscopy. Clarendon Press, 1977.

[41] Kevin C. Cox, Matthew A. Norcia, Joshua M. Weiner, Justin G. Bohnet, and James K. Thompson. Reducing collective quantum state rotation errors with reversible dephasing. Applied Physics Letters, 105(26):–, 2014.

[42] Kevin C Cox, Joshua M Weiner, Graham P Greve, and James K Thompson. Generating entanglement between atomic spins with low-noise probing of an optical cavity. arXiv, 2015.

[43] Kevin C. Cox, Joshua M. Weiner, and James K. Thompson. Phase diagram for injection locking a superradiant laser. Phys. Rev. A, 90:053845, Nov 2014.

[44] M. C. Cross. Improving the frequency precision of oscillators by synchronization. Phys. Rev. E, 85:046214, Apr 2012.

[45] Jean Dalibard and Claude Cohen-Tannoudji. Laser cooling below the doppler limit by polarization gradients: simple theoretical models. JOSA B, 6(11):2023–2045, 1989.

[46] Emanuele G. Dalla Torre, Johannes Otterbach, Eugene Demler, Vladan Vuletic, and Mikhail D. Lukin. Dissipative preparation of spin squeezed atomic ensembles in a steady state. Phys. Rev. Lett., 110:120402, Mar 2013.

[47] Pascal Del'Haye, Katja Beha, Scott B Papp, and Scott A Diddams. Self-injection locking and phase-locked states in microresonator-based optical frequency combs. Phys. Rev. Lett., 112(4):043905, January 2014.

[48] Sebastian Diehl, Andrea Tomadin, Andrea Micheli, Rosario Fazio, and Peter Zoller. Dynamical phase transitions and instabilities in open atomic many-body systems. Phys. Rev. Lett., 105:015702, Jul 2010.

[49] F. Dimer, B. Estienne, A. S. Parkins, and H. J. Carmichael. Proposed realization of the dicke-model quantum phase transition in an optical cavity qed system. Phys. Rev. A, 75:013804, Jan 2007.

[50] Keiji Enpuku, Tadashi Minotani, Takemitsu Gima, Yukinori Kuroki, Yuzuru Itoh, Makiko Yamashita, Yoshinori Katakura, and Satoru Kuhara. Detection of magnetic nanoparticles with superconducting quantum interference device (squid) magnetometer and application to immunoassays. Japanese Journal of Applied Physics, 38(10A):L1102, 1999.

[51] Richard P Feynman, Frank L Vernon Jr, and Robert W Hellwarth. Geometrical representation of the schrödinger equation for solving maser problems. Journal of applied physics, 28(1):49–52, 1957.

[52] Michael Foss-Feig, Kaden RA Hazzard, John J Bollinger, and Ana Maria Rey. Nonequilibrium dynamics of arbitrary-range ising models with decoherence: An exact analytic solution. Physical Review A, 87(4):042101, 2013.

[53] Sarang Gopalakrishnan, Benjamin L. Lev, and Paul M. Goldbart. Exploring models of associative memory via cavity quantum electrodynamics. Philosophical Magazine, 92(January 2015):353–361, 2012.

[54] Ya. S. Greenberg. Application of superconducting quantum interference devices to nuclear magnetic resonance. Rev. Mod. Phys., 70:175–222, Jan 1998.

[55] Paul Hamilton, Matt Jaffe, Justin M. Brown, Lothar Maisenbacher, Brian Estey, and Holger Müller. Atom interferometry in an optical cavity. Phys. Rev. Lett., 114:100405, Mar 2015.

[56] Chris D. Hamley, C. S. Gerving, T. M. Hoang, E. M. Bookjans, and Michael S. Chapman. Spin-nematic squeezed vacuum in a quantum gas. Nat. Phys., 8(4):305–308, February 2012.

[57] Serge Haroche and Jean Michel Raimond. Exploring the quantum. Oxford Univ. Press, 2006.

[58] P. G. Harris, C. A. Baker, K. Green, P. Iaydjiev, S. Ivanov, D. J. R. May, J. M. Pendlebury, D. Shiers, K. F. Smith, M. van der Grinten, and P. Geltenbort. New experimental limit on the electric dipole moment of the neutron. Phys. Rev. Lett., 82:904–907, Feb 1999.

[59] TP Heavner, SR Jefferts, EA Donley, JH Shirley, and TE Parker. Nist-f1: recent improvements and accuracy evaluations. Metrologia, 42(5):411, 2005.

[60] J. M. Higbie, E. Corsini, and D. Budker. Robust, high-speed, all-optical atomic magnetometer. Rev. Sci. Inst., 77(11):113106, November 2006.

[61] N Hinkley, JA Sherman, NB Phillips, M Schioppo, ND Lemke, K Beloy, M Pizzocaro, CW Oates, and AD Ludlow. An atomic clock with 10–18 instability. Science, 341(6151):1215–1218, 2013.

[62] Travis Horrom, Robinjeet Singh, Jonathan P. Dowling, and Eugeniy E. Mikhailov. Quantum-enhanced magnetometer with low-frequency squeezing. Phys. Rev. A, 86:023803, Aug 2012.

[63] K. Jensen, N. Leefer, A. Jarmola, Y. Dumeige, V. M. Acosta, P. Kehayias, B. Patton, and D. Budker. Cavity-enhanced room-temperature magnetometry using absorption by nitrogen-vacancy centers in diamond. Phys. Rev. Lett., 112:160802, Apr 2014.

[64] Shehzaad Kaka, Matthew R. Pufall, William H. Rippard, Thomas J. Silva, Stephen E. Russek, and Jordan A. Katine. Mutual phase-locking of microwave spin torque nano-oscillators. Nature, 437(7057):389–392, September 2005.

[65] Georgy A Kazakov and Thorsten Schumm. Active optical frequency standards using cold atoms: perspectives and challenges. arXiv preprint arXiv:1503.03998, 2015.

[66] Alexei Yu Kitaev, Alexander Shen, and Mikhail N Vyalyi. Classical and quantum computation. Number 47. American Mathematical Soc., 2002.

[67] Masahiro Kitagawa and Masahito Ueda. Squeezed spin states. Phys. Rev. A, 47:5138–5143, Jun 1993.

[68] Daniel Kleppner, H. Mark Goldenberg, and Norman F. Ramsey. Theory of the hydrogen maser. Phys. Rev., 126:603–615, Apr 1962.

[69] I. K. Kominis, T. W. Kornack, J. C. Allred, and M. V. Romalis. A subfemtotesla multichannel atomic magnetometer. Nature, 422(6932):596–599, April 2003.

[70] Shlomi Kotler, Nitzan Akerman, Yinnon Glickman, Anna Keselman, and Roee Ozeri. Single-ion quantum lock-in amplifier. Nature, 473(7345):61–65, May 2011.

[71] SJM Kuppens, MP Van Exter, and JP Woerdman. Quantum-limited linewidth of a bad-cavity laser. Physical review letters, 72(24):3815, 1994.

[72] SJM Kuppens, MP Van Exter, JP Woerdman, and MI Kolobov. Observation of the effect of spectrally inhomogeneous gain on the quantum-limited laser linewidth. Optics communications, 126(1):79–84, 1996.

[73] Tony E. Lee, Ching-Kit Chan, and Shenshen Wang. Entanglement tongue and quantum synchronization of disordered oscillators. Phys. Rev. E, 89:022913, Feb 2014.

[74] Tony E. Lee and M. C. Cross. Quantum-classical transition of correlations of two coupled cavities. Phys. Rev. A, 88:013834, Jul 2013.

[75] Tony E. Lee and H. R. Sadeghpour. Quantum synchronization of quantum van der pol oscillators with trapped ions. Phys. Rev. Lett., 111:234101, Dec 2013.

[76] D. Leibfried, M. D. Barrett, T. Schaetz, J. Britton, J. Chiaverini, W. M. Itano, J. D. Jost, C. Langer, and D. J. Wineland. Toward Heisenberg-limited spectroscopy with multiparticle entangled states. Science, 304(5676):1476–1478, 2004.

[77] Dietrich Leibfried, Emanuel Knill, Signe Seidelin, Joe Britton, R Brad Blakestad, John Chiaverini, Davi d B Hume, Wayne M Itano, John D Jost, Christopher Langer, et al. Creation of a six-atom schrödinger cat-state. Nature, 438(7068):639–642, 2005.

[78] Ian D. Leroux, Monika H. Schleier-Smith, and Vladan Vuletić. Implementation of cavity squeezing of a collective atomic spin. Phys. Rev. Lett., 104:073602, Feb 2010.

[79] Ian D. Leroux, Monika H. Schleier-Smith, and Vladan Vuletić. Orientation-dependent entanglement lifetime in a squeezed atomic clock. Phys. Rev. Lett., 104:250801, Jun 2010.

[80] Paul D. Lett, Richard N. Watts, Christoph I. Westbrook, William D. Phillips, Phillip L. Gould, and Harold J. Metcalf. Observation of atoms laser cooled below the doppler limit. Phys. Rev. Lett., 61:169–172, Jul 1988.

[81] Wlodzimierz Lewandowski, Jacques Azoubib, and William J Klepczynski. Gps: primary tool for time transfer. Proceedings of the IEEE, 87(1):163–172, 1999.

[82] S. Li, P. Vachaspati, D. Sheng, N. Dural, and M. V. Romalis. Optical rotation in excess of 100 rad generated by rb vapor in a multipass cell. Phys. Rev. A, 84:061403, Dec 2011.

[83] Rodney Loudon. The quantum theory of light. Oxford university press, 2000.

[84] Bernd Lücke, Jan Peise, Giuseppe Vitagliano, Jan Arlt, Luis Santos, Géza Tóth, and Carsten Klempt. Detecting multiparticle entanglement of dicke states. Phys. Rev. Lett., 112:155304, Apr 2014.

[85] Max Ludwig and Florian Marquardt. Quantum many-body dynamics in optomechanical arrays. Phys. Rev. Lett., 111:073603, Aug 2013.

[86] A. Mari, A. Farace, N. Didier, V. Giovannetti, and R. Fazio. Measures of quantum synchronization in continuous variable systems. Phys. Rev. Lett., 111:103605, Sep 2013.

[87] M. J. Martin, D. Meiser, J. W. Thomsen, Jun Ye, and M. J. Holland. Extreme nonlinear response of ultranarrow optical transitions in cavity qed for laser stabilization. Phys. Rev. A, 84:063813, Dec 2011.

[88] Matthew H. Matheny, Matt Grau, Luis G. Villanueva, Rassul B. Karabalin, M. C. Cross, and Michael L. Roukes. Phase synchronization of two anharmonic nanomechanical oscillators. Phys. Rev. Lett., 112:014101, Jan 2014.

[89] D J McCarron, S A King, and S L Cornish. Modulation transfer spectroscopy in atomic rubidium. Measurement Science and Technology, 19(10):105601, 2008.

[90] Jason McKeever, Andreea Boca, A David Boozer, Joseph R Buck, and H Jeff Kimble. Experimental realization of a one-atom laser in the regime of strong coupling. Nature, 425(6955):268–271, 2003.

[91] Moritz Mehmet, Stefan Ast, Tobias Eberle, Sebastian Steinlechner, Henning Vahlbruch, and Roman Schnabel. Squeezed light at 1550 nm with a quantum noise reduction of 12.3 db. Optics express, 19(25):25763–25772, 2011.

[92] S. Meiboom and D. Gill. Modified spinecho method for measuring nuclear relaxation times. Review of Scientific Instruments, 29(8), 1958.

[93] D. Meiser and M. J. Holland. Steady-state superradiance with alkaline-earth-metal atoms. Phys. Rev. A, 81:033847, Mar 2010.

[94] D. Meiser, Jun Ye, D. R. Carlson, and M. J. Holland. Prospects for a millihertz-linewidth laser. Phys. Rev. Lett., 102:163601, Apr 2009.

[95] V. Meyer, M. A. Rowe, D. Kielpinski, C. A. Sackett, W. M. Itano, C. Monroe, and D. J. Wineland. Experimental demonstration of entanglement-enhanced rotation angle estimation using trapped ions. Phys. Rev. Lett., 86:5870–5873, Jun 2001.

[96] Thomas Monz, Philipp Schindler, Julio T. Barreiro, Michael Chwalla, Daniel Nigg, William A. Coish, Maximilian Harlander, Wolfgang Hänsel, Markus Hennrich, and Rainer Blatt. 14-qubit entanglement: Creation and coherence. Phys. Rev. Lett., 106:130506, Mar 2011.

[97] W. Muessel, H. Strobel, D. Linnemann, B. Hume, D. and K. Oberthaler, M.˙ Scalable spin squeezing for quantum-enhanced magnetometry with bose-einstein condensates. Phys. Rev. Lett., 113:103004, Sep 2014.

[98] H. C. Nägerl, D. Leibfried, H. Rohde, G. Thalhammer, J. Eschner, F. Schmidt-Kaler, and R. Blatt. Laser addressing of individual ions in a linear ion trap. Phys. Rev. A, 60:145–148, Jul 1999.

[99] TL Nicholson, SL Campbell, RB Hutson, GE Marti, BJ Bloom, RL McNally, W Zhang, MD Barrett, MS Safronova, GF Strouse, et al. Systematic evaluation of an atomic clock at 2 [times] 10-18 total uncertainty. Nature communications, 6, 2015.

[100] Caspar F. Ockeloen, Roman Schmied, Max F. Riedel, and Philipp Treutlein. Quantum metrology with a scanning probe atom interferometer. Phys. Rev. Lett., 111:143001, Oct 2013.

[101] Myriam Pannetier, Claude Fermon, Gerald Le Goff, Juha Simola, and Emma Kerr. Femtotesla magnetic field measurement with magnetoresistive sensors. Science, 304(5677):1648–1650, 2004.

[102] Randolf Pohl, Ronald Gilman, Gerald A Miller, and Krzysztof Pachucki. Muonic hydrogen and the proton radius puzzle. arXiv preprint arXiv:1301.0905, 2013.

[103] Simon Rainville, James K Thompson, and David E Pritchard. An ion balance for ultra-high-precision atomic mass measurements. Science, 303(5656):334–338, 2004.

[104] Norman F. Ramsey. A molecular beam resonance method with separated oscillating fields. Phys. Rev., 78:695–699, Jun 1950.

[105] Behzad Razavi. A study of injection locking and pulling in oscillators. IEEE Journal of Solid-State Circuits, 39(9):1415–1424, 2004.

[106] Fritz Riehle. Frequency standards: basics and applications. John Wiley & Sons, 2006.

[107] Till Rosenband, DB Hume, PO Schmidt, CW Chou, A Brusch, L Lorini, WH Oskay, RE Drullinger, TM Fortier, JE Stalnaker, et al. Frequency ratio of al+ and hg+ single-ion optical clocks; metrology at the 17th decimal place. Science, 319(5871):1808–1812, 2008.

[108] C.T. Russell, R.C. Snare, J.D. Means, D. Pierce, D. Dearborn, M. Larson, G. Barr, and G. Le. The ggs/polar magnetic fields investigation. Space Science Reviews, 71(1-4):563–582, 1995.

[109] S. Sani, J. Persson, S.M. Mohseni, Ye Pogoryelov, P.K. Muduli, A. Eklund, G. Malm, M. Käll, A. Dmitriev, and J. Åkerman. Mutually synchronized bottom-up multi-nanocontact spin-torque oscillators. Nat Commun, 4:–, November 2013.

[110] Monika H. Schleier-Smith, Ian D. Leroux, and Vladan Vuletić. States of an ensemble of two-level atoms with reduced quantum uncertainty. Phys. Rev. Lett., 104:073604, Feb 2010.

[111] Peter D. D. Schwindt, Svenja Knappe, Vishal Shah, Leo Hollberg, John Kitching, Li A. Liew, and John Moreland. Chip-scale atomic magnetometer. Applied Physics Letters, 85(26):6409–6411, 2004.

[112] R. J. Sewell, M. Koschorreck, M. Napolitano, B. Dubost, N. Behbood, and M. W. Mitchell. Magnetic sensitivity beyond the projection noise limit by spin squeezing. Phys. Rev. Lett., 109:253605, Dec 2012.

[113] D. Sheng, S. Li, N. Dural, and M. V. Romalis. Sub-femtotesla scalar atomic magnetometer using multipass cells, August 2012.

[114] D. Sheng, S. Li, N. Dural, and M. V. Romalis. Subfemtotesla scalar atomic magnetometry using multipass cells. Phys. Rev. Lett., 110:160802, Apr 2013.

[115] Seung-Bo Shim, Matthias Imboden, and Pritiraj Mohanty. Synchronized oscillation in coupled nanomechanical oscillators. Science (New York, N.Y.), 316(5821):95–9, April 2007.

[116] Jonathan Simon. Cavity QED with atomic ensembles. PhD thesis, Harvard University, 2010.

[117] R_E Slusher, LW Hollberg, Bernard Yurke, JC Mertz, and JF Valley. Observation of squeezed states generated by four-wave mixing in an optical cavity. Physical Review Letters, 55(22):2409, 1985.

[118] Anders Sørensen and Klaus Mølmer. Quantum computation with ions in thermal motion. Physical review letters, 82(9):1971, 1999.

[119] S. Steinert, F. Dolde, P. Neumann, A. Aird, B. Naydenov, G. Balasubramanian, F. Jelezko, and J. Wrachtrup. High sensitivity magnetic imaging using an array of spins in diamond. Review of Scientific Instruments, 81(4):–, 2010.

[120] Steven Strogatz. Sync: The emerging science of spontaneous order. Hyperion, 2003.

[121] Steven H. Strogatz. From Kuramoto to Crawford: exploring the onset of synchronization in populations of coupled oscillators. Physica D: Nonlinear Phenomena, 143:1–20, 2000.

[122] O. Sushkov, A. I. Lovchinsky, N. Chisholm, L. Walsworth, R. H. Park, and D. Lukin, M.˙ Magnetic resonance detection of individual proton spins using quantum reporters. Phys. Rev. Lett., 113:197601, Nov 2014.

[123] Haruka Tanji-Suzuki, Ian D. Leroux, Monika H. Schleier-Smith, Marko Cetina, Andrew T. Grier, Jonathan Simon, and Vladan Vuletić. Interaction between atomic ensembles and optical resonators: Classical description. Adv. At. Mol. Opt. Phys., 60:201, 2011.

[124] J. M. Taylor, P. Cappellaro, L. Childress, L. Jiang, D. Budker, P. R. Hemmer, A. Yacoby, R. Walsworth, and M. D. Lukin. High-sensitivity diamond magnetometer with nanoscale resolution. Nature Physics, 4(10):810–816, September 2008.

[125] Michael A Taylor, Jiri Janousek, Vincent Daria, Joachim Knittel, Boris Hage, Hans-A Bachor, and Warwick P Bowen. Subdiffraction-limited quantum imaging within a living cell. Physical Review X, 4(1):011017, 2014.

[126] Andrea Tomadin, Sebastian Diehl, and Peter Zoller. Nonequilibrium phase diagram of a driven and dissipative many-body system. Phys. Rev. A, 83:013611, Jan 2011.

[127] Q. A. Turchette, C. S. Wood, B. E. King, C. J. Myatt, D. Leibfried, W. M. Itano, C. Monroe, and D. J. Wineland. Deterministic entanglement of two trapped ions. Phys. Rev. Lett., 81:3631–3634, Oct 1998.

[128] Henning Vahlbruch, Simon Chelkowski, Boris Hage, Alexander Franzen, Karsten Danzmann, and Roman Schnabel. Demonstration of a squeezed-light-enhanced power-and signal-recycled michelson interferometer. Physical review letters, 95(21):211102, 2005.

[129] Frank Verstraete, Michael M. Wolf, and J. Ignacio Cirac. Quantum computation and quantum-state engineering driven by dissipation. Nat Phys, 5(9):633–636, 09 2009.

[130] Stefan Walter, Andreas Nunnenkamp, and Christoph Bruder. Quantum synchronization of a driven self-sustained oscillator. Phys. Rev. Lett., 112:094102, Mar 2014.

[131] W. Wasilewski, K. Jensen, H. Krauter, J. J. Renema, M. V. Balabas, and E. S. Polzik. Quantum Noise Limited and Entanglement-Assisted Magnetometry. Physical Review Letters, 104(13):133601+, mar 2010.

[132] J. Weber. Masers. Rev. Mod. Phys., 31:681–710, Jul 1959.

[133] Joshua M. Weiner, Kevin C. Cox, Justin G. Bohnet, Zilong Chen, and James K. Thompson. Superradiant raman laser magnetometer. Applied Physics Letters, 101(26):–, 2012.

[134] Y Henry Wen, Michael R E Lamont, Alexander L Gaeta, Isabel M Kloumann, and Steven H Strogatz. Self-organization in soliton modelocked parametric frequency combs. arXiv, 2014.

[135] D. J. Wineland, J. J. Bollinger, W. M. Itano, and D. J. Heinzen. Squeezed atomic states and projection noise in spectroscopy. Phys. Rev. A, 50:67–88, Jul 1994.

[136] D. J. Wineland, C. Monroe, W. M. Itano, D. Leibfried, B. E. King, and D. M. Meekhof. Experimental issues in coherent quantum-state manipulation of trapped atomic ions. J. Res. Natl Inst. Stand. Tech., 103:259, May 1998.

[137] Arthur T. Winfree. Biological rhythms and the behavior of populations of coupled oscillators. Journal of Theoretical Biology, 16(1):15 – 42, 1967.

[138] R Wynands and S Weyers. Atomic fountain clocks. Metrologia, 42(3):S64, 2005.

[139] Ze-Liang Xiang, Sahel Ashhab, J. Q. You, and Franco Nori. Hybrid quantum circuits: Superconducting circuits interacting with other quantum systems. Rev. Mod. Phys., 85:623–653, Apr 2013.

[140] Minghui Xu and M. J. Holland. Conditional ramsey spectroscopy with synchronized atoms. Phys. Rev. Lett., 114:103601, Mar 2015.

[141] Minghui Xu, David A. Tieri, E. C. Fine, James K. Thompson, and Murray J. Holland. Synchronization of two ensembles of atoms. Phys. Rev. Lett., 113:154101, Oct 2014.

[142] Lei Ying, Ying-Cheng Lai, and Celso Grebogi. Quantum manifestation of a synchronization transition in optomechanical systems. Phys. Rev. A, 90:053810, Nov 2014.

[143] J. Q. You, Xuedong Hu, S. Ashhab, and Franco Nori. Low-decoherence flux qubit. Phys. Rev. B, 75:140515, Apr 2007.

[144] Mian Zhang, Gustavo S. Wiederhecker, Sasikanth Manipatruni, Arthur Barnard, Paul McEuen, and Michal Lipson. Synchronization of Micromechanical Oscillators Using Light. Phys. Rev. Lett., 109(23):233906, December 2012.

[145] X. Zhang, M. Bishof, S. L. Bromley, C. V. Kraus, M. S. Safronova, P. Zoller, A. M. Rey, and J. Ye. Spectroscopic observation of su(n)-symmetric interactions in sr orbital magnetism. Science, 345(6203):1467–1473, 2014.

[146] Yifu Zhu, Daniel J. Gauthier, S. E. Morin, Qilin Wu, H. J. Carmichael, and T. W. Mossberg. Vacuum rabi splitting as a feature of linear-dispersion theory: Analysis and experimental observations. Phys. Rev. Lett., 64:2499–2502, May 1990.

Appendix A

Superradiant Laser Liouvillian

In Chapter 2, I introduced the master equation for superradiance in a 3-level system. The total Liouvillian $\mathcal{L}[\hat{\rho}]$ was mentioned but not written out fully. Here I show the Liouvillians comprising $\mathcal{L}[\hat{\rho}] = \mathcal{L}_c[\hat{\rho}] + \mathcal{L}_{eg}[\hat{\rho}] + \mathcal{L}_{3e}[\hat{\rho}] + \mathcal{L}_R[\hat{\rho}] + \mathcal{L}_{g3}[\hat{\rho}]$ for the dissipation processes.

$$\mathcal{L}_c[\hat{\rho}] = -\frac{\kappa}{2}(\hat{c}^\dagger\hat{c}\hat{\rho} + \hat{\rho}\hat{c}^\dagger\hat{c} - 2\hat{c}\hat{\rho}\hat{c}^\dagger \tag{A.1}$$

$$\mathcal{L}_{eg}[\hat{\rho}] = -\frac{\gamma}{2}\sum_{q=1}^{N}(\hat{\sigma}_{eg}^{(q)}\hat{\sigma}_{ge}^{(q)}\hat{\rho} + \hat{\rho}\hat{\sigma}_{eg}^{(q)}\hat{\sigma}_{ge}^{(q)} - 2\hat{\sigma}_{ge}^{(q)}\hat{\rho}\hat{\sigma}_{eg}^{(q)}) \tag{A.2}$$

$$\mathcal{L}_{3e}[\hat{\rho}] = -\frac{\Gamma_{3e}}{2}\sum_{q=1}^{N}(\hat{\sigma}_{3e}^{(q)}\hat{\sigma}_{e3}^{(q)}\hat{\rho} + \hat{\rho}\hat{\sigma}_{3e}^{(q)}\hat{\sigma}_{e3}^{(q)} - 2\hat{\sigma}_{e3}^{(q)}\hat{\rho}\hat{\sigma}_{3e}^{(q)}) \tag{A.3}$$

$$\mathcal{L}_R[\hat{\rho}] = \frac{\Gamma_R}{4}\sum_{q=1}^{N}((\hat{\sigma}_{ee}^{(q)} - \hat{\sigma}_{gg}^{(q)})\hat{\rho}(\hat{\sigma}_{ee}^{(q)} - \hat{\sigma}_{gg}^{(q)}) - (\hat{\sigma}_{ee}^{(q)} + \hat{\sigma}_{gg}^{(q)})\hat{\rho}) \tag{A.4}$$

$$\mathcal{L}_{g3}[\hat{\rho}] = -\frac{W}{2}\sum_{q=1}^{N}(\hat{\sigma}_{g3}^{(q)}\hat{\sigma}_{3g}^{(q)}\hat{\rho} + \hat{\rho}\hat{\sigma}_{g3}^{(q)}\hat{\sigma}_{3g}^{(q)} - 2\hat{\sigma}_{3g}^{(q)}\hat{\rho}\hat{\sigma}_{g3}^{(q)}). \tag{A.5}$$